Department of Physics and Astronomy

University of Heidelberg

Master thesis

in Physics

submitted by

Michael Rudolf Ciupek

born in Landstuhl

2019

Electrons from semi-leptonic decays of heavy-flavour hadrons at mid-rapidity and low transverse momenta in pp collisions at $\sqrt{s} = 5.02$ TeV

This Master thesis has been carried out by

Michael Rudolf Ciupek

at the

Physikalisches Institut

under the supervision of

Prof. Dr. Silvia Masciocchi

Abstract

Within this thesis, the p_T-differential production cross section of electrons from semi-leptonic decays of heavy-flavour hadrons in proton-proton collisions at $\sqrt{s} = 5.02$ TeV was measured with ALICE at the LHC. The measurement of electrons from semi-leptonic decays of heavy-flavour hadrons requires a good knowledge of the electron background. The main contribution from the background sources is removed by tagging electrons from Dalitz decays and photon conversions in the detector material. The production cross section of electrons from semi-leptonic decays of heavy-flavour hadrons is compared to perturbative quantum chromo dynamics and is used as a reference to compute the nuclear modification factor of electrons from semi-leptonic decays of heavy-flavour hadrons in Pb-Pb and Xe-Xe collisions.

Zusammenfassung

Diese Arbeit beschäftigt sich mit der Messung des p_T-differentiellen Produktionsquerschnitt von Elektronen aus semi-elektronischen Zerfällen von Heavy-Flavour Hadronen in Proton-Proton Kollisionen bei einer Schwerpunktsenergie von $\sqrt{s} = 5.02$ TeV mit ALICE am LHC. Die Messung von Elektronen aus semi-elektronischen Zerfällen von Heavy-Flavour Hadronen erfordert eine genau Bestimmung des Elektronenhintergrund. Der Hauptanteil des Elektronenhintergrunds wird durch die Identifizierung von Elektronen aus Dalitz Zerfällen und Photon Konversionen entfernt. Diese Messung wird mit perturbativen Quatnumchromodynamik verglichen und dient als Referenzmessung, um den nuklearen Modifikationsfaktor von Elektronen aus semi-elektronsichen Zerfällen von Heavy-Flavour Hadronen in Blei-Blei und Xenon-Xenon Kollisionen zu bestimmen.

Contents

1 Introduction

1.1 Quantum chromodynamics

Quantum Chromo Dynamics (QCD) is a gauge field theory describing the strong interaction between quarks and gluons. It is a non-abelian gauge theory with invariance under local SU(3) transformations. The Lagrangian of QCD is given by:

$$L_{QCD} = \sum_{i=0}^{n} \overline{\Psi}_i (i\gamma^\mu D_\mu - m_i)\Psi_i - \frac{1}{4}F_{\mu\nu}^a F_a^{\mu\nu} \tag{1}$$

where n is the number of quark flavours and $D_\mu = \partial_\mu - \frac{1}{2}igA_\mu^a \lambda_a$, the covariant derivative. The fields Ψ_i correspond to the quarks with flavour i. The gauge fields $A_\mu = A_\mu^a \lambda_a$, where λ_a corresponds to the eight generators of the SU(3) group, correspond to the bosons of the strong interaction, called gluons. Compared to Quantum Electro Dynamics (QED), QCD has three different charges called color (red, blue, green). Besides, the gluons carry itself color charge, different from the photon, which is a neutral particle. The field tensor F_μ^a can be written as:

$$F_{\mu\nu}^a = \partial_\mu A_\nu^a - \partial_\nu A_\mu^a + g_s f_{abc} A_\mu^b A_\nu^c \tag{2}$$

where f_{abc} and g_s are the structure function and gauge coupling constant. Since the generators of the SU(3) group do not commute, $[A^a, A^b] = f_{abc}A^c \neq 0$, the last term of (2) leads to gluon self interactions. Although there is evidence for the existence of quarks [1, 2], they were never detected as free particles [3]. The non-observation of free quarks is described by the observation of color confinement, which states that the coloured objects are always confined to color singlet states. At the moment, the concept of color confinement is not yet understood from a theoretical point of view.

At low energy scales the coupling constant of QCD ($\alpha_s = g_s^2/4\pi$) is rather large and perturbation theory cannot be applied and computational approaches like lattice QCD need to be used.
Following the treatment of renormalization for QCD, the functional dependence of α_s with the energy transfer $|q^2|$ is given by [4]:

$$\alpha_s(|q^2|) = \frac{12\pi}{(11f - 2n)ln(\frac{|q^2|}{\Lambda_{QCD}^2})} \tag{3}$$

where f is the number of colors and n the number of quark flavours. Since 11f-2n > 1, α_s decreases at larger energy scales [5, 6]. This behaviour is known as
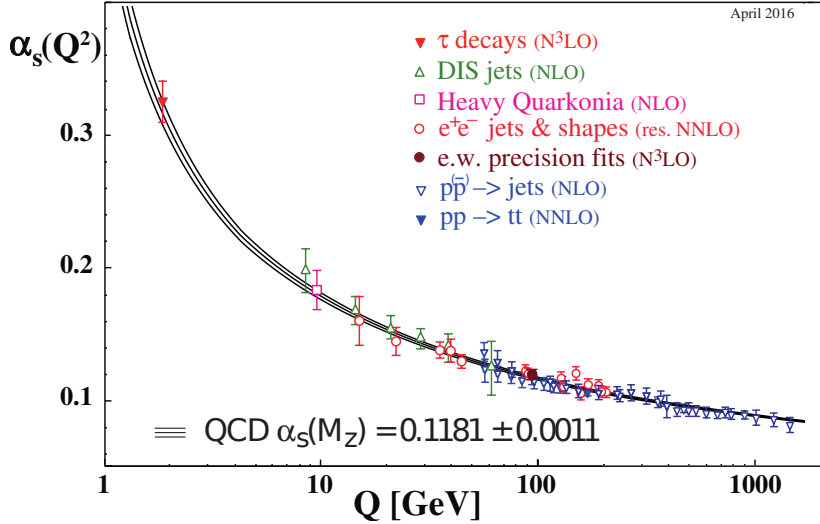
Figure 1.1: The strong coupling constant as function of the energy scale. Image taken from [7].

asymptotic freedom and is experimentally tested for different energy scales, as shown in Figure 1.1.

1.2 Quark Gluon Plasma

The observation of QCD as an asymptotically free gauge theory lead to the hypothesis that there exists a phase transition between confined hadronic matter and a plasma, where partons behave like free constitutes. This hypothesis can be understood by simple considerations. Hadrons have a finite size of approximately 1 fm. Therefore, with increasing density, these hadrons start to overlap, until the original quark is in the vicinity of a considerable number of other quarks [8]. At this point the original quark cannot identify the other quarks with which it formed the hadron and the concept of a hadron loses its meaning, reaching a state of matter, where partons act as free particles. These state of matter is known as the Quark Gluon Plasma [9].

The strongly interacting matter can be found in different phases, depending on the temperature T and the baryochemical potential μ_B, quantifying the net baryon density. A schematic sketch of these phases is shown in Figure 1.2.
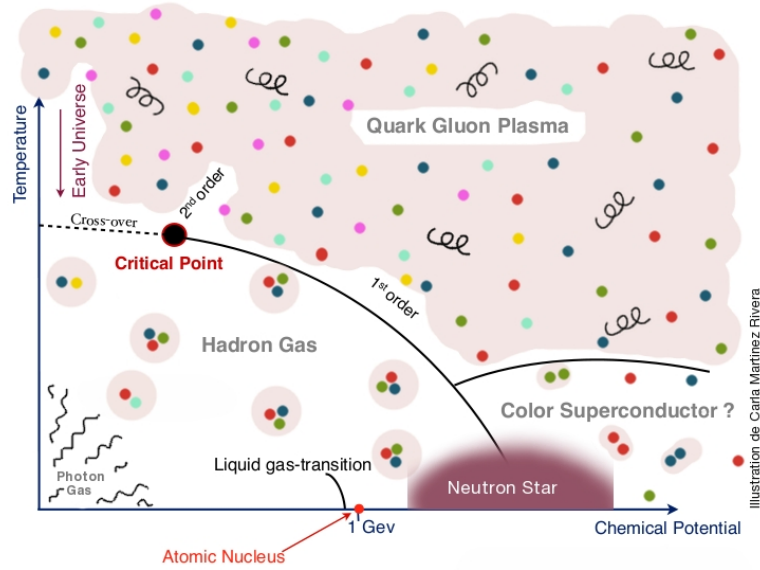
Figure 1.2: Phase diagram of strongly interacting matter. Image taken from [10].

At low temperatures T and small μ_B, quarks and gluons are confined in hadronic matter, bound to color neutral objects as in ordinary nuclear matter of our environment, around $\mu_B \approx 1$ GeV. At large μ_B and small temperatures, an additional state of matter is expected, the color superconductor, in which quark and gluons form color Cooper pairs. This state of matter probably exists in the cores of neutron stars, where μ_B is very large, due to extreme gravitational compression.

At sufficiently high baryochemical potential and temperature, the confined phase is been separated from the deconfined phase by a sharp first-order transition. On the other hand, at low μ_B, the phase transition from confined and deconfined matter is a rapid crossover process occurring in a small and well defined temperature interval [11]. According to lattice QCD, the phase transition at zero baryochemical potential, which is investigated via ultra-relativistic heavy-ion collisions (e.g. LHC), happens around $T(\mu_B = 0) = (156.5 \pm 1.5)$ MeV [12]. Lattice QCD at non-zero baryochemical potential also suggests the existence of a critical point, where the phase transition changes from a crossover to first-order type.

The phase transition from the QGP to ordinary hadronic matter occurred in the early universe after the Big Bang at vanishing baryochemical potential and high temperature during the expansion and cooling of the early universe. On the other hand, in neutron stars, the QGP is formed at large baryochemical potential and temperature close to zero. Therefore the investigation of the QCD phase diagram at different values of μ_B and T is crucial for our understanding of strong interac-

tions.

At these days, the region of high T and low μ_B is investigated via ultra-relativistic heavy-ion collisions at the LHC and RHIC. The Beam Energy Scan (BES) program of RHIC scans the QCD phase diagram for different values of T and high μ_B to allow for the exploration of the first-order phase transition and the critical point [13, 14]. In addition, in the future there will be another facility FAIR, probing the QGP at larger μ_B. On the other hand, the regime of temperatures close to zero and large baryochemical potential is indirectly investigated in the context of astrophysical studies.

2   Open heavy flavour

2.1   Heavy-quark production in p-p collisions

The production of heavy-quarks in pp collisions proceeds via initial hard partonic scattering, since the mass of these heavy quarks i.e. charm ($m_c \approx 1.27 \ GeV/c^2$) and beauty ($m_b \approx 4.18 \ GeV/c^2$) is much larger than the QCD scale parameter $\lambda_{QCD} \approx 0.2$ GeV. Because of their large mass, the production of heavy-flavour quarks can be described theoretically via perturbative QCD (pQCD) calculations over all momenta, whereas light quarks and gluons can only be described via pQCD at high transverse momenta [15]. Therefore, the measurement of heavy-quark production serves as an important test of pQCD calculations and improves our understanding of the underlying processes. The production process of a hadron carrying a heavy quark can be factorized into three different components [16]:

$$\frac{\mathrm{d}\sigma^{q'q'\to H_{q'}X}}{\mathrm{d}p_{\mathrm{T}}} = \sum_{i,j=q,\bar{q},g} f_i(x_1,\mu_{\mathrm{f}}^2)f_j(x_2,\mu_{\mathrm{f}}^2)\frac{\mathrm{d}\sigma^{ij\to q'\bar{q}'}}{\mathrm{d}p_{\mathrm{T}}}D_{q'\to H_{q'}}(z_{q'},\mu_{\mathrm{f}}^2) \quad (4)$$

where q´ is referring to the heavy quarks, p_{T} is the transverse momentum of the hadron, and the hadrons containing a heavy quark, in the context of this thesis mainly D or B mesons, are called $H_{q'}$. The factorization scale μ_{f} is often set equal to the momentum transfer in the given process. The different components of above equation are described in the following:

- initial conditions $f_i(x_1,\mu_{\mathrm{f}}^2)f_j(x_2,\mu_{\mathrm{f}}^2)$: The Parton Distribution Functions (PDF) describe the probability to find a quark or gluon of type i (j) carrying the momentum fraction of x_i (x_j) of the colliding nucleon. The PDFs have been studied in deep inelastic scattering experiments $e^- p \to e^- X$ at HERA [17] and also at the LHC [18].
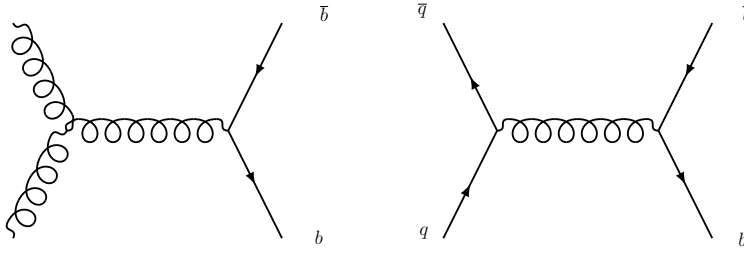
9

Figure 2.1: Examples for Feynman diagrams of heavy-quark production at Leading Order. The left diagram corresponds to gluon fusion, the right diagram to quark-antiquark annihilation.
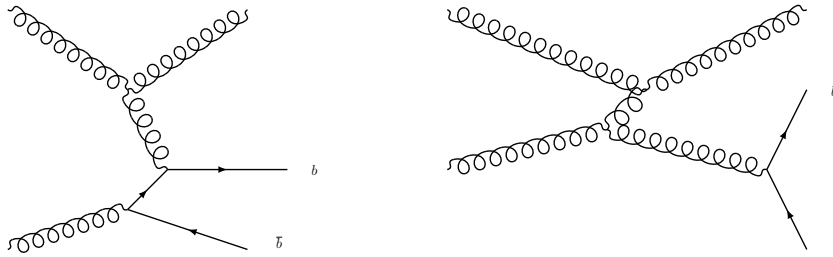
Figure 2.2: Examples for Feynman diagrams of heavy-quark production at Next-to-Leading Order. The left diagram corresponds to flavour excitation, the right one to gluon splitting.

- Partonic scattering cross-section $\frac{d\sigma^{ij \to q'\bar{q}'}}{dp_T}$: It can be calculated in perturbative QCD. The production of a heavy quark-antiquark pair is in Leading Order (LO) quark-antiquark annihilation and gluon fusion (Figure 2.1), where at LHC energies the latter one is the dominating source. At next-to-leading order (NLO) flavour excitation and gluon splitting (Figure 2.2) need to be considered as well.

- Fragmentation function $D_{q' \to H_{q'}}(z_{q'}, \mu_f^2)$: It represents the probability of the produced heavy-quark to create a hadron $H_{q'}$ with the momentum fraction z $= p_T/p_{q'}$. These functions are experimentally measured in e^+e^- collisions.

Heavy-flavour quarks hadronise and form relatively long-lived particles, for example, the D-meson (lifetime of $\approx$ 0.5-1 ps) or B-meson (lifetime of $\approx$ 1.5 ps). The measurement of heavy-flavour hadron decays can be performed in two different ways. The hadron can be kinematically fully reconstructed via its decay products,

for example, $D^0 \rightarrow K^- \pi^+$. Alternatively, electrons or muons from semi-leptonic decays are measured. The latter method does not allow for a full access of the decay kinematics but provides a higher branching ratio and bigger capabiltites at high-momentum in comparison to the full reconstruction of heavy hadrons. The measurement of the cross-section of electrons from semi-leptonic decays of heavy-flavour hadrons in pp collisions is described in Section 4 and is compared with the pQCD calculation of FONLL [19] in Section 5.

2.2   Heavy-quark production in nucleus-nucleus collision

In addition, to test pQCD calculations, the measurement of heavy-quark production in pp collisions treated in this thesis serves as an important reference to probe the properties of the QGP produced in heavy-ion collisions. Since heavy-quark production requires large momentum transfers, larger than the thermal momentum in the medium, they are dominantly produced in the early stages of the collision. The patrons propagate through the QGP, interact with the colored medium and lose energy. Therefore, the comparison of the cross-section of heavy-flavour hadrons in heavy-ion and pp collisions helps to understand the energy loss mechanism in the QGP and the properties of the QGP itself.

The simplest way to compare both measurements is in taking the ratio of both of the spectra. However, one can consider a heavy-ion collision as a superposition of many independent nucleon-nucleon interactions. The number of binary collisions N_{Coll} can be estimated via a comparision of a Glauber model [20] with the experimentally measured multiplicity in the experiment. The number of binary collisions can then be used to scale the differential yield of e.g electrons from semi-leptonic decays of heavy-flavour hadrons in pp collisions to the differential yield in heavy-ion collisions:

$$\frac{\mathrm{d}^2 N_{\mathrm{AA}}}{\mathrm{d}p_{\mathrm{T}}\mathrm{d}y} = N_{\mathrm{Coll}}\frac{\mathrm{d}^2 N_{\mathrm{pp}}}{\mathrm{d}p_{\mathrm{T}}\mathrm{d}y} \tag{5}$$

This so called binary scaling can be violated because of the nuclear medium, which is described in the next section.

2.3   Violation of binary scaling due to nuclear effects

The violation of binary scaling due to the presence of a strongly interacting medium, is usually divided in two classes:

- Initial state effects arise from the characteristics of the incoming colliding

nuclei.

- Final state effects are a result of the hadronic matter which is produced in heavy-ion collisions.

Initial and final states effects can be experimental studied with the nuclear modification factor R_{AA}:

$$R_{AA} = \frac{\mathrm{d}^2 N_{AA}/\mathrm{d}p_{\mathrm{T}}\mathrm{d}y}{< N_{\mathrm{coll}} > \mathrm{d}^2 N_{\mathrm{pp}}/\mathrm{d}p_{\mathrm{T}}\mathrm{d}y} \tag{6}$$

It is defined as the ratio of particle yield in nucleus-nucleus collisions to the binary scaled p-p yield, where no QGP is formed. In absence of nuclear effects, R_{AA} is equal to unity. One can also define a similar observable for proton-nucleus collisions, to investigate the initial state effects, since in such collisions the QGP is not produced and therefore the nuclear modification factor is not affected by final state effects.

2.3.1 Initial state effects

- **Cronin effect:** The Cronin effect can be described due to the increase of the initial transverse momentum of the parton before the hard collision. This effect is believed to come from multiple scattering of the initial partons on the incoming opposite nucleus, resulting in a larger transverse momentum for the initial parton. The resulting enhancement of the nuclear modification factor is sketched in Fig. 2.3.

- **Modification of PDF in a nucleus:** The parton distribution functions show a different behaviour when inside a nucleus compared to a free nucleon. This effect can be evaluated by defining the following ratio:

$$R_i^A = \frac{f_i^A(x, Q^2)}{f_i^N(x, Q^2)} \tag{7}$$

where f_i^A is the PDF of parton species i of the nucleon inside the nucleus and f_i^N is the PDF of the free nucleon. The effect on R_i^A as function of the Björken x is illustrated in Fig. 2.4.

To investigate these phenomena and disentangle them from effects coming directly from the QGP, a reference measurement with proton-nucleus collisions is needed, where no QGP is believed to be formed.
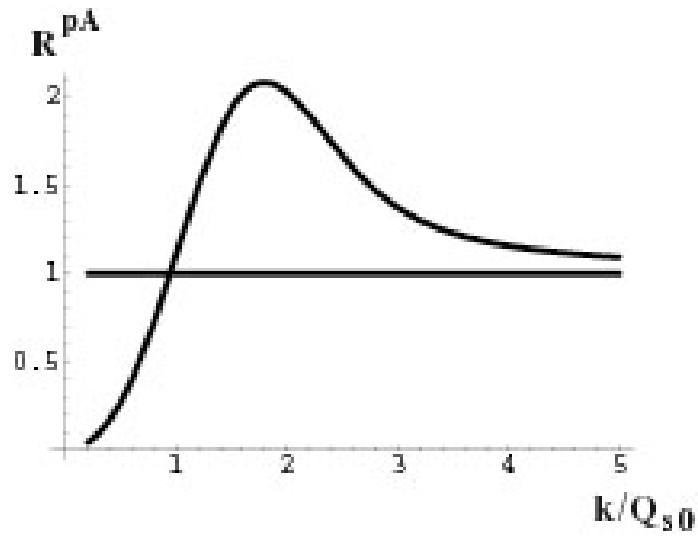
Figure 2.3: Nuclear modification factor in proton-nucleus collision, showing the Cronin effect. Image taken from [21].
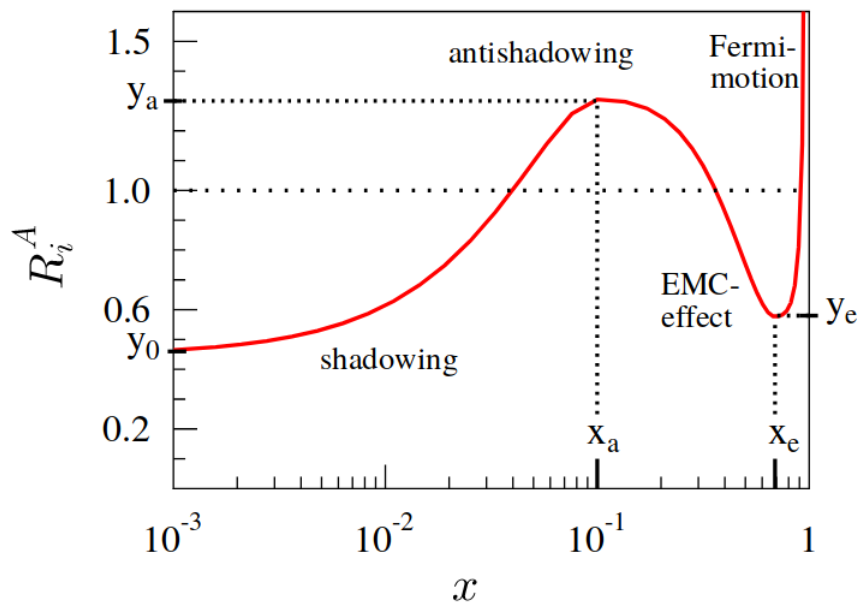

Figure 2.4: Example of nuclear effects on the PDF as function of the Björken x. Image taken from [22].

2.3.2 Final state effects

The initially produced partons traverse the QGP, interact with the medium and lose energy, mainly because of multiple scattering processes and medium-induced gluon radiation. The importance of both mechanisms is shortly described in the following:

- **Radiative energy loss:** The energy loss due to gluon radiation is very important for partons produced at high p_T and is different for gluons and quarks. The reason for that is the fact that the QCD coupling factor, so called Casimir factor, is different for gluon-quark ($C_F = \frac{3}{4}$) or gluon-gluon coupling ($C_A = 3$) and therefore the energy loss for particles coming from gluon fragmentation is larger than for those coming from quarks. Since a large fraction of light-flavoured hadrons is produced in the late stages of the collisions from the fragmentation of gluons, whereas heavy-flavour hadrons produced from the fragmentation of heavy quarks directly produced from the early stage of the collision, the suppression of light mesons is expected to be larger compared to mesons containing a charm or beauty quark.

    Beside of the Casimir factor, the mass of the quark itself determines the energy loss in the QGP, due to the so called dead-cone effect [23]. The dead-cone effect predicts a suppression of the gluon radiation at angles smaller than $\Theta_0 = \frac{m}{E}$. Since Θ_0 is larger for heavy quarks compared to light quarks, the cone where gluon radiation is forbidden is larger for heavy quarks and therefore the energy loss is smaller.
    As a consequence for the above described phenomena the following energy-loss hierarchy is expected:

$$\Delta E_{\text{beauty}} < \Delta E_{\text{charm}} < \Delta E_{\text{light quark}} < \Delta E_{\text{gluon}} \tag{8}$$

- **Collisional energy loss:** Partons can also lose energy via elastic collisions with the constitutes of the hot and dense medium. It was pointed out that the collisional energy loss should be comparable in magnitude to radiate energy loss over a whole kinematic interval [15].

    Figure 2.5 shows the comparison between the collisional (solid line) and radiative (dashed line) fractional energy loss as a function of the momentum p for light, charm and beauty quarks. The energy loss at lower momentum (p < 10 GeV/c (15 GeV/c) for light and charm (beauty)) is dominated by collisional energy loss mechanism rather than radiative ones.
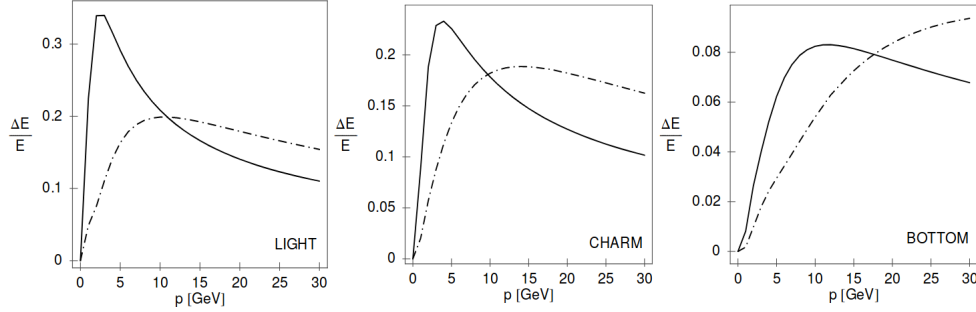
Figure 2.5: Comparison between the collisional (solid line) and radiative (dashed line) fractional energy loss as function of the momentum of light, charm and beauty quarks. Image taken from [24]

3   The ALICE detector

ALICE (A Large Ion Collider Experiment) is one of the four main experiments at the Large Hadron Collider (LHC) at CERN. It is designed to address the physics of strongly interacting matter and to study the QGP created in high-energy heavy-ion collisions.

The detector is designed to be sensitive to a momentum interval from approximately 100 MeV/c to 100 GeV/c in order to study hadrons, electrons, muons and photons created in the collision of heavy ions and protons [26].
ALICE has a size of 16 x 16 x 26 m^3 and weights about 10.000 t. The detector systems can be divided in three parts: The central barrel, the muon spectrometer and the forward detectors.
The central barrel detectors cover the midrapidity range ($|\eta| < 0.9$) and are embedded in the large solenoid magnet, from the L3 experiment of LEP, providing a magnetic field of B = 0.5 T longitudinal to the beam direction. These detectors are, from the innermost to the outermost, the Inner Tracking System (ITS), the Time Projection Chamber (TPC), Transition Radiation Detector (TRD), Time of Flight detector (TOF), Photon Spectrometer (PHOS), Electromagnetic Calorimeter (EMCal), Di-jet Calorimeter (DCal) and the High Momentum Particle Identification Detector (HMPID) [27].
The muon spectrometer covers the pseudo-rapidity region between -4 < η < -2.5

15

THE ALICE DETECTOR

a. ITS SPD (Pixel)
b. ITS SDD (Drift)
c. ITS SSD (Strip)
d. V0 and T0
e. FMD

1. ITS
2. FMD, T0, V0
3. TPC
4. TRD
5. TOF
6. HMPID
7. EMCal
8. DCal
9. PHOS, CPV
10. L3 Magnet
11. Absorber
12. Muon Tracker
13. Muon Wall
14. Muon Trigger
15. Dipole Magnet
16. PMD
17. AD
18. ZDC
19. ACORDE
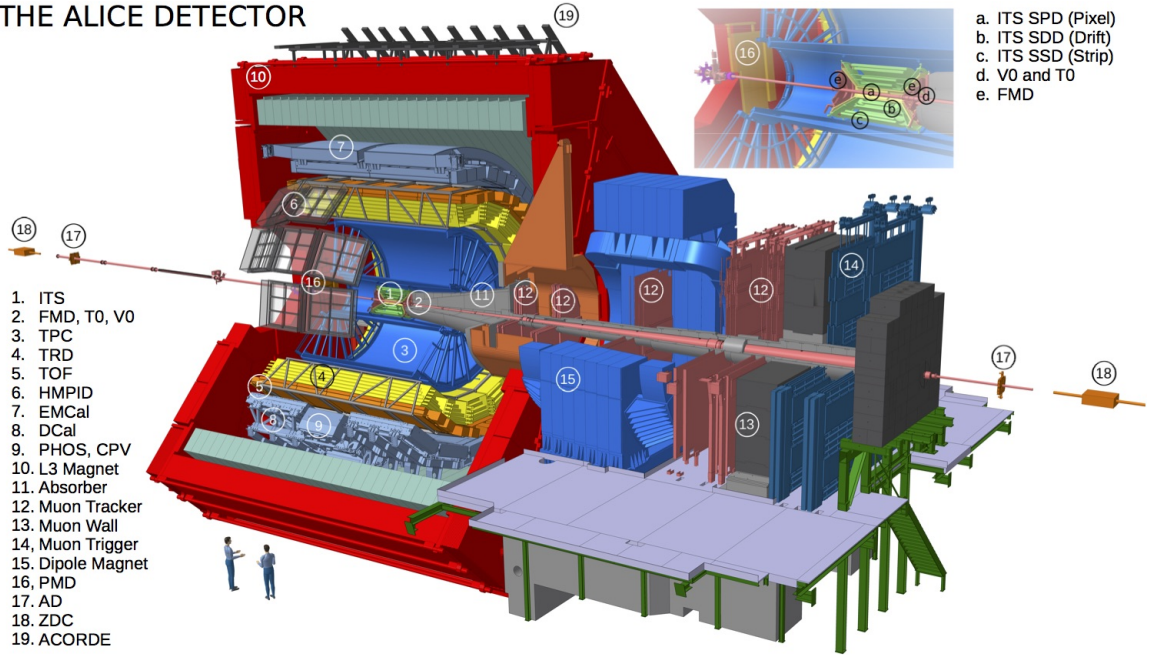
Figure 3.1: The ALICE experiment during Run 2. Image taken from [25].

and is used to measure quarkonia, light vector mesons and muons from heavy-flavour hadron decays.

The forward detectors are the Photon Multiplicity Detector (PMD) and the Forward Multiplicity Detector (FMD), used to measure photons and charged particles at $|\eta| \approx 3$, the plastic scintillation detector V0, used for triggering and the determination of centrality and event plane in Pb-Pb collisions, the Cherenkov detector T0, used to deliver times (eg. for Time of Flight detector) and the longitudinal position of the interaction, and the Zero Degree Calorimeter (ZDC), used to measure the centrality [27].

The ALICE experiment uses a right-handed orthogonal Cartesian coordinate system, which is centered in the middle of the central barrel. The z-axis is parallel to the beam direction and is pointing in the opposite direction of the muon spectrometer location. The x-axis points towards the centre of the LHC, whereas the y-axis is pointing upwards[28].

More information regarding ALICE can be found in [26]. The detectors used in this analysis are described in more details in the next sections.
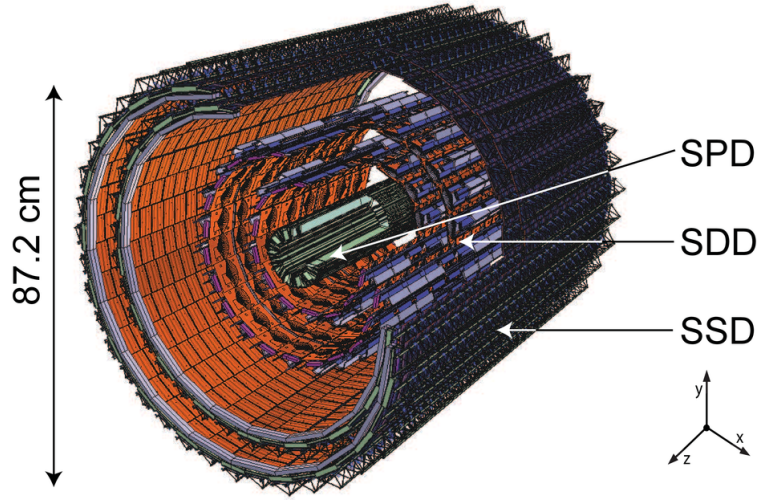
Figure 3.2: Layout of the ITS detector. Image take from [30]

3.1   Inner Tracking System

The Inner Tracking System (ITS) [29] is the innermost detector in the central barrel of ALICE and consists of six layers of three different types of silicon detectors and covers the pseudorapidity range of $|\eta| < 0.9$ ($|\eta| < 2$ for the first layer, $|\eta| < 1.4$ for the second layer). The layout of the ITS is shown in Figure 3.2.

Because of the high particle density expected at ALICE and the requirement to achieve a high resolution on the primary vertex position and impact parameter, the first two layers are built up of Silicon Pixel Detectors (SPD) and the intermediate two layers of Silicon Drift Detectors (SDD)[31]. The SPD allows to determine the position of the primary vertex with a resolution better than 100 μm and to reconstruct the secondary vertex from decays of hyperons, B and D mesons [26]. The two outermost layers are built of double sided Silicon Strip Detectors (SSD), which are crucial for the matching of tracks between the ITS and TPC. The SDD and SSD layers provide, in addition, particle identification information via the measurement of the specific energy loss dE/dx especially in the low momentum region. Some characteristics of the ITS layers is shown in Table 1.a

3.2   Time Projection Chamber

The Time Projection Chamber (TPC) [32] is the main detector of ALICE. It is a tracking detector with a total length of 5 m and a volume of ≈ 90 m^3. The TPC, shown in Fig. 3.3, is divided into two parts by a high-voltage electrode in

Table 1: Characteristics of the six ITS layers

Layer	Type	r[cm]	± z[cm]	$|\eta|$	Resolution rϕ × z[μm^2]
1	SPD	3.9	14.1	≤ 2.0	12 × 100
2	SPD	7.6	14.1	≤ 1.4	12 × 100
3	SDD	15	22.2	≤ 0.9	35 × 25
4	SDD	23.9	29.7	≤ 0.9	35 × 25
5	SSD	38.0	43.1	≤ 0.9	20 × 830
6	SSD	43.0	48.9	≤ 0.9	20 × 830
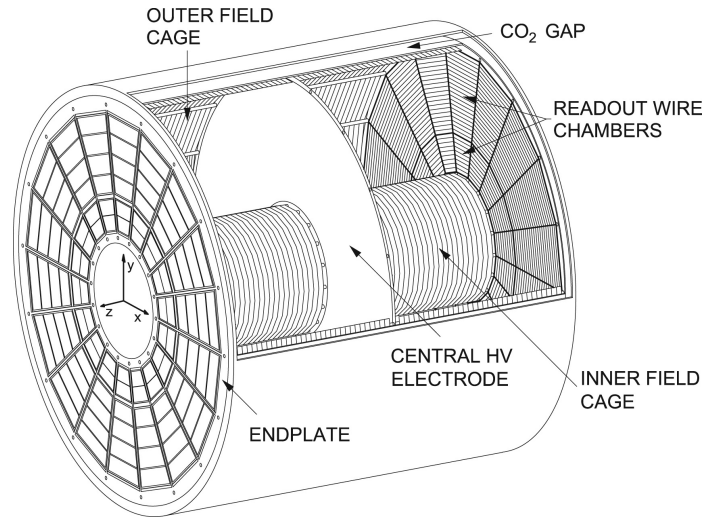
Figure 3.3: Schematic view of the ALICE TPC. Image is taken from [32].
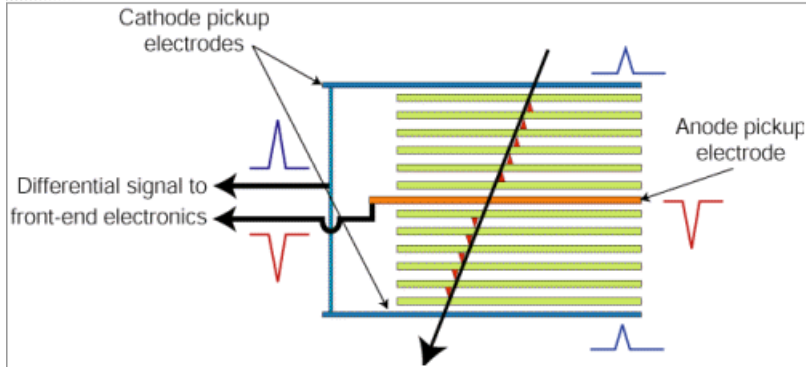
Figure 3.4: A schemetical sketch of the working principel of MRPC used in the TOF detector [34]

the center of the cylinder, providing a uniform electric field of 400 V/cm in both drift regions. Charged particles traverse the detector and ionize the gas. Electrons, generated by this ionization, drift longitudinally with respect to the electric field towards the end plates of the cylinder, where multi-wire proportional chambers (MWPC) are mounted. The readout is done via cathode pads arranged in 159 rows in the radial direction. The radial coordinate rΦ of the track is given by the signal release on the cathode pads. The third spatial component is given by the drift time of electrons needed to reach the end cap. Therefore, a three dimensional reconstruction of the track is obtained and makes their momentum measurement with a resolution of 1% at $p_\mathrm{T} \approx 1$ GeV/c^2 increasing to 3.5% at $p_\mathrm{T} \approx 100$ GeV/c^2, possible [33].
Furthermore, the TPC allows for charged particle identification by measuring the energy loss of a particle per track length ($\mathrm{d}E/\mathrm{d}x$) and the particle momentum [27].

3.3   Time of Flight detector

The Time of Flight (TOF) detector [26] has an internal radius of ≈ 370 cm and an outer radius of ≈ 399 cm. Like the TPC, TOF covers the mid-rapidity-region ($|\eta| < 0.9$) and the full azimuthal angle. The TOF detector is built of Multi-gap-Resistive Plate chambers (MRPC), best suited for the desired intrinsic time resolution of ≈ 100 ps in the ALICE experiment.

MRPCs offer a high and uniform electric field over the full gaseous volume. A charged particle traversing these chambers ionizes the gas and starts an avalanche of electrons, which will generate a signal on the readout cathode. The total signal is then the sum of all the signals from the gaps [34]. The working principle of an

19
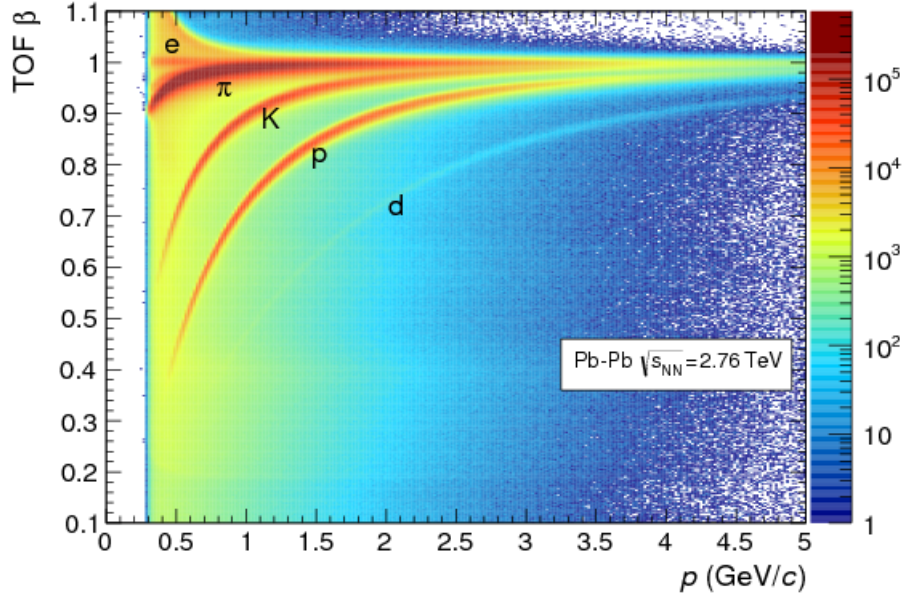
Figure 3.5: Velocity β of charged particles as function of the momentum p for Pb-Pb collisions at $\sqrt{s_{NN}}$ = 2.76 TeV. Image taken from [27].

MRPC used in TOF is shown in 3.4.

Particle identification in the TOF detector is based on the measurement of the time of flight of a particle. With known time of flight t, momentum p and track length L, the mass of the particle can be calculated in the following way [35]:

$$m = \frac{p}{c}\sqrt{\frac{c^2 t^2}{L^2} - 1}. \tag{9}$$

The TOF detector distinguishes electrons from kaons and protons up to $p_T \simeq 2.5$ GeV/c and $p_T \simeq 4$ GeV/c respectively as shown in Figure 3.5.

4   Data Analysis

The goal of this analysis is the measurement of the cross-section of electrons from semi-leptonic heavy-flavour hadron decays. In a first step, general event selection criteria are applied to the analysed sample. The second step of the analysis consists of selecting a sample of high-quality tracks through proper criteria. The third step consists of applying particle identification (PID) using the TOF and TPC detector information in order to select the inclusive electron candidate sample. The yield of electrons from semi-leptonic heavy-flavour hadron decays is then computed by subtracting the contribution of electrons that do not originate from open heavy-flavour hadron decays. The dominant background sources are Dalitz decays of light neutral mesons and photon conversions in the detector material. Finally, the yield of electrons from heavy-flavour hadron decays is corrected for the acceptance and reconstruction efficiency.

The cross-section is then compared to perturbative QCD models, like FONLL. Finally, this measurement serves as a reference to measure the nuclear modification factor (R_{AA}) in Pb-Pb and Xe-Xe collisions.

4.1   Data set and Monte Carlo simulations

In this analysis, a minimum bias (MB) sample of pp collisions at $\sqrt{s}$ = 5.02 TeV was used. The minimum bias trigger used in this data sample requires a signal in both of the V0 detectors above a certain threshold.

Since the SDD is a rather slow detector compared to the other silicon detectors in the ITS, a large fraction of events were recorded without the information from the SDD. Accordingly to this, there exist two versions of the reconstructed data, one with the information of the SDD and another one without it. In this analysis, the reconstructed data without the SDD is used, since it offers larger statistics because all events are included, also those with available SDD information, but not used in the reconstruction step. The total number of events analysed in this thesis consist of about 1000M MB events.

For this analysis, two different Monte Carlo samples are used. The minimum bias Monte Carlo (MC) samples (LHC17l3b-fast & LHC17l3b-Cent-woSDD) were produced using the PHYTHIA generator [36, 37] and transport code GEANT3 [38], which will be used to correct the spectrum of electrons coming from decays of photons and neutral mesons. An additional MC sample (LHC18a4b2) also based on the PHYTHIA generator and GEANT transport code is used, in which each simulated pp event contains a $c\bar{c}$ or $b\bar{b}$ pair and heavy-flavour hadrons are forced to decay semi-leptonically. This MC sample has been used to minimize the statistical uncertainty on the reconstruction efficiency.

21

Table 1: Summary of the data samples and Monte Carlo simulations used in this analysis.

Period/Sample	Number of events	Additional information
Data		
LHC17p-fast & LHC17p-CENT-woSDD	1000 M	pp, $\sqrt{s}$ = 5.02 TeV, minimum bias, 43 runs, reconstruction pass 1
Monte Carlo simulations		
LHC18a4b2	125 M	PYTHIA HF enriched production, GEANT
LHC17l3b-fast & LHC17l3b-cent-woSDD	220 M	PYTHIA, GEANT, minimum bias

A summary of all the data and Monte Carlo samples used in the analysis is provided in Table 1.

4.2 Event selection

The data set analysed in this thesis contains around 1000M events selected via a minimum bias trigger. The condition of the trigger is also fulfilled by multiple scattering between the proton beam and the gas inside the beam pipe. Furthermore, some of the events are occurring far away from the center of the central barrel, difficult to reconstruct correctly, since the produced particles move outside the detector acceptance.

This kind of events is removed by requiring the interaction vertex to be within 10 cm around the center of the detector in the direction of the beam. The interaction vertex is reconstructed using at least two global tracks, reconstructed with TPC and ITS. These event selection criteria are satisfied approximate by 88% (881M) of all events.

4.3 Track selection

Electron candidates are required to fulfill the track selection criteria summarized in Table 2. Tracks need to have at least a transverse momentum p_T of 0.3 GeV/c to reach the TOF detector in the magnetic field (B = 0.5 T) provided by the solenoid magnet. Nevertheless, the cross section of electrons coming from decays of heavy-flavour hadrons shown in this thesis starts at minimum p_T of 0.5 GeV/c, because of the very small signal over background ratio and the low and steep efficiencies to find electrons from decays of photons and neutral mesons.

This makes the analysis below = 0.5 GeV/*c* unreliable and results in large statistical uncertainties.

Each track needs to have at least 100 TPC clusters, out of a maximum of 159, used for tracking among which a least 80 clusters have to be also used for the energy loss calculation. The requirement on the number of clusters is used to improve the discrimination between electrons and hadrons since on average electrons generate a larger number of clusters. This can be explained by the fact that electrons, always at the Fermi plateau, have a larger energy deposition than minimum ionizing particles. Hadrons reach the Fermi plateau only for momenta larger than p = 20 GeV/*c*. Fake tracks comprise a significant number of TPC clusters originating from more than one charged particle trajectory were rejected by requiring that the χ^2 per degree of freedom (ndf) of the track fit in the TPC is smaller than four. Since clusters are not shared between tracks, the ratio of found over findable clusters has to be larger than 60%, where findable cluster includes all geometrically possible clusters which can be assigned to a track.

The track selection criteria in the ITS are used to reduce the number of electrons from photon conversions in the material. Therefore, each track needs to have a signal in at least three layers of the ITS, out of a maximum of four since the SDD layer was not used for tracking, and in both of the SPD layers. To reduce the number of electrons from the background, the distance of closest approach (DCA) of tracks to the primary vertex is required to be smaller than 2 cm (1 cm) in the longitudinal (radial) direction.

Kinks are particles which suddenly change their direction of flight, e.g. because of bremsstrahlung effects. The tracks before this change are called kink mothers, after the change kink daughters. Both are excluded from the analysis.

The analysis is restricted to tracks within $|\eta| < 0.8$ to avoid the edges of the detectors, where the systematic uncertainties related to particle identification increase.

4.4 Electron candidates

For particle identification, the TOF and TPC detector information is used. In order to discriminate between different particle species, the commonly $n\sigma$ quantity is used. It is defined as the deviation of the measured signal S_α in the detector α, e.g. d*E*/d*x* in the TPC and the time-of-flight in TOF, from that expected $\hat{S}_\alpha^i$ for particle i in terms of the detector resolution σ_α^i:

$$n\sigma_\alpha^i = \frac{S_\alpha - \hat{S}_\alpha^i}{\sigma_\alpha^i}. \tag{10}$$

Table 2: Summary of track selection criteria for electron candidates in the TPC-TOF and TPC-only analysis.

Track and PID cuts	TPC-TOF analysis	TPC only analysis
p_T^{min}	0.5 GeV/c	0.5 GeV/c
$|\eta|$	< 0.8	< 0.8
Number of TPC clusters	≥ 100	≥ 100
Number of TPC $\frac{dE}{dx}$ clusters (PID)	≥ 80	≥ 80
Number of ITS hits	≥ 3	≥ 3
χ^2/clusters of the track fit in the TPC	< 4	< 4
Ratio found / findable TPC clusters	≥ 0.6	≥ 0.6
Requirement of hits in the SPD layers	both layers	both layers
DCA to the primary vertex in xy	< 1 cm	< 1 cm
DCA to the primary vertex in z	< 2 cm	< 2 cm
Kink mothers and daughters	excluded	excluded
TOF t - $<$ TOF t $>|_{el}$	(-3 to 3 σ)	-
TPC $\frac{dE}{dx}$ - $<$ TPC $\frac{dE}{dx}>|_{el}$	$(-0.5 + \mu(p)$ to $3.0)\,\sigma$	$(0 + \mu(p)$ to $3)\,\sigma$

Since the analysis focus on electrons, i = e.

Up to a momentum of 3 GeV/c, the TOF detector is essential to remove the contamination due to kaons, protons and deuterons, as shown in Figure 3.5 and 4.1. Above 3 GeV/c, TOF is not able to discriminate between electrons and hadrons anymore. Since it reduces the acceptance and therefore the statistics of tracks, it is not used anymore. To extend the analysis to larger p_T, only the particle identification capabilities of the TPC detector are used. The analysis where TPC and TOF are used is performed in the p_T interval between 0.5 - 6 GeV/c, and is referred to later in the text as "TPC-TOF". The analysis where only the TPC is used is performed in the p_T interval between 2 - 10 GeV/c is referred to as "TPC-only". The TPC-TOF analysis between 3 - 6 GeV/c is performed to have an overlapping p_T interval between both strategies in order to check that both analyses strategies provide consistent results.

For the TPC-TOF strategy, electrons are selected by rejecting all particles outside $3n\sigma^e_{TOF}$, shown in Figure 4.1. This helps to remove a large fraction of hadrons below 3 GeV/c. The $n\sigma^e_{TPC}$ distributions, before and after TOF selection, are shown in the upper and lower panel of Fig. 4.2, respectively. By definition, the electrons should be populated around $n\sigma^e_{TPC} \approx 0$, while hadrons are mainly not. Therefore,
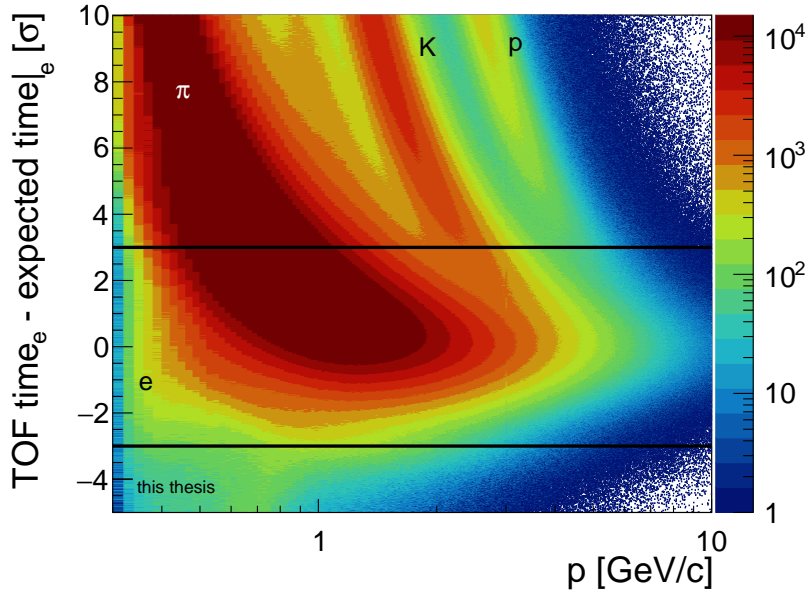
Figure 4.1: $n\sigma^e_{TOF}$ as function of the tracks momentum p. Tracks inside the black lines are selected as electron candidates in the TPC-TOF analysis.

an additional selection on the $n\sigma^e_{TPC}$ is applied to increase the purity of the electron sample, as described in the next paragraph.

The usage of the selection based on the $n\sigma^e_{TPC}$ is based on the assumption that the mean and width of the electron distribution are located at zero and unity. In the analysed data sample a shift of that expectation was observed. In the data taking period, the gas gain in the TPC chambers was relatively low, leading to difficulties in describing the behaviour of the energy loss by electrons correctly. Accordingly, the electron spline does not describe the distribution correctly and leads to a deviation from the expectation.
The position of the electron mean and width was extracted directly from data by applying the TPC-TOF selection criteria to all tracks (shown in Table 2), considering the $n\sigma^e_{TPC}$ distributions for different track momentum p and fitting the electron distribution with a Gaussian function, which is expected since the signal is given in $n\sigma^e_{TPC}$. An example of one Gaussian fit is shown in Fig. 4.3 [panel (c)]. In addition, Fig. 4.3 shows the $n\sigma^e_{TPC}$ distributions, after TOF selection, together with the mean and width extracted from the Gaussian fits. In the right panel, the electron mean, in larger momentum bins, is shown together with a function used to parametrize it.
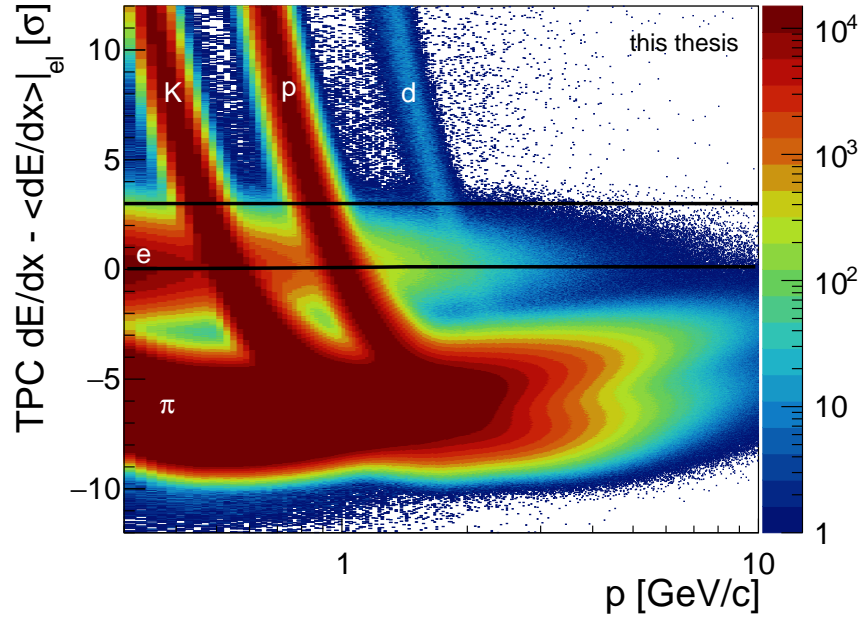
((a)) $n\sigma_{TPC}^{e}$ before TOF selection.
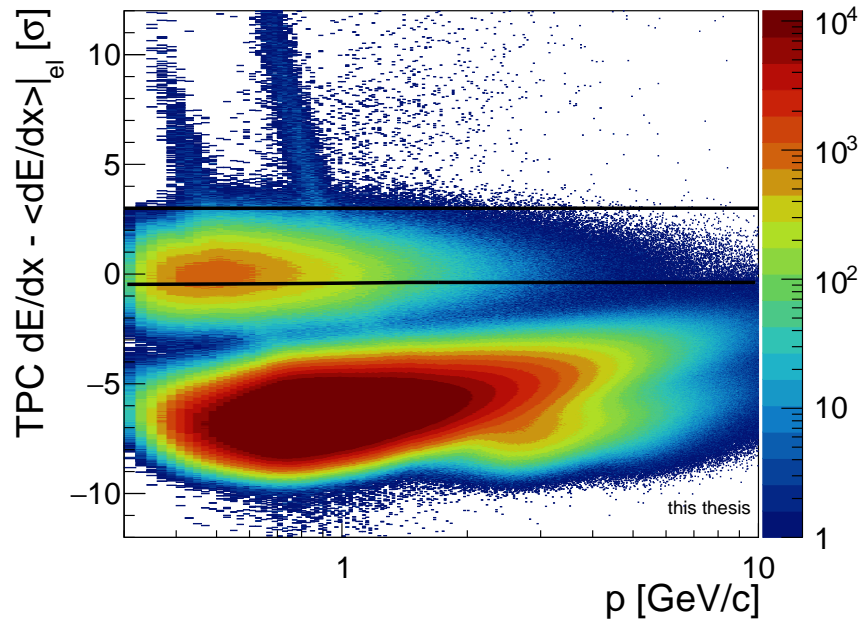
((b)) $n\sigma_{TPC}^{e}$ after TOF selection.

Figure 4.2: $n\sigma_{TPC}^{e}$ as a function of the track momentum before TOF selection [panel (a)] and after TOF selection [panel (b)]. Tracks inside the black lines are selected as electron candidates in the TPC-TOF [panel (b)] and TPC only [panel (a)] analysis, respectively.

For low track momentum, a linear dependence of the electron mean as function of the momentum is observed which gets flat for track momenta above ≈ 1.5 GeV/c. Since later in this analysis, the TPC PID efficiency is corrected with a constant factor, by expecting the electron distribution to be of Gaussian shape, with mean zero and width unity, we would clearly introduce a bias in the efficiency correction, because of the shifted electron mean in the analysed data sample. Accordingly, in order to keep the constant TPC PID efficiency correction, a momentum dependent selection in the TPC is introduced. The shift in the TPC selection is changed by a parametrization function of the electron mean, shown in Fig. 4.3 [panel (b)]:

$$\mu(p) = min(0.12, 0.017 + 0.071 \cdot p). \tag{11}$$

A parametrization function of the electron width is not needed since above p = 0.5 GeV/c, the width is equal to unity. Therefore, in the TPC-TOF analysis, electron candidates are selected within -0.5 + $\mu(p) < n\sigma_{TPC}^{e} < 3$, corresponding to a TPC PID efficiency of 70%.
A tighter selection in the TPC ($0 + \mu(p)$ $n\sigma_{TPC}^{e} < 3$), TPC PID efficiency of 50%, is required for the TPC only analysis in order to reduce the contamination due to pions at large momentum since the relative difference in the energy loss for electron and pions reduces as function of momentum.

4.5   Hadron contamination

4.5.1   Hadron contamination for the TPC-TOF analysis

The tracks selected via the selection criteria described in sections 4.3 and 4.4 still contain hadrons, contaminating the inclusive electron sample. In order to remove the remaining hadrons, the $n\sigma_{TPC}^{e}$ distribution is fitted in different momentum intervals and from these fits, the hadron contamination is computed.

Electrons are described by a Gaussian function, while pions are described by a convolution of a Landau curve and an exponential function over the whole momentum range p. The Landau function is used since a Gaussian function is not able to describe the pion tail well and would lead to an underestimation of the contamination due to pions. The exponential function is needed as a correction function. The TPC signal corresponds to several measurements of the energy loss in a given track length. Since charged particles can loose a relatively large amount of energy due to δ- electrons, the TPC signal follows a Landau distribution. To remove the large tail of the TPC distribution, a truncated mean is used, which nevertheless modifies the distribution. The modification is described by the above mentioned exponential function. This effect is more pronounced for pions than

(a)

(b)

(c)
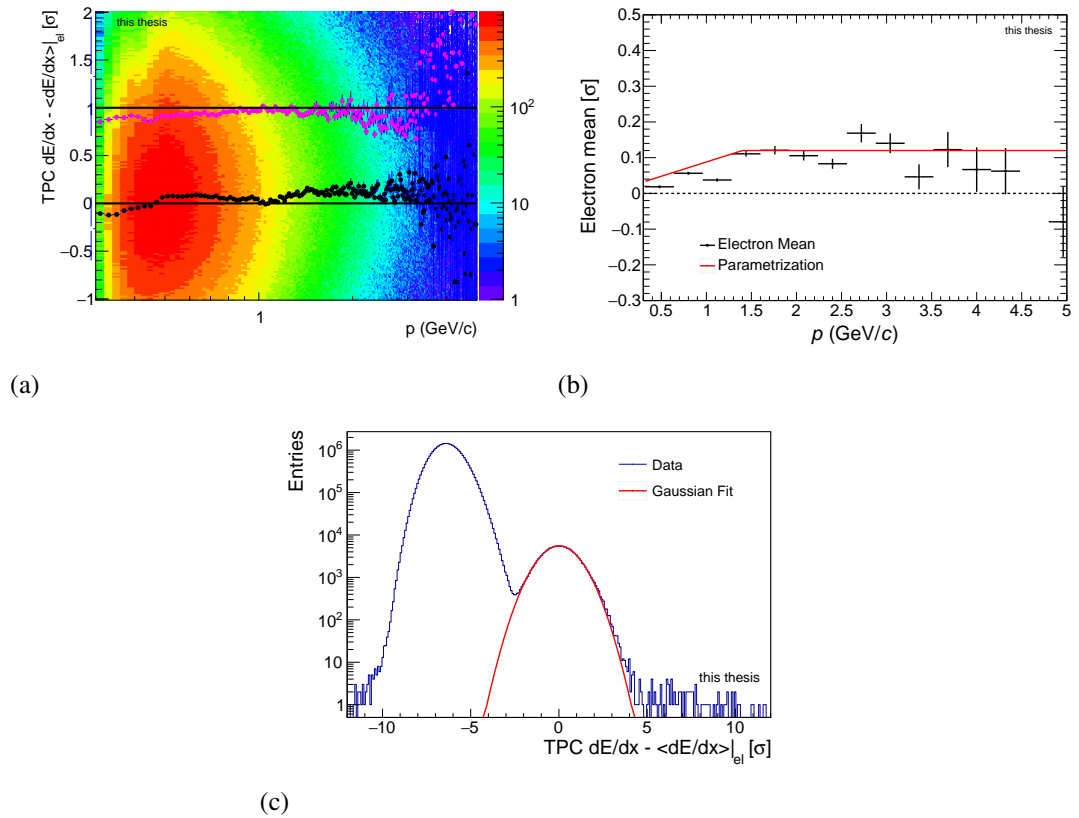
Figure 4.3: $n\sigma^e_{TPC}$ as function of the track momentum after TOF selection together with the electron mean and width extracted from the Gaussian fits [panel (a)] and the electron mean together with a parametrization function [panel (b)]. In addition, an example of an Gaussian fit to extract the electron mean is shown [panel (c)].

(a)   (b)
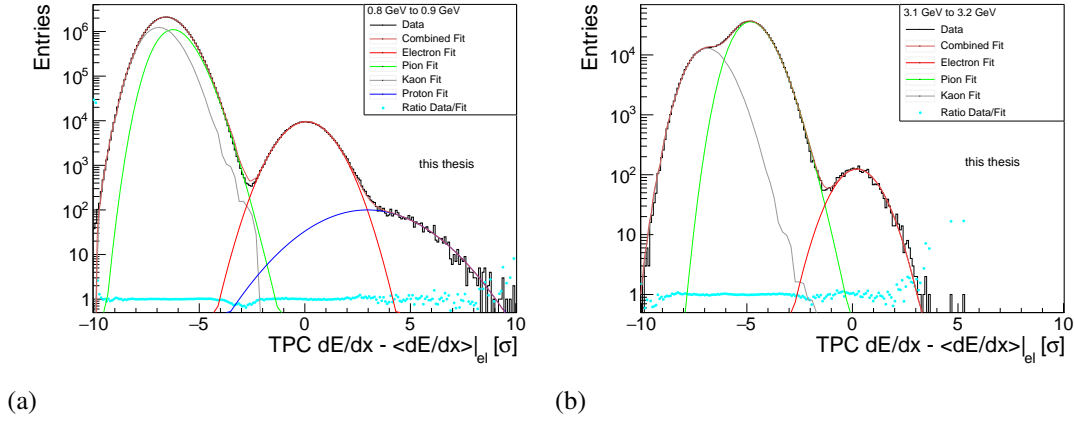
Figure 4.4: Distribution of the $n\sigma^e_{TPC}$ for the momentum slices between 0.8 to 0.9 GeV/c [panel (a)] and 3.1 to 3.2 GeV/c [panel (b)] with the fit for electrons (red), pions (green), kaons (grey), protons (blue) and the ratio between fit and data (cyan).

for electrons. A more detailed description can be found in [39].

As it is shown in figure 4.2 [panel (b)], there is still a large number of protons which cross the electron band around 1 GeV/c and lead to an increase of the hadron contamination. A Gaussian function is used to describe the protons crossing the electron band at low momentum. The kaons crossing the electron band around 0.5 GeV/c shows a stronger suppression compared to the proton line and does not lead to a significant contamination at this momentum. For larger momentum, the energy loss of protons and kaons gets quite similar and therefore one function is used to describe them [40]. This function is a template, which was extracted from data to fit the distribution of kaons and protons at large momentum simultaneously. The $n\sigma^e_{TPC}$ distribution for different momentum together with the fits of electrons (red), pions (green), kaons (grey), protons at low momentum (blue) is shown in the Figure 4.4. The ratio between fit and data (cyan) is also reported in the plots.

The hadron contamination C(p) for each momentum slice is calculated considering the following function:

$$C(p) = \frac{\int_{x_{\min}}^{x_{\max}} (f_\pi(x) + f_K(x) + f_p(x))dx}{\int_{x_{\min}}^{x_{\max}} (f_\pi(x) + f_K(x) + f_p(x) + f_{el}(x))dx} \qquad (12)$$

where x_{min} = -0.5 + $\mu(p)$ and x_{max} = 3 are the selection in the TPC PID for the

29
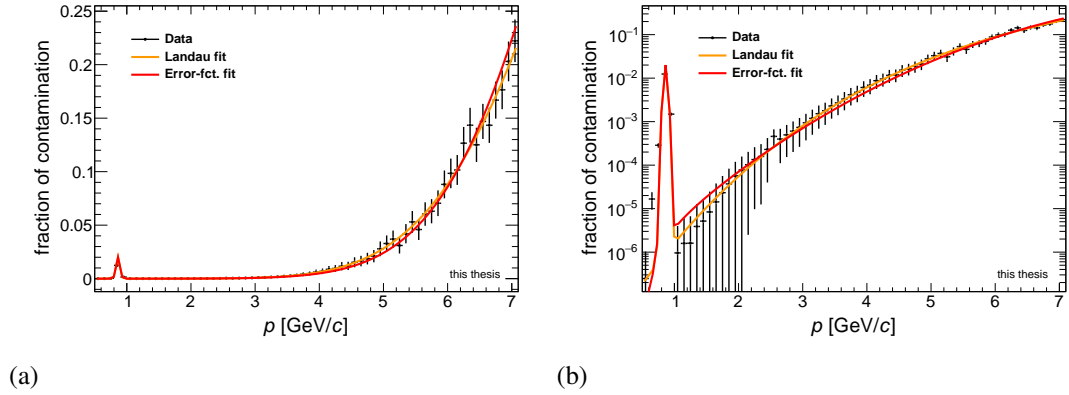
Figure 4.5: Hadron contamination as function of track momentum in linear [panel (a)] and logarithmic [panel (b)] scale together with two different parametrization functions for the TPC-TOF analysis.

TPC-TOF analysis and f_i the fit function for the particle type i, described before. Figure 4.5 shows the hadron contamination $C(p)$ as function of the track momentum in linear and logarithmic scale. The hadron contamination for the TPC-TOF analysis strategy starts to be important above momenta of 4 GeV/c reaching a maximum at 7 GeV/c of 20 %. The protons crossing the electron line at approximately 1 GeV/c cause a contamination of about 1%.

Since the cross section in this thesis is given as function of the transverse momentum p_T, the hadron contamination has to be transferred from a function of p to p_T. This is done by applying a weight to each track with momentum p and transverse momentum p_T. These weights are given by the parametrization function of the hadron contamination, shown in Figure 4.5. A Landau-plus-Gaussian function or an Error plus Gaussian function are used to describe the hadron contamination as function of the track momentum. The Gaussian function is needed to describe the contamination due to protons accurately. Since the Landau function describes the low momentum better than the Error function, the following function is used as parametrization:

$$C(\mathrm{p}) = 6.63 \cdot \mathrm{Landau}(p, 14.29, 3.53) + 0.02 \cdot \mathrm{Gaus}(p, 0.88, 0.03) \qquad (13)$$

The Error function will be used to estimate the systematic uncertainty due to the hadron contamination.
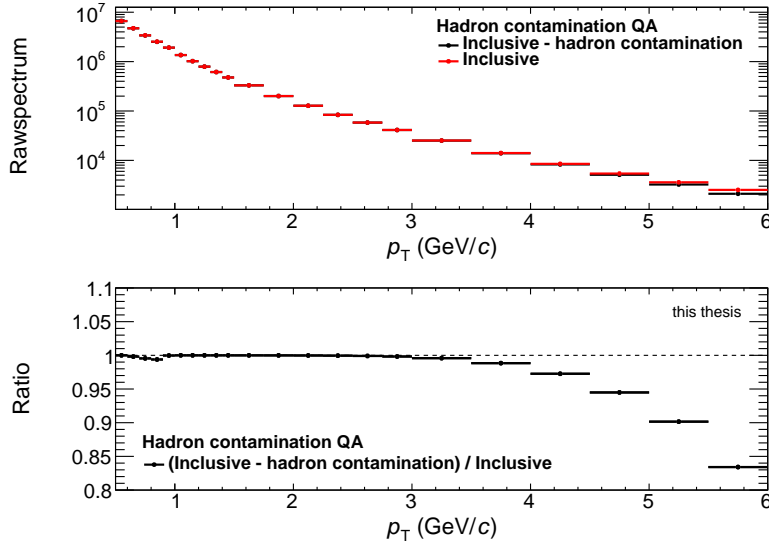
Figure 4.6: Raw yield of inclusive electrons before (red) and after (black) subtraction of the hadron contamination as function of p_T for the TPC-TOF analysis.

Figure 4.6 shows the inclusive electron yield before (red) and after (black) the subtraction of the hadron contamination.

4.5.2   Hadron contamination for the TPC only analysis

The estimation of the hadron contamination for the TPC only analysis follows the same procedure as for the TPC-TOF analysis but starting from a momentum above 2 GeV/c. As shown in Figure 4.2 [panel (b)], deuterons start to cross the electron band at a momentum of approximately 2 GeV/c. During the crossing, it is difficult to fit an appropriate function to the deuteron, since the electron and deuteron distributions overlap. In the case of the proton line in the TPC-TOF analysis (described in the last section) the proton line was largely suppressed and therefore the exact position of the proton distribution could be judged from Figure 4.2 [panel (b)]. In the deuteron case, the suppression is much lower, and therefore the contamination due to deuterons much higher. Therefore the usage of a fit function, which deviate from true deuteron distribution, could have a not negligible effect on the hadron contamination. Correspondingly, the position of the deuteron distribution is extracted directly from data and then fixed for the hadron contamination estimation.

The position of the deuteron distribution is extracted in the following way. In the first step, a sample of deuterons is needed, which is obtained by using the TOF

31

(a)　　　　　　　　　　　　　　　　　　　(b)
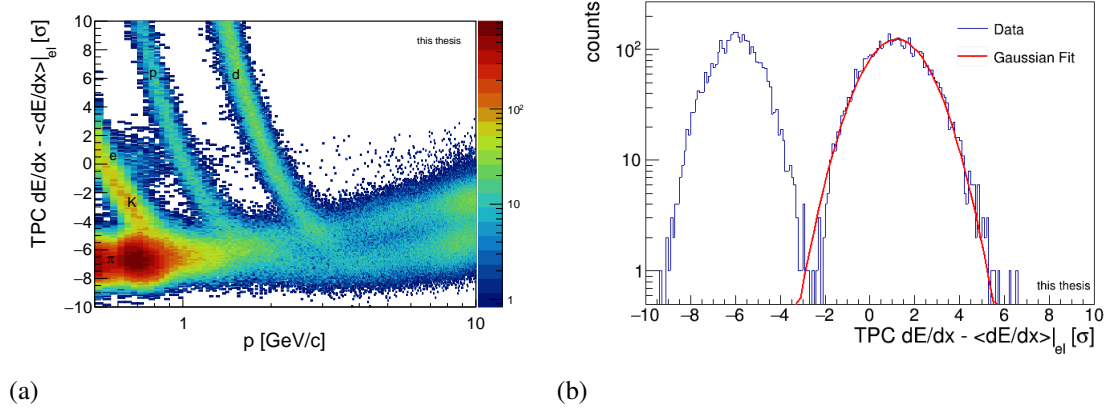
Figure 4.7: $n\sigma^{e}_{TPC}$ for tracks selected as deuterons via TOF as function of the track momentum [panel (a)] and the projection of $n\sigma^{e}_{TPC}$ in the momentum slices 1.8 - 2.0 GeV/*c* simultaneously with the Gaussian fit [panel (b)].

detector. Tracks which satisfy the track selection criteria in Table 2 and are within $-3 < n\sigma^{d}_{TOF} < 3$ are selected as deuterons. Figure 4.7 [panel (a)] shows the tracks satisfying the selection criteria as function of the track momentum and $n\sigma^{e}_{TPC}$. In order to extract the position of the deuteron distribution, the $n\sigma^{e}_{TPC}$ distribution shown in Figure 4.7 is projected within a given momentum interval $\Delta p = 0.2$ GeV/*c* in the momentum range where the deuteron line crosses the electron line (1.6 GeV/*c* < p < 2.4 GeV/*c*). Figure 4.7 [panel (b)] shows the projected distribution together with the Gaussian fit, from which the mean and width is extracted. This mean and width are now used to fix the deuteron distribution for the computation of the hadron contamination.

The hadron contamination is now evaluated in the same way as for the TPC-TOF analysis. The electron distribution is described via a Gaussian function, the pion distribution via a Landau function convoluted with an exponential function, whereas protons and kaons are described simultaneously via a template extracted from data, since there d*E*/d*x* values are quite similar in the momentum range between 2 - 10 GeV/*c*. The deuteron distribution is described via a Gaussian function. The $n\sigma^{e}_{TPC}$ distribution for different momentum slices together with the fits of electrons (red), pions (green), kaons + protons (grey) and deuterons (blue) and the ratio between fit and data (cyan) is shown in Figure 4.8.

The hadron contamination $C(p)$ for each momentum is now calculated with the following function:

(a)

(b)

(c)
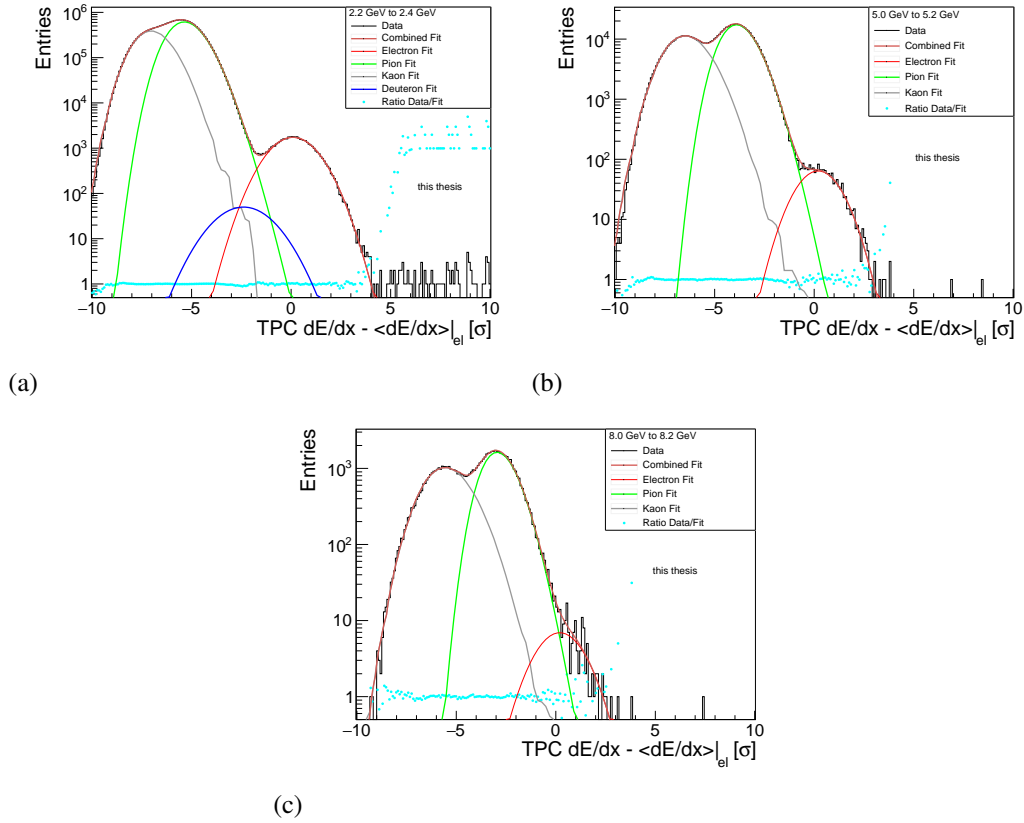
Figure 4.8: nσ^{e}_{TPC} distribution for the momentum slices between 2.0 - 2.2 GeV/*c* [panel (a)], 5.0 - 5.2 GeV/*c* [panel (b)] and 8.0 - 8.2 GeV/*c* [panel (c)] for the TPC only analysis with the fit for electrons (red), pions (green), kaons + protons(grey), deuterons (blue) and the ratio between fit and data (cyan).

(a)   (b)
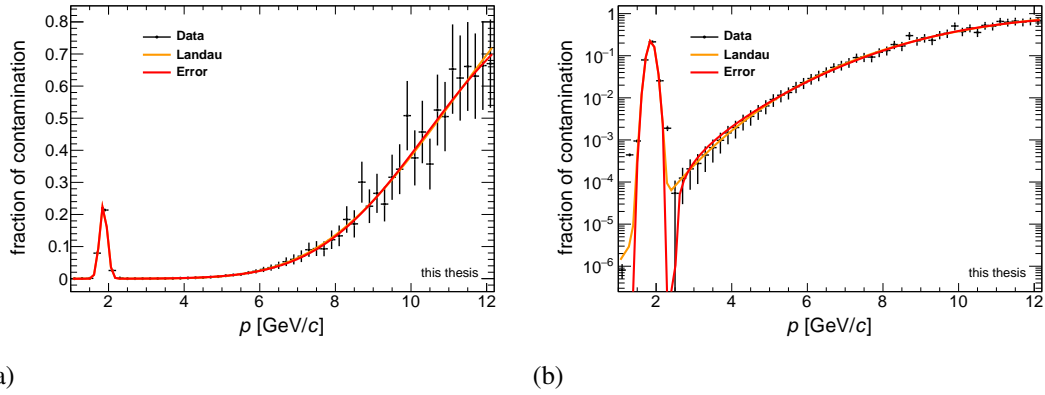
Figure 4.9: Hadron contamination as function of p in linear (left) and logarithmic (right) scale with two different parametrization functions for the TPC only analysis.

$$C(\mathrm{p}) = \frac{\int_{x_{\min}}^{x_{\max}}(f_\pi(x) + f_{K+p}(x) + f_D(x))dx}{\int_{x_{\min}}^{x_{\max}}(f_\pi(x) + f_{K+p}(x) + f_D(x) + f_{el}(x))dx} \tag{14}$$

where $x_{min} = 0 + \mu(p)$ and $x_{max} = 3$ are the selection criteria in the TPC and f_i the fit functions used for the different particle species, described above. The hadron contamination as function of the momentum is shown in linear and logarithmic scale in Figure 4.9. The hadron contamination due to the deuterons is 20% at 1.9 GeV/c and reaches a maximum of 70% at large momentum, due to pion, kaons and protons approaching again the electron line, shown in Fig. 4.2 [panel (a)].
A Landau function best describes the hadron contamination $C(\mathrm{p})$ as function of the track momentum:

$$C(\mathrm{p}) = 4.82 \cdot \mathrm{Landau}(p, 15.95, 3.89) + 0.23 \cdot \mathrm{Gaus}(p, 1.87, 0.11) \tag{15}$$

The inclusive electron yield before (red) and after (black) the subtraction of the hadron contamination is shown in Figure 4.10. When comparing the ratio between both yields, we observe that at $p_T = 2$ GeV/c the hadron contamination as function of p_T due to deuterons is below 1%. This can be explained by the fact that the hadron contamination as function of p needs to be transformed to a contamination as function of p_T, which is done by applying a weight to each track with momentum p and transverse momentum p_T, and since for each track the following relation is valid: $p_T \leq \mathrm{p}$.
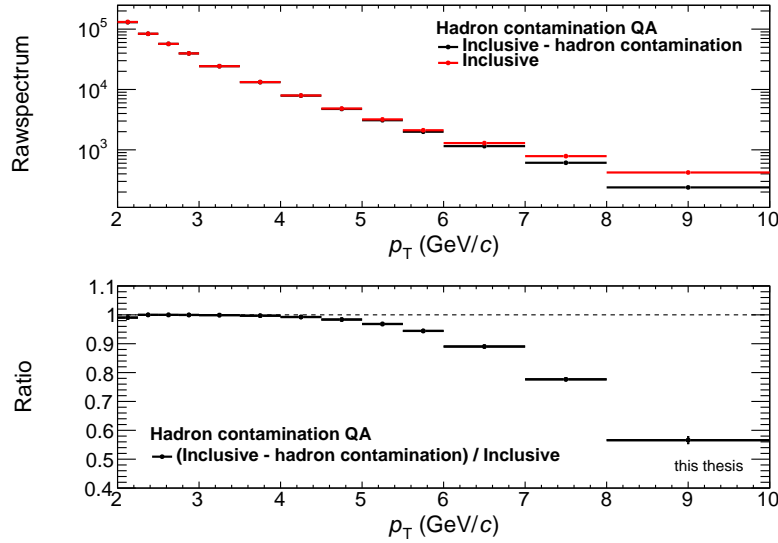
Figure 4.10: Raw yield of inclusive electron candidates before (red) and after (black) subtraction of the hadron contamination as function of p_T for the TPC only analysis.

4.6 Electrons from background sources

The raw spectrum obtained after removing the hadron contamination still contains electrons from different sources, other than from the semi-leptonic decays of heavy-flavour hadrons. These background sources are

- Dalitz decays of light neutral mesons (π^0, η and $\eta^{'}$)

- conversions of photons in the detector material

- Di-electron decays of light vector mesons (ρ, ω and Φ)

- Di-electron decays of heavy quarkonia (J/ψ and Υ)

- weak $K \rightarrow e\, \pi\, \nu$ (K_{e3}) decays

The most important background sources are Dalitz decays of light neutral mesons and photon conversions. These electrons are always produced as electron-positron pairs with a small invariant mass m_{ee}. Such a correlation does not hold for electrons from semi-leptonic decays of heavy-flavour hadrons. This property is used in the invariant mass method to estimate the background due to electrons coming from Dalitz decays of light neutral mesons and photon conversions.

35

Electrons from Dalitz decays of light neutral mesons and photon conversions are reconstructed statistically by pairing an electron (positron) track with opposite charge tracks identified as positrons (electrons), called associated electrons in the following, from the same event selected with the requirements listed in Table 3. These track criteria are less restrictive than the criteria applied to select the electron candidates (listed in Table 2), to maximise the probability of finding the true associated electron pairs.

In order to include all electrons from photon conversions and Dalitz decays of π^0, the invariant mass of these unlike sign pairs is restricted to be lower than 140 MeV/c^2. Pairs from other light mesons (η, η') are only included for unlike sign pairs with an invariant mass lower than 140 MeV/c^2. However, due to the small contribution of other light mesons to the electron background, the difference is negligible [41].

The pool of unlike sign pairs contains pairs of electrons from decays of the above mentioned sources and many uncorrelated, random pairs. To estimate the contribution of these random pairs, the invariant mass distribution of the like sign pairs is used. Each electron track is paired with an associated track of the same sign.

The yield of electrons coming from Dalitz decays and photon conversions is now evaluated for each p_T interval of the inclusive electron candidates using:

$$N_{\text{photonic,raw}}(p_T) = N_{\text{ULS}}(p_T) - N_{\text{LS}}(p_T), \tag{16}$$

where N_{ULS} and N_{LS} are the yields of unlike and like sign pairs. Figure 4.11 shows the yield of like and unlike sign pairs in the momentum interval of 0.5 - 0.6 p_T of the inclusive electron candidates.

Due to detector acceptance and tracking inefficiencies, not all electrons from Dalitz decays and photon conversions in the inclusive electron sample are tagged with this method. Therefore, the raw yield of tagged electrons is corrected for the efficiency to find the associated electron (positron), hereafter called tagging efficiency. The tagging efficiency ε_{tag} is calculated using the minimum bias Monte Carlo sample, since it offers a larger statistics of Dalitz decays and pair production, compared to the enhanced MC sample, where heavy-flavour hadrons are forced to decay semi-leptonically. The tagging efficiency is now calculated as the ratio of electrons for which the partner is found in the pool of associated tracks (N_{found}) and all electrons from Dalitz decays and photon conversions, passing the selection criteria listed in Table 2, as function of p_T of the inclusive track candidates:

$$\varepsilon_{\text{tag}}(p_T) = \frac{N_{\text{found}}(p_T)}{N_{\text{photonic}}(p_T)} \tag{17}$$

Table 3: Summary of track selection criteria for associated tracks

Track and PID cuts	Associated candidates
p_{T}^{min}	0.1 GeV/c
$|\eta|$	< 0.8
Number of TPC clusters	≥ 60
Number of TPC $\frac{dE}{dx}$ clusters (PID)	≥ 60
Number of ITS hits	≥ 2
χ^2/clusters of the momentum fit in the TPC	< 4
Ratio found / findable TPC clusters	> 0.6
Requirement of hits in the SPD layers	kAny
DCA to the primary vertex in xy	< 1 cm
DCA to the primary vertex in z	< 2 cm
Kink mothers and daughters	excluded
TOF t - < TOF t > $|_{el}$ in between	not used
TPC $\frac{dE}{dx}$ - < TPC $\frac{dE}{dx}$ > $|_{el}$ in between	-3 to 3 σ
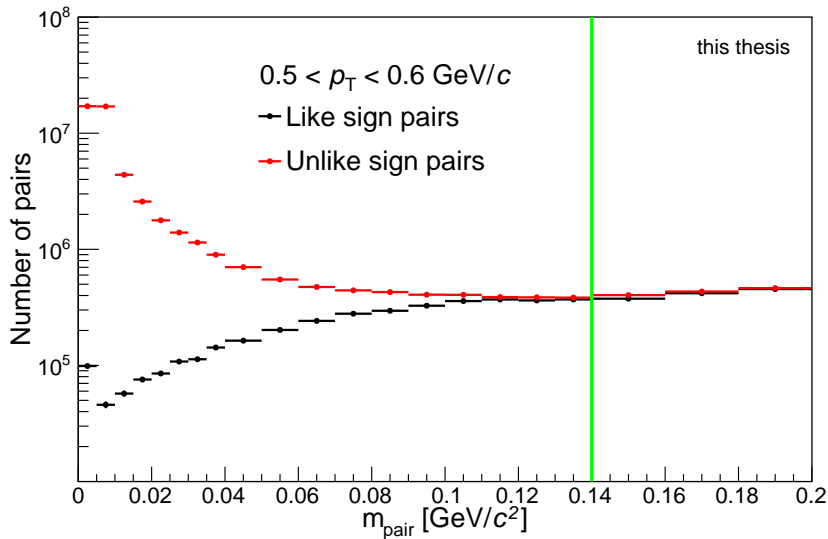
Figure 4.11: Invariant mass distribution of like sign (black) and unlike sign (red) pairs in the p_{T} interval of the inclusive electron candidates from 0.5 - 0.6 GeV/c. The green line corresponds to the selection criterion of only selecting pairs with an invariant mass lower than $M_{ee} = 140$ MeV/c^2.
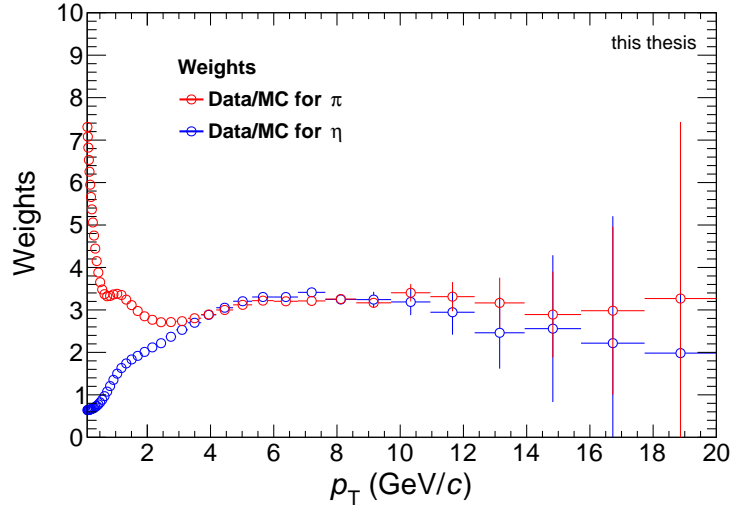
Figure 4.12: Weight factors for the π^0 (red) and η (blue) distribution as function of p_T of the mother meson.

Since ε_{tag} depends only on the p_T-shape of the mother particles (π^0, η) it has to be guaranteed that the distribution of these mother particle as function of p_T in Monte Carlo reflects the one measured experimentally. The simulated π^0 and η p_T-distributions are weighted so as to match the measured $\pi^{\pm}$ p_T- spectra [42] and the corresponding η p_T- spectra respectively. In this analysis, the spectrum of charged pions is used to calculate the weight factors, since they provide a lower statistical uncertainty than the spectrum of neutral pions. For medium and large transverse momentum the approximation is valid using the argument of isospin symmetry, where the pion family forms a triplet. At low transverse momentum, decays of resonance can break this symmetry. Therefore, as a cross check, also weights using the neutral pion spectrum are used. At low transverse momentum a difference of $\approx 3\%$ at the level of the final production cross-section of electrons from semi-leptonic decays from heavy flavour hadrons was observed (see Fig. A.1). Figure 4.12 shows the weights for the π^0 (red) and η (blue) distribution applied to the π^0 and η distribution in Monte Carlo as function of p_T of the mother meson.

In Figure 4.13 the tagging efficiency as function of p_T of the inclusive electron candidates for the TPC-TOF and TPC only analysis is shown. They agree within statistical uncertainties, which is expected since the track selection criteria of the associated tracks are the same for both analyses. The statistics of tracks in the TPC only analysis is increased compared to the TPC-TOF analysis, but not changing the relative amount of found electron-positron pairs.
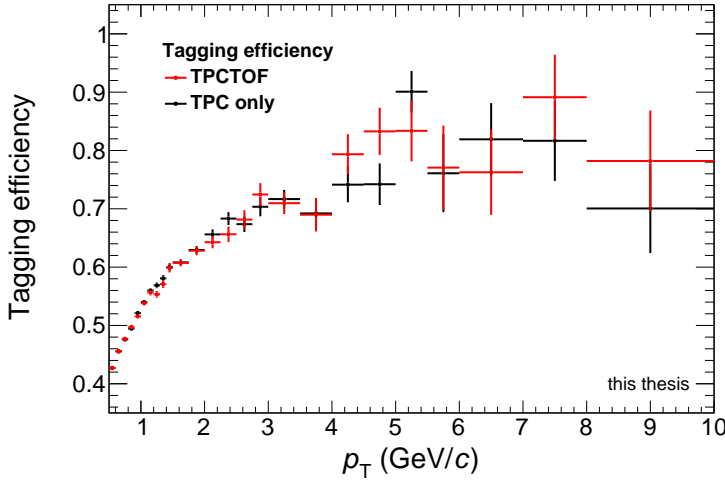
Figure 4.13: Tagging efficiency calculated from the minimum bias Monte Carlo sample for the TPC-TOF and TPC only analysis as function of p_T of the inclusive electron candidates.

The yield of electrons from Dalitz decays of light neutral mesons and photon conversions is now evaluated via:

$$N_{\text{photonic}} = \frac{N_{\text{ULS}} - N_{\text{LS}}}{\varepsilon_{\text{tag}}} \tag{18}$$

The raw yield of "non-photonic" electrons can now be calculated by subtracting the yield of electrons coming from Dalitz decays and photon conversions, from the inclusive yield. Figure 4.14 shows all spectra needed to calculate the raw yield of "non-photonic" electrons for the TPC-TOF and TPC only analyses, on the left and right side, respectively. The electrons from Dalitz decays and photon conversions have the largest contribution at low momentum and their contribution decreases for large momentum.

The yield of "non-photonic" electrons still contains electrons from di-electron decays of light vector mesons, heavy quarkonia and weak decays of kaons. The most dominant sources are J/ψ and K_{e3}. This subtraction is done after the correction for acceptance, efficiency and normalization. For completeness, they are described in this section.

39

(a)   (b)
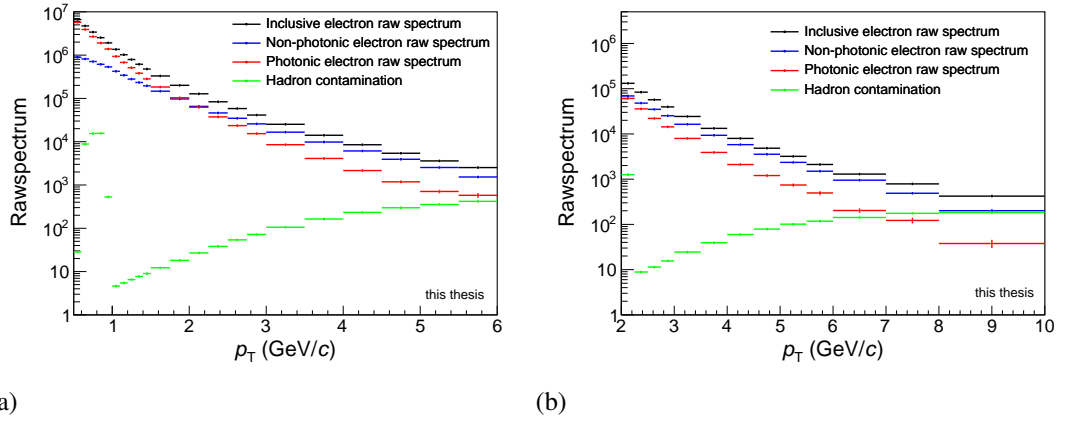
Figure 4.14: Decomposition of the inclusive raw spectrum into its components for the TPC-TOF [panel (a)] and TPC only [panel (b)].

The contribution from K_{e3} is obtained by multiplying the fully corrected photonic background with the following function

$$f(p_T) = 0.0125 \cdot exp(-2.0 \cdot log(2.5 \cdot p_T)) \qquad (19)$$

which describes the ratio of electrons from K_{e3} decays and from the photonic background. This function was extracted from MC and is valid in the momentum region discussed in this thesis. Since this ratio is valid for the pp collisions at $\sqrt{s}$ = 2.76 TeV and $\sqrt{s}$ = 7 TeV it is assumed that it is also true for pp collisions at $\sqrt{s}$ = 5.02 TeV.

The contribution of electrons from J/ψ decays is obtained using the spectral shape from the parametrization of the differential interpolated J/ψ cross sections in pp at $\sqrt{s}$ = 5.5 TeV [43]. The integrated cross section of electrons from J/ψ is then rescaled using the $\sqrt{s}$ dependence which is also obtained from [43] and subtracted from the remaining fully corrected "non-photonic" yield.

The contribution from di-electron decays of light vector mesons are negligible compared to contributions from the photonic sources [40].

4.7 Efficiency correction

The spectrum of "non-photonic" electrons still needs to be corrected the geometrical acceptance (ε_{geo}) of the detectors, the reconstruction efficiency (ε_{recon}) and the electron identification efficiency (ε_{eID}). All of them were obtained from the enhanced Monte Carlo simulation except the TPC PID efficiency, which was calculated as the integral of a Gaussian function with mean zero and width unity. In the TPC-TOF analysis, the TPC selection corresponds to a TPC PID efficiency

of 70%, whereas for the TPC only analysis it corresponds to a TPC efficiency of 50%.

Figure 4.15 shows the efficiency correction due to the track selection criteria (Table 2), the geometrical acceptance and the electron identification (expect TPC PID) as function of p_T of the "non-photonic electron spectrum for the TPC-TOF (red) and TPC only (black) analysis.
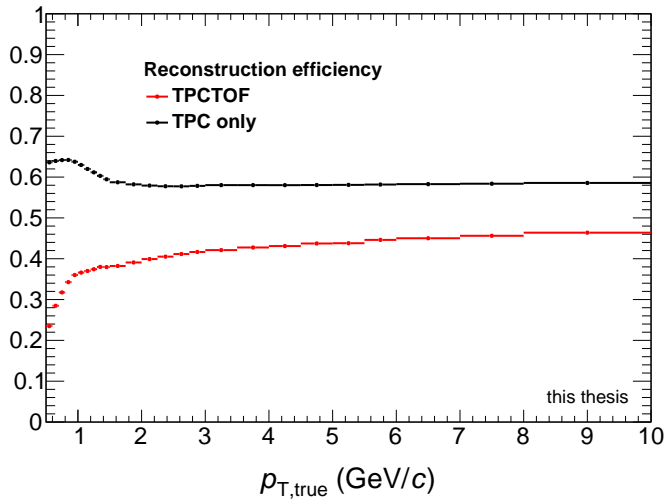
Figure 4.15: Reconstruction efficiency $\varepsilon_{\mathrm{recon}} \times \varepsilon_{\mathrm{geo}} \times \varepsilon_{\mathrm{eID}}$ as function of p_T for the TPC-TOF and TPC only analysis.

The reconstruction efficiency for the TPC-TOF case shows a steep rise for momenta below 1 GeV/c and flattens out for higher momenta. This behaviour is explained by the fact that tracks need to have at least a momentum of 0.3 GeV/c to reach the TOF detector. The reconstruction efficiency for the TPC only case is higher compared to the TPC-TOF case since the TOF detector has a smaller geometrical acceptance than the TPC. Furthermore, the TPC-TOF reconstruction efficiency is lower, because of the matching of tracks from the TPC to the TOF detector.

4.8 Normalization

The spectrum was normalized to the number of minimum bias events. The number of events was evaluated with the following formula:

$$N_{\text{MB}} = N_{\text{Vertex}} + f_{\text{Vertex}} \cdot N_{\text{no Vertex}} \tag{20}$$

where N_{Vertex} describes the number of events with a vertex from tracks surviving the event selection, f_{Vertex} describes the fraction of events passing the event selection and $N_{\text{no Vertex}}$ describes the number of events where no vertex from the track could be found. The second term of the equation is an estimate of events without tracks in the central barrel, but a signal in the V0 detectors. Since the minimum bias cross section was measured including such events, the second term is needed to allow for a correct normalization.

In addition to the normalization on the number of events, the yield of electrons coming from heavy flavour hadrons is normalized to unit rapidity by dividing with the rapidity range investigated in this analysis. Since electrons have a low mass compared to their momenta, the pseudorapidity is about equal to the rapidity. The yield was divided by $\Delta y = \Delta \eta = 1.6$.

To obtain a production cross section the spectrum has to be multiplied with the minimum bias cross section of pp collisions at $\sigma_{\text{MB}} = 50.9 \pm 1.1$ mb. More details about the measurement of the minimum bias cross section σ_{MB} can be found in [44].

The final invariant production cross section of electrons ($\frac{e^- + e^+}{2}$) is given by dividing the raw yield N^e_{raw}, after subtracting the hadron contamination and the background from photonic electrons, by the number of analysed events (N_{MB}), by the value of the transverse momentum at the centre of each bin (p_T^{centre}) and its width Δp_T, by the width Δy of the covered rapidity interval, by the geometrical acceptance (ε^{geo}) times the reconstruction ($\varepsilon^{\text{reco}}$), PID efficiencies ($\varepsilon^{\text{eID}}$) and a factor of two to obtain the charge averaged invariant differential yield, since in this analysis the distinction between positive and negative charges is not done:

$$\frac{1}{2\pi p_T}\frac{d\sigma^e}{dp_T dy} = \frac{1}{2}\frac{1}{2\pi p_T^{\text{centre}}}\frac{1}{\Delta y \Delta p_T}\frac{N^e_{\text{raw}}}{\varepsilon^{\text{geo}} \times \varepsilon^{\text{reco}} \times \varepsilon^{\text{eID}}}\frac{\sigma_{\text{MB}}}{N_{\text{MB}}}$$

From this final production cross section the background sources coming from J/ψ and K_{e3} need to be subtracted to obtain the final invariant production cross section of electrons and positrons coming from semi-leptonic decays of heavy-flavour hadrons.
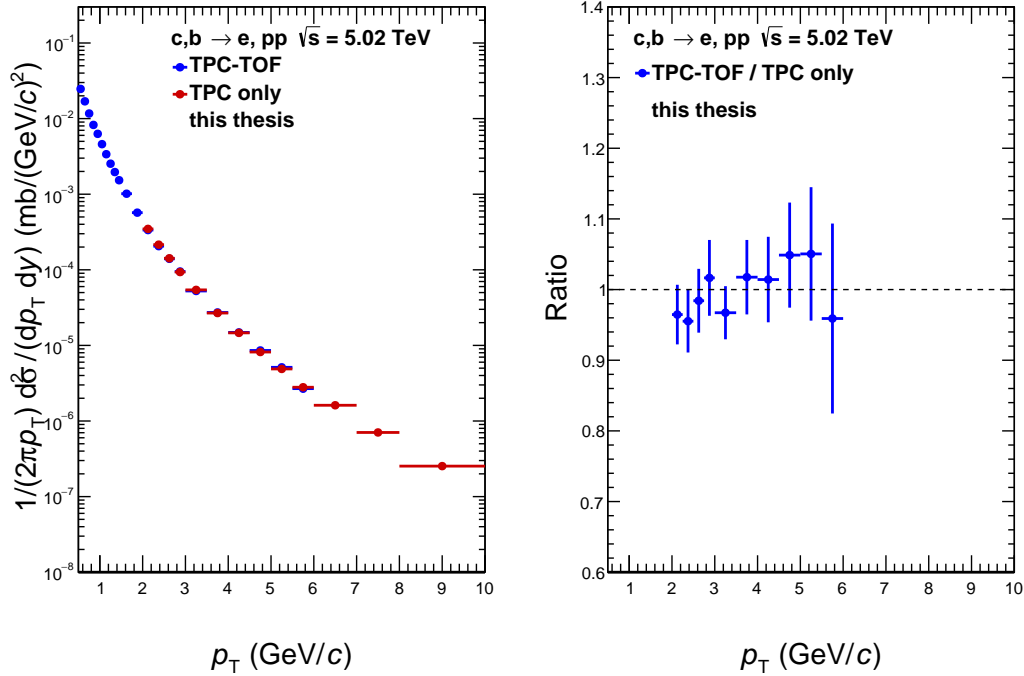
Figure 4.16: The p_T-differential cross-section for electrons from heavy-flavour hadron decays for the TPC-TOF and TPC only analyses. In addition the ratio between the two cross sections in the overlapping p_T region is shown.

Figure 4.16 shows the final cross section as function of the transverse momentum for the TPC-TOF and TPC only analyses before evaluating the systematic uncertainties. The analysis coming from "TPC-TOF" and "TPC only" agree within statistical uncertainties.

4.9 Systematic uncertainties

Several sources of systematic uncertainties affecting the measurement are considered and are described in the following sections:

- Track selection criteria on the electron candidates
- TPC PID selection
- Pseudorapidty - window
- Selection criteria in the SPD
- TPC - TOF matching
- TPC - ITS matching

(a)   (b)
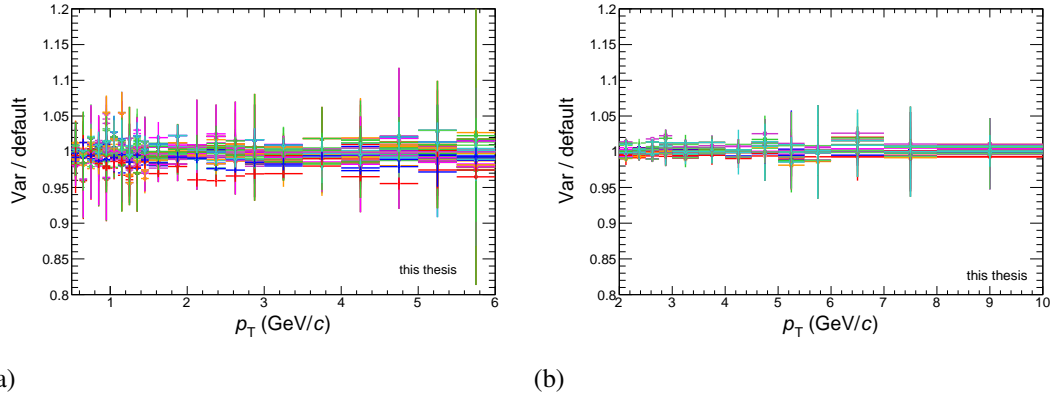
Figure 4.17: Ratio of the cross section obtained with the default selection criteria and with the varied selections of the track selection for the electron candidates listed in Table 4. The left panel shows the TPC-TOF analysis, where as the TPC only analysis is shown in the right panel. In the appendix A.2 to A.6 the variations are shown in a clearer way in different plots.

- Associated track selection and the invariant mass cut
- Weights used to correct the p_T shape of the spectra of light mesons
- Hadron contamination parametrization
- Subtracting of J/ψ and K_{e3}

The systematic uncertainties arise from the residual discrepancy between MC, used to determine the efficiency corrections, and data, and are estimated by varying the track selection and PID requirements around the default values chosen in the analysis. The different contributions were evaluated, by looking at the ratio of fully corrected cross-sections. In the end, the systematic uncertainties from different contributions are summed in quadrature, since they are considered uncorrelated.

4.9.1 Systematic uncertainties due to the selection of electron candidates

For the estimation of the systematic uncertainties due to the selection of the electron candidates the track selection criteria listed in table 4. The variations taken into account are shown in Figure 4.17 for the TPC-TOF [panel (a)] and TPC only [panel (b)] analyses.

(a)   (b)
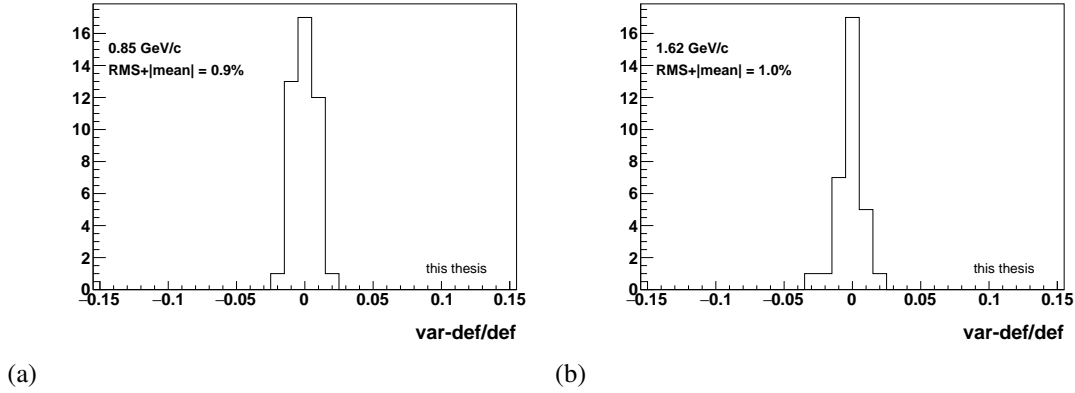
Figure 4.18: Examples of difference distributions between the cross section obtained with the default selection and with the varied selection for two p_T bins for the TPC-TOF analysis.

The variations are tested via the Barlow criterion [45], were possible statistical fluctuation of the cross section are taken into account. In this analysis all variations with $\frac{|\sigma_{\text{def.}}^2 - \sigma_{\text{var}}^2|}{\sqrt{\sigma_{\text{def.}}^2 + \sigma_{\text{var}}^2}} > 2$ are considered to be significant for the determination of the systematic uncertainty and are investigated further to check if a trend is observed in the ratios of the cross section from the default and the varied selections.

Since for the TPC-TOF case, no systematic trend was observed, an RMS approach was used to estimate the systematic uncertainty. This approach was used to avoid an overestimation of the systematic uncertainties on the final cross section, which would be obtained if all track selection criteria, e.g. TPC cluster, TPC PID cluster, would be evaluated independently. For each p_T interval of the final cross-section, the difference between the cross section obtained with the default selection criterion and with the varied one listed in table 4 is calculated. This difference is divided by the cross section obtained with the default selection to obtain a relative difference. This procedure is repeated for all considered variation. Figure 4.18 shows examples of such a distribution for two different p_T intervals. These distributions are attached to the appendix for every p_T interval evaluated in the TPC-TOF analysis (Fig. A.7 - A.9). From these plots, the RMS and the mean are extracted to estimate the systematic uncertainty associated to each p_T interval. The systematic uncertainty assigned to the track selection of the electron candidates, do not cause a significant systematic effect and varies around 1 - 2% in the whole momentum region.

Table 4: Summary of cut variations to estimate the systematic uncertainties linked to the track selection and particle identification for electron candidate tracks.

Source of Uncertainty	Reference	Variations
TPC clusters	$\geqslant 100$	$\geqslant 90, \geqslant 95, \geqslant 105,$ $\geqslant 110$
TPC PID clusters	$\geqslant 80$	$\geqslant 70, \geqslant 75, \geqslant 85, \geqslant 90$
ITS hits	$\geqslant 3$	$\geqslant 2, \geqslant 4$
TOF PID	$\pm 3.0\,\sigma$	$\pm 2.0\,\sigma, \pm 2.5\,\sigma, \pm 3.5\,\sigma, \pm 4.0\,\sigma, \pm 5.0$
DCA$_{xy}$ [cm]	< 1	$< 2, < 4$
DCA$_r$ [cm]	< 2	< 1
Kink mothers	Excluded	Included

In the TPC only analysis, we observed a systematic trend in varying the number of TPC PID clusters, whereas all other variations are not significant and are not considered further. Figure 4.19 shows the ratios between the cross section obtained with the default selection criteria and with the varied selections of the TPC PID clusters. A systematic uncertainty of 1% is assigned to the whole transverse momentum range between 2 and 10 GeV/c, which is found to be similar to the TPC-TOF analysis.

4.9.2 Systematic uncertainties due to the photonic electron subtraction

For the estimation of the systematic uncertainties due to the photonic background subtraction, the associated track selection criteria were varied. The variations taken into account are summarized in Table 5 and the ratio of the cross sections obtained with the default and varied selection criteria are shown in Figure 4.20 for the TPC-TOF [panel (a)] and TPC only [panel (b)] respectively.
Similarly to the estimation of the systematic uncertainty due to the selection of electron candidates, the Barlow criteria was used to take into account possible statistical fluctuations.

For the TPC-TOF case no systematic trend was observed and therefore again an RMS approach was used to calculate the systematic uncertainty due to the photonic electron subtraction. The difference distribution of the cross section obtained with the default selection criteria and the varied selection criteria for each p_T interval are shown in the Appendix in Figure A.22 - A.24. A maximum systematic

(a)   (b)
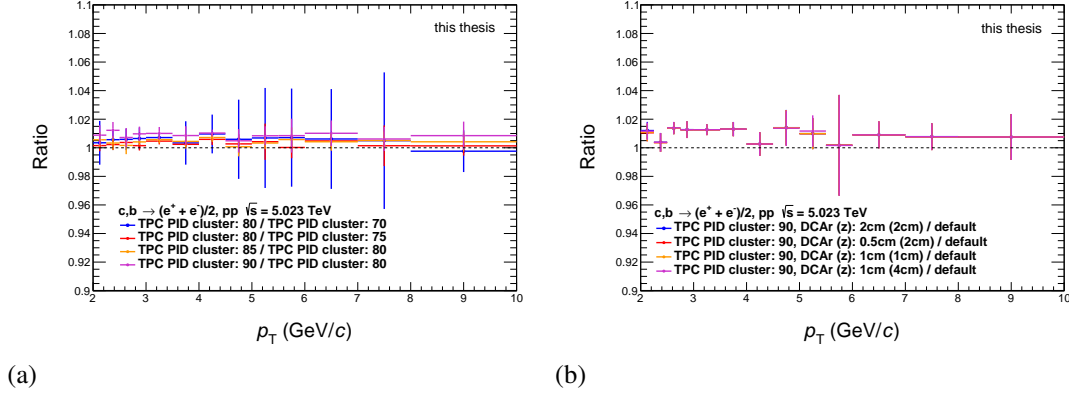
Figure 4.19: Ratio of the cross section obtained with the default selection criteria and with the varied selection criteria on the TPC PID clusters [panel (a)] and simultaneous variation of both the TPC and TPC PID number of clusters.

Table 5: Summary of variations to estimate the systematic uncertainties linked to the track selection and particle identification for associated candidate tracks.

Source of Uncertainty	Reference	Variations
p_T^{Min} (GeV/c)	> 0.1	$> 0.0, > 0.15$
Mass cut (GeV/c^2)	< 0.14	$< 0.10, < 0.12, < 0.16, < 0.18, < 0.2$
TPC clusters	$\geqslant 60$	$\geqslant 50, \geqslant 70, \geqslant 80$
TPC PID clusters	$\geqslant 60$	$\geqslant 50, \geqslant 70, \geqslant 80$
DCA$_{xy}$ [cm]	< 1	$< 0.5, < 2$
DCA$_r$ [cm]	< 2	$< 0.5, < 1, < 4$
ITS hits	≥ 2	$\geq 1, \geq 3$

(a)   (b)
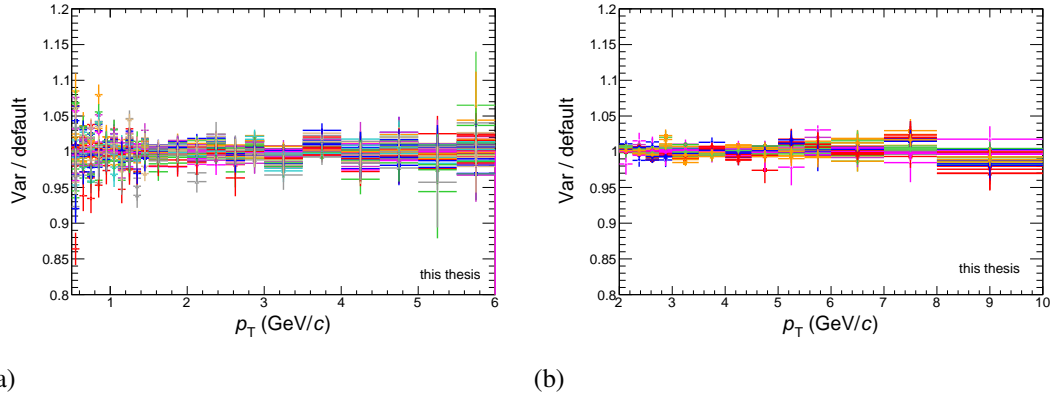
Figure 4.20: Ratio of the cross section obtained with the default selection criteria and with the varied selection criteria for all variations concerning the associated track selection criteria for the TPC-TOF and TPC only analysis. In the appendix A.12 to A.21, the variations are shown in a clearer way in many plots.

uncertainty of 4% at low transverse momentum, decreasing up to 2% at the highest transverse momentum, 6 GeV/c is assigned for the TPC-TOF analysis. As expected, the systematic effect due to the variation of the track selection criteria on the associated tracks is especially important at the low p_T interval, since in this p_T interval most of the electrons are coming from photonic sources, and the final cross-section is therefore sensitive to variation which is changing the number of photonic electrons.

For the TPC only analysis strategy, a trend in the variation of the invariant mass selection cut and the minimum p_T of electrons is observedwhereas all other variations are not significant and are neglected. A systematic uncertainty of 1 % between 2 and 5 GeV/c is assigned, which is similar like for the TPC-TOF analysis.

4.9.3   Systematic uncertainties from other sources

In contrast to the estimation of the systematic uncertainties due to the selection of electron candidates and due to the photonic electrons, described in the last sections, the systematic uncertainties from sources described in this section were considered separately. This is due to the fact that the variations considered in this section are not only testing the quality of the tracks but also other parts of the analysis, e.g. background subtraction and detector and track properties, which will be pointed out in more details when the systematic source is discussed. The

(a)   (b)
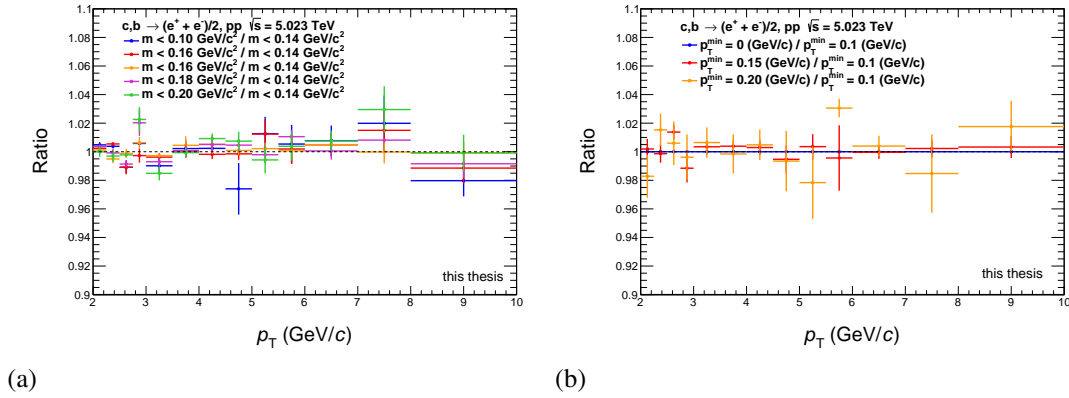
Figure 4.21: Ratio of the cross section obtained with the default selection criteria and with the varied selection criteria of the invariant mass cut [panel (a)] and the minimum p_T of electrons [panel (b)].

systematic sources described in this section are:

- TPC PID selection
- Pseudorapidty - window
- Selection criteria in the SPD
- TPC - TOF matching
- TPC - ITS matching
- Weights used to correct the p_T shape of the spectra of light mesons
- Hadron contamination parametrization
- Subtracting of J/ψ and K_{e3}

For these sources, a systematic uncertainty is assigned where a systematic trend in the ratio of the cross section obtained with the default selection criterion and varying the other aspects of the analysis strategy is observed. Since an RMS approach is not possible with the limited number of variations which are possible, the maximum variation in those cases is used as an estimate of the systematic.

- The variation on the TPC PID selection was considered separately from the track selection criteria on the electron candidates because we observed a shift of the electron candidates in this data sample and a systematic effect was observed when varying the TPC PID selection. On the other hand, the variation on the TPC PID serves as a test of the TPC PID efficiency correction and the description of the electron spline. Figure 4.22 shows the ratio of the cross section obtained with the default TPC PID selection and with

(a)   (b)
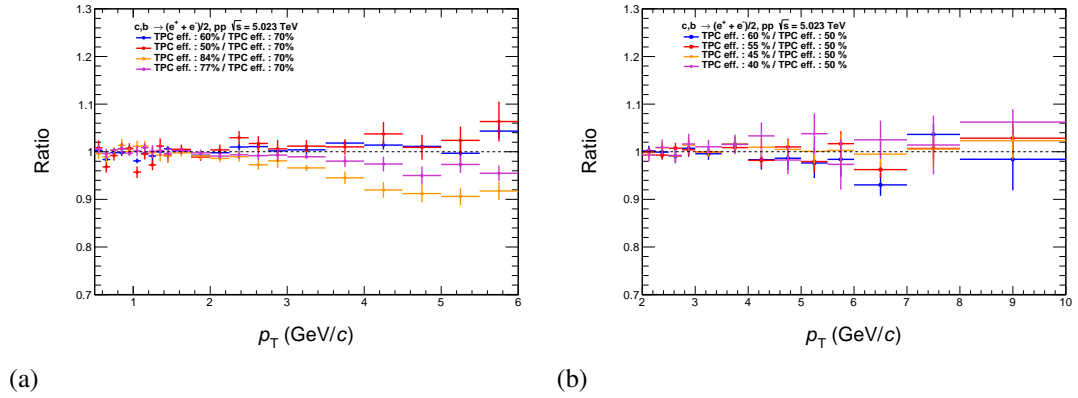
Figure 4.22: Ratio of the cross section obtained with the default TPC PID selection and the varied one for the TPC-TOF [panel (a)] and TPC only analysis [panel (b)].

the varied selection for the TPC-TOF [panel (a)] and TPC only [panel (b)] analyses.

For the TPC-TOF analysis a systematic uncertainty of 2% between 2-3 GeV/c, 3 % between 3-4 GeV/c and 5% between 4-6 GeV/c, whereas for the TPC only analysis a systematic uncertainty of 2% between 4-6 GeV/c, 3% between 6-8 GeV/c and 5% between 8-10 GeV/c was assigned. This trend in the systematic uncertainties could be partly due to the fact, that at larger p_T the relative number of hadrons compared to electrons is increasing and the variation on the TPC PID is varying this relative number.

- The analysis was performed in the pseudorapidity window $|\eta| < 0.8$. To test the detector performance on the edges (i.e. distortions) of the detector and our description of the detector material at the edges, the pseudorapidity window is varied to $|\eta| < 0.5, |\eta| < 0.6$ and $|\eta| < 0.7$. For each of the η, the hadron contamination had to be recalculated since the relative hadron contamination is changing as function of η. Fig. 4.23 shows the $n\sigma^e_{\mathrm{TPC}}$ distribution as function of η. One can clearly recognize that the pion band is moving away from the electron band leading to a lower hadron contamination at large $|\eta|$. This can be explained by the fact, that the dE/dx resolution for tracks with a larger length in the TPC is better compared to shorter tracks.

The TPC signal for a track is collected in clusters and each part of a track
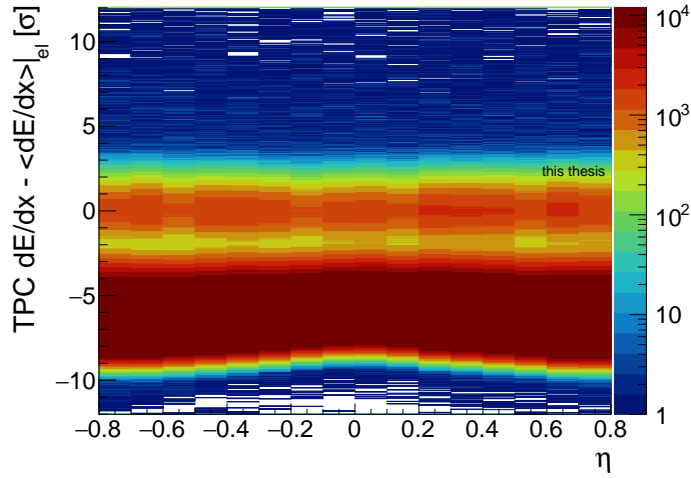
Figure 4.23: $n\sigma^e_{TPC}$ distribution as function of the the pseudorapidity $|\eta|$. Electrons are found at 0 $n\sigma^e_{TPC}$, while pions are found between $-3n\sigma^e_{TPC}$ and $-10n\sigma^e_{TPC}$.

belongs to a certain cluster. The track length associated with one cluster is larger for larger η, since the track traverses the TPC diagonally. The ionization of the gas due to the track is fluctuating and the total deposit on one cluster is following a Landau distribution. If the associated track length for one cluster gets larger, the relative fluctuations get smaller, leading to a better dE/dx resolution (width of the TPC signal is smaller). When the electrons and pions are distributed around their expectation value, at larger η they are separated by the same distance, but their distribution widths are smaller. The pion tail is not reaching the electron signal so easily, leading to a lower relative hadron contamination.

Fig. 4.24 shows the ratio of the cross section obtained with the default η selection and the with the varied η selection for the TPC-TOF and TPC only analysis. In the TPC-TOF analysis strategy, a systematic uncertainty of 5% between 0.5 and 1 GeV/c was assigned, whereas in the TPC only strategy a systematic of 4% was assigned between 5 and 10 GeV/c.

- To test the robustness of the photonic-electron tagging method, the number of clusters in the SPD required for electron candidates has been released to a single hit in any of the two layers or the first layer, increasing in this way

(a)   (b)
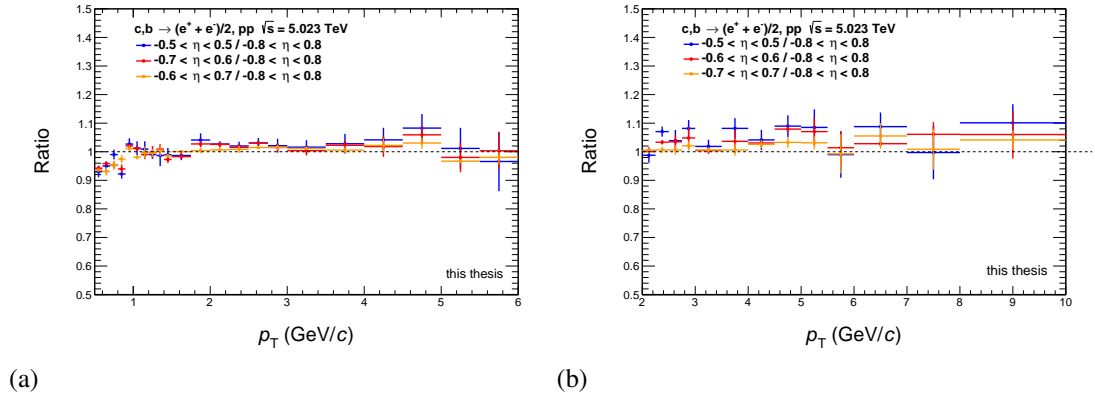
Figure 4.24: Ratio of the cross section obtained with the default η selection and with the varied selection for the TPC-TOF [panel (a)] and TPC only [panel (b)] analysis.

the fraction of electrons coming from photon conversions in the detector material. Figure 4.25 shows the ratio of the cross section obtained with the default SPD selection and the varied one for the TPC-TOF and TPC only analysis. Due to the SPD variation a systematic uncertainty of 3% between 0.5 and 2 GeV/c and the whole momentum interval was assigned for the TPC-TOF and TPC only analysis, respectively.

- As described in section 4.6, the tagging efficiency depend on the p_T-shape of the π_0 and η spectra, which need to be reweighed since they disagree in data and Monte Carlo. To estimate a systematic uncertainty due to this reweighing, the used reweighing function is varied, by considering the upper and lower extrema of the uncertainties of the measured spectra. Figure 4.26 shows the ratio of the cross section obtained with the default reweighting function and with the varied one. For both analyses, no systematic uncertainty was assigned.

- The systematic uncertainty due to the hadron contamination is estimated using a different parametrization (shown in Fig. 4.5). Figure 4.27 shows the ratio of the cross section obtained with the default parametrization and the varied one for the TPC-TOF and TPC only analysis.
  For the TPC-TOF analysis, the error function was used to describe the

(a)   (b)
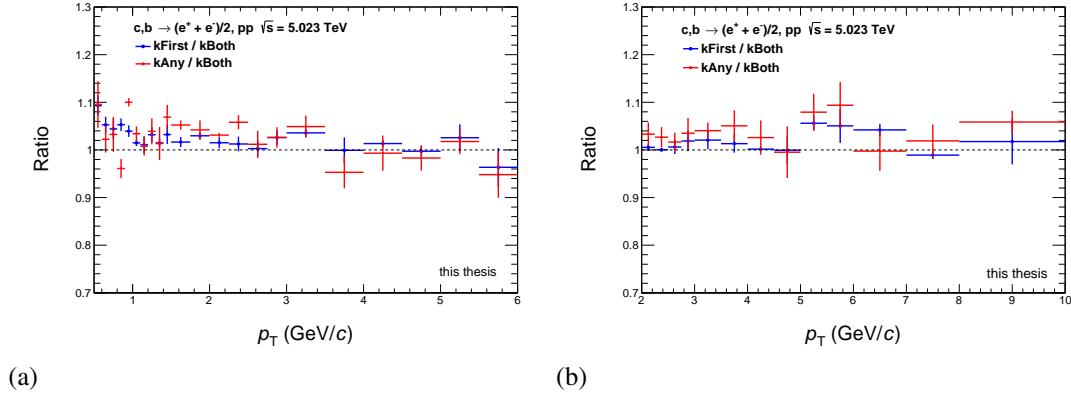
Figure 4.25: Ratio of the cross section obtained with the default SPD selection and with the varied selection on the requirement concerning hints in the SPD for the TPC-TOF [panel (a)] and TPC only [panel (b)] analysis.

(a)   (b)
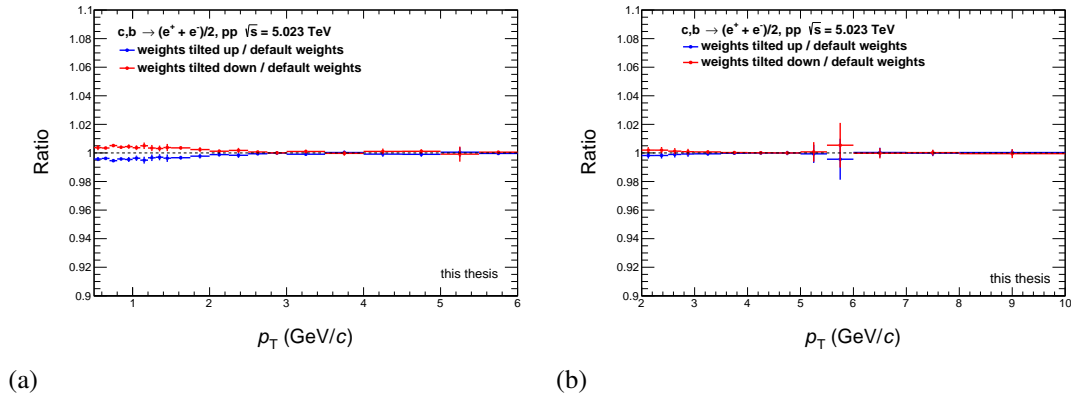
Figure 4.26: Ratio of the cross section obtained with the default reweighting function and with the varied ones for the TPC-TOF [panel (a)] and TPC only [panel (b)] analysis.

(a)   (b)
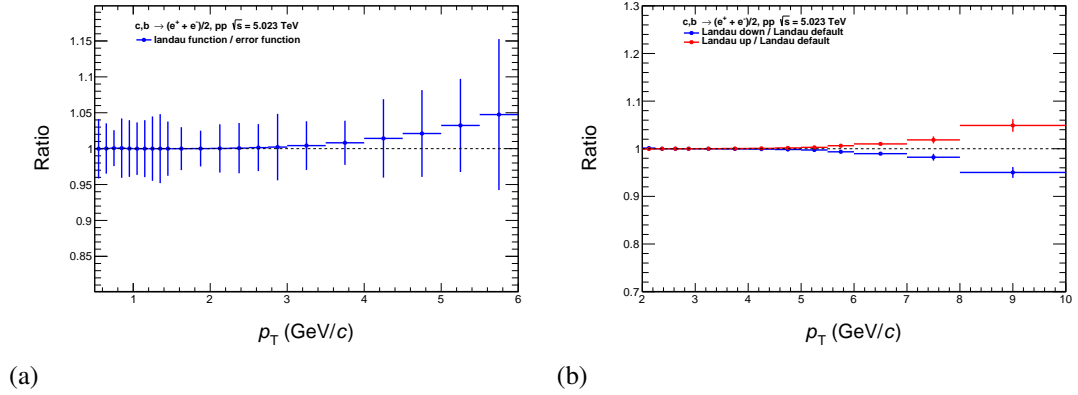
Figure 4.27: Ratio of the cross section obtained with the default hadron contamination parametrization and with the varied one for the TPC-TOF [panel (a)] and TPC only [panel (b)] analysis.

hadron contamination of a Landau. In this case, a systematic uncertainty of 4% was assigned in the transverse momentum region between 5 and 6 GeV/c.

For the TPC only analysis, a different procedure was used, since the error function showed no difference to the Landau function. Here the systematic uncertainty was calculated by using the upper and lower statistical uncertainties of the hadron contamination to estimate a parametrization. In the TPC only analysis, a systematic uncertainty of 1 % between 6-7 GeV/c, 2 % between 7-8 GeV/c and 5 % between 8-10 GeV/c was assigned.

The final spectrum is most sensitive to the variation of the hadron contamination at larger momentum since the relative amount of hadron (especially pions) is increasing monotonically as function of momentum. For the TPC-TOF analysis this effect begins to be important at a lower momentum interval then the TPC only analysis, since a looser TPC PID selection is used in the TPC-TOF analysis.

- The subtraction of the background electrons contribution from the J/ψ and K_{e3} decays are affected by the uncertainty on the input distribution. This results in an uncertainty of 100% on the J/ψ and K_{e3} spectra, like in similar analysis [40]. Figure 4.28 shows the ratio of the cross section obtained with the default selection and the varied one, not removing the background source, for the TPC-TOF and TPC only case. For the subtraction of the K_{e3} component a systematic uncertainty of 4 % between 0.5 and 0.6 GeV/c,

(a)   (b)
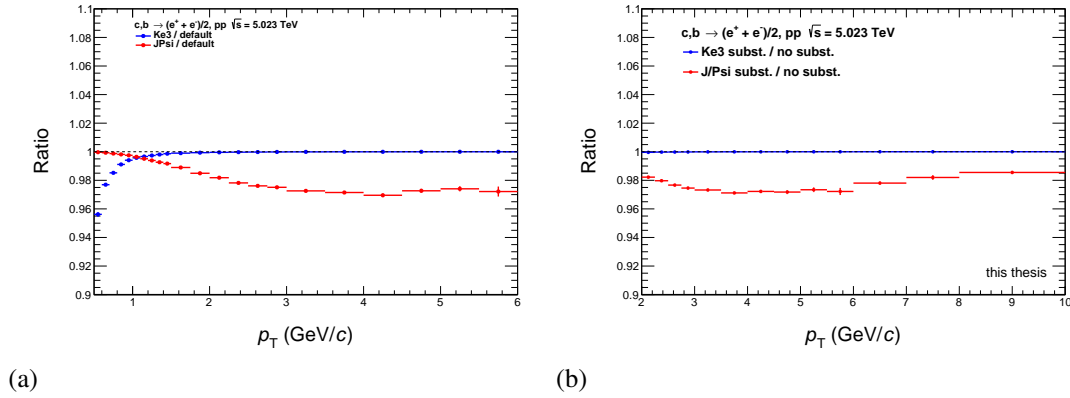
Figure 4.28: Ratio of the cross section obtained with the default selection criteria and the varied one concerning the subtraction of the J/ψ and K_{e3} component for the TPC-TOF [panel (a)] and TPC only [panel (b)] analysis.

2% between 0.6 and 0.7 GeV/c and 1% between 0.7 and 0.9 GeV/c was assigned in the TPC-TOF analysis, whereas no systematic was assigned for the TPC only analysis strategy, since it starts at 2 GeV/c.
For the subtraction of the J/ψ component a systematic uncertainty of 1% between 1.5 and 3 GeV/c and 3% between 3 and 6 GeV/c was assigned for the TPC-TOF analysis, whereas 2 % between 2 - 3 and 6 -8 GeV/c and 3% between 3 - 6 GeV/c was assigned in the case of the TPC only analysis.

- The systematic uncertainty due to the TPC-ITS matching was taken from [46].
  The uncertainty for the TPC-TOF matching was estimated by using charged particle tracks since they offer a larger statistical sample. First of all, the ratio between charged particle tracks with and without the TOF detector, in data and MC is calculated. Both ratios are compared with each other, as shown in Figure 4.29 as function of transverse momentum, and is used to assign a systematic uncertainty. This amounts to 2% for both analysis strategies, both for the TPC-ITS and for the TPC-TOF matching.

4.9.4   Total systematic uncertainty

The total systematic uncertainty was calculated by summing the contributions from all the sources described in the last three sections in quadrature since they
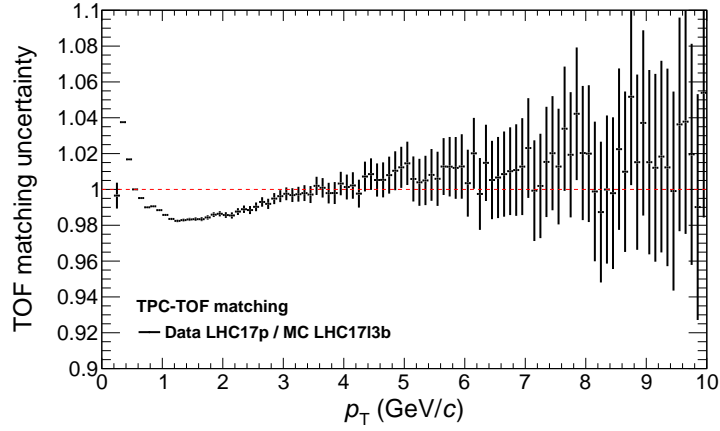
Figure 4.29: Ratio of the efficiency to find a track before and after TOF between Data and Monte Carlo. The ratio is used to estimate the systematic uncertainty due to the TPC-TOF matching.

are considered to be uncorrelated. The total systematic uncertainties are summarized in Table 6 and shown in Figure 4.30 for the TPC-TOF [panel (a)] and TPC only [panel (b)] analyses. At low transverse momentum, the largest contribution to the systematic uncertainty is coming from the variation of the η- window and from the uncertainties in the determination of the photonic background. At large transverse momentum, the most significant systematic uncertainty is coming from the subtraction of the hadron contamination.

Table 6: Summary of the total systematic uncertainties

Transverse momentum (p_T) in GeV/c	Total systematic uncertainty (%)	
	TPC-TOF	TPC-only
0.5-0.6	8.8	-
0.6-0.7	7.3	-
0.7-0.8	7.2	-
0.8-0.9	7.4	-
0.9-1.0	6.9	-
1.0-1.1	5.1	-
1.1-1.2	5.2	-
1.2-1.3	5.4	-
1.3-1.4	5.1	-
1.4-1.5	4.8	-
1.5-1.75	4.8	-
1.75-2.0	4.6	-
2.0-2.25	4.0	4.7
2.25-2.5	4.3	4.8
2.5-2.75	4.1	4.8
2.75-3.0	4.1	4.8
3.0-3.5	5.6	5.3
3.5-4.0	5.5	5.3
4.0-4.5	6.9	5.5
4.5-5.0	6.9	5.5
5.0-5.5	8.0	7.2
5.5-6	8.2	7.2
6-7	-	7.0
7-8	-	7.2
8-10	-	9

(a) (b)
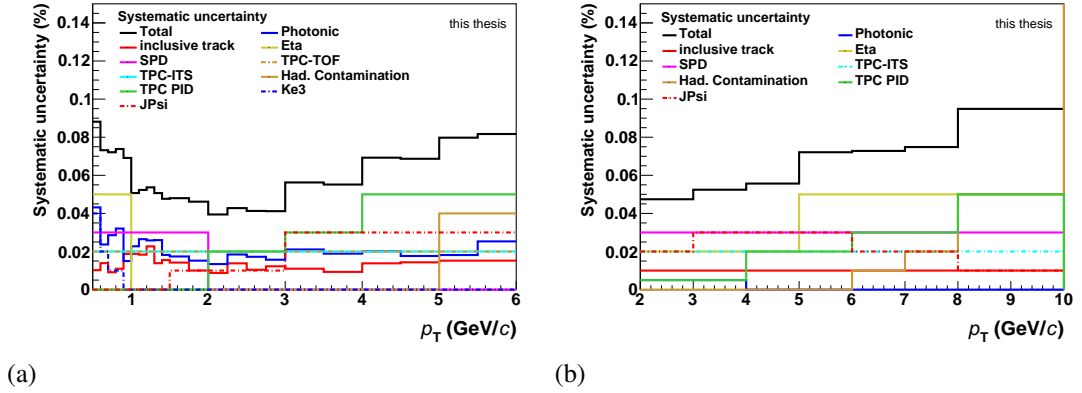
Figure 4.30: The total systematic uncertaitny together with each component for the TPC-TOF [panel (a)] and TPC only [panel (b)] analysis.

5 Results and discussion

The final invariant production cross section of electrons from decays of heavy-flavour hadrons, containing a charm or beauty quark, in proton-proton collisions at $\sqrt{s} = 5.02$ TeV as function of p_T is shown for the TPC-TOF and TPC only analyses in Fig. 5.1. In the overlapping region of both analyses between 2 and 6 GeV/c, the production cross sections agree within statistical and systematic uncertaities, as shown in the right panel.

For the final cross-section, the TPC-TOF measurement is used below 3 GeV/c and above the TPC only measurement is used because of the lower statistical and systematic uncertainties. The final p_T-differential production cross section of electrons coming from decays of heavy-flavour hadrons is shown in Figure 5.2 together with the FONLL pQCD calculation. The FONLL calculation was obtained via the published framework [47] for hadrons containing a charm or beauty quark. To compare with the final production cross section in this thesis, the FONLL calculations for charm and beauty quarks were added up. The uncertainties of the FONLL calculations are shown as a red band and reflect different choices for the charm and beauty quark masses, the factorization and renormalization scales. They also reflect the uncertainty on the set of parton distribution functions used in the FONLL calculations. The measured production cross section lies on the upper edge of the theoretical prediction.

Since similar measurements for pp collisions at $\sqrt{s} = 2.76$ TeV [48], $\sqrt{s} = 7$ TeV [40, 49] and $\sqrt{s}$ 13 TeV [50], ratios of the cross sections at different energies
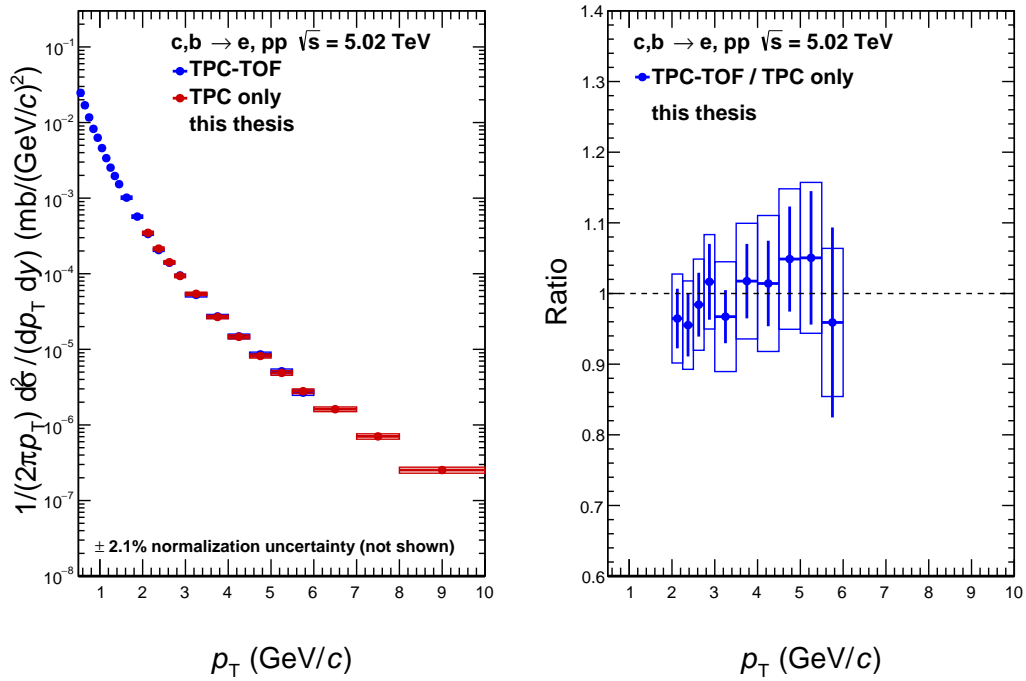
Figure 5.1: The p_T-differential cross-section for electrons from semi-leptonic heavy-flavour hadron decays for the TPC-TOF and TPC only analyses on the left side. In addition the ratio between the cross section obtained in the two analyses strategies is shown in the overlapping p_T region between 2 and 6 GeV/c.
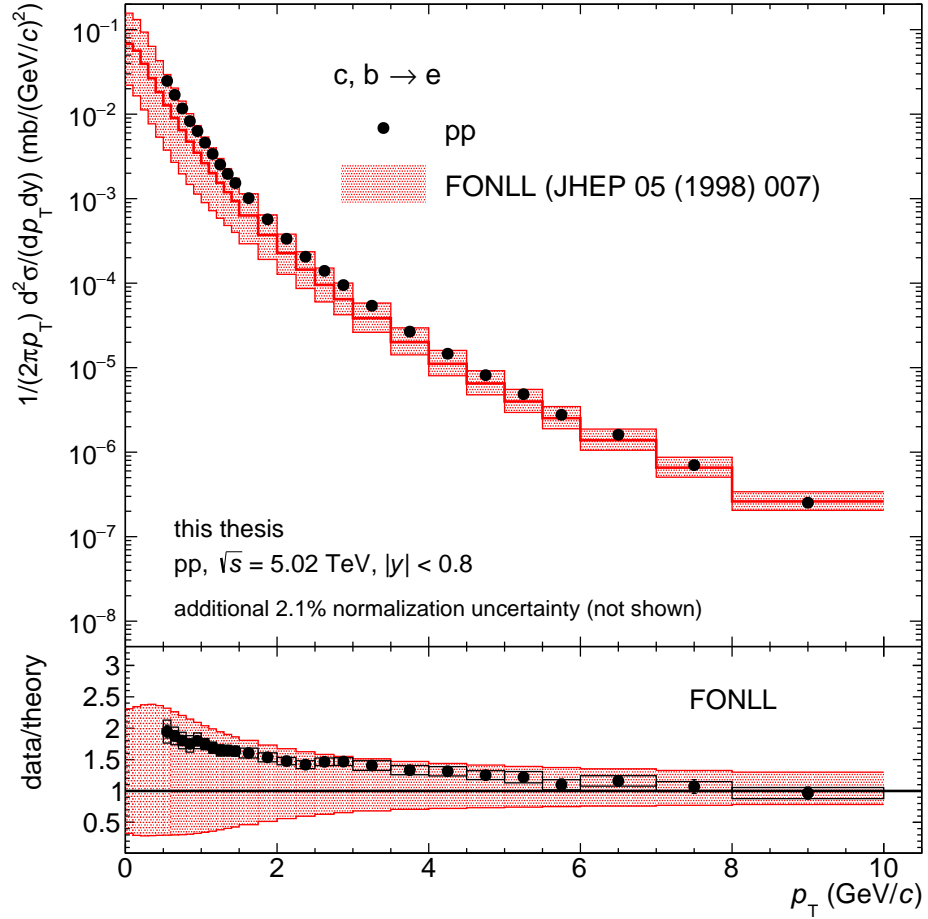
Figure 5.2: The p_T- differential cross section for electrons from semi-leptonic decays of hadrons containing a charm or beauty quark in pp at $\sqrt{s}$ = 5.02 TeV, compared to the theoretical prediction of this cross- section given by FONLL. On the lower panel, the ratio between the measured cross section and the mean value given by FONLL together with the model prediction band is shown.

can be compared with similar FONLL calculations. The statistical and systematic uncertainties of the cross-sections were added in quadrature to calculate the ratios. The ratios calculated with FONLL have smaller uncertainties, compared to the uncertainties from the production cross section calculated with FONLL. Therefore in principle, these ratios allow to constrain some of the input parameters of FONLL in a much better way, than only comparing the cross sections [51]. Figure 5.3 shows the ratio of the production cross section in pp at $\sqrt{s} = 5.02$ with the production cross section in pp at $\sqrt{s} = 2.76$, 7 and 13 TeV together with the FONLL calculations. The ratios of production cross sections are affected by large statistical and systematic uncertainties, which make it difficult for the moment to constrain any of the parameter inputs in FONLL. High statistic data (ALICE Run3) and a reduction of the systematic uncertainties especially at $p_T >$ 2 GeV/c can improve the uncertainties on the data and allow to constrain some of the FONLL input parameters.

The production cross-section of electrons from semi-leptonic decays of heavy-flavour hadrons is used as a reference for the production of electrons from semi-leptonic decays of heavy-flavour hadrons in heavy-ion collions, where the QGP is formed. The production cross-section obtained in this thesis is used together with similar measurements in Xe-Xe[52] and Pb-Pb[53] collisions to estimate the nuclear modification factor in Xe-Xe and Pb-Pb collisions.

Fig. 5.4 shows the nuclear modification factor R_{AA} in Xe-Xe collisions at $\sqrt{s}$ = 5.44 TeV for central (0-20%) and peripheral (20-40%) events for electrons (black marker) or muons (red marker) from semi-leptonic decays of heavy flavour hadrons. The measurement of electrons from semi-leptonic decays of heavy-flavour hadrons was measured at mid-rapidity (|y| < 0.8) using the ITS, TPC and TOF detector of ALICE, the measurement of muons were performed at forward-rapidity (2.5 < y < 4.0) with the muon spectrometer. Since the center of mass energy of the reference and the XeXe collisions differ, the pp reference is scaled using the ratio of the production cross section at $\sqrt{s}$ = 5.02 and 5.44 TeV calculated with FONLL. In the overlapping region between p_T = 3 - 6 GeV/c both nuclear modification factors R_{AA}'s agree well within statistics and systematic uncertainties. This is also expected by theory since the branching ratios of B or D mesons in the semi-leptonic channel is similar due to lepton universality. This comparison serves also as a cross-check of the measurement of electrons from semi-leptonic decays of heavy-flavour hadrons in Xe-Xe and p-p collisions.

(a)

(b)

(c)
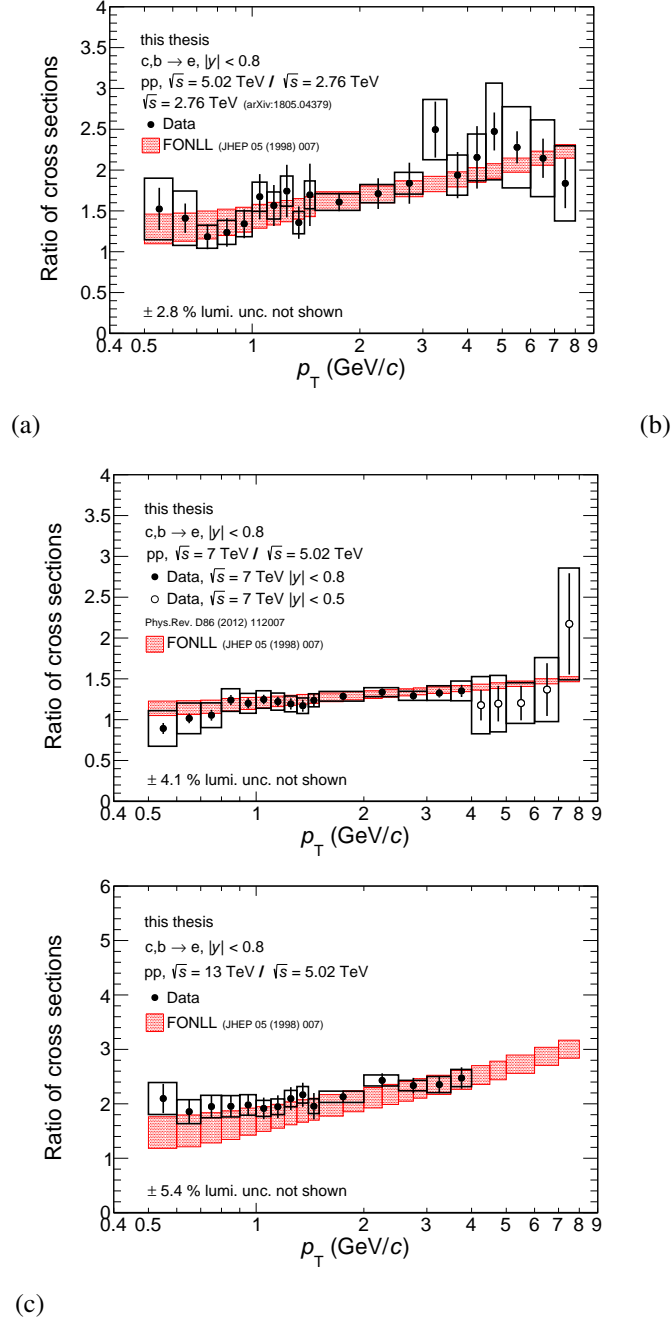
Figure 5.3: Ratio of production cross section as function of p_T in pp for different collision energies, compared to the theoretical prediction by FONLL (red band).
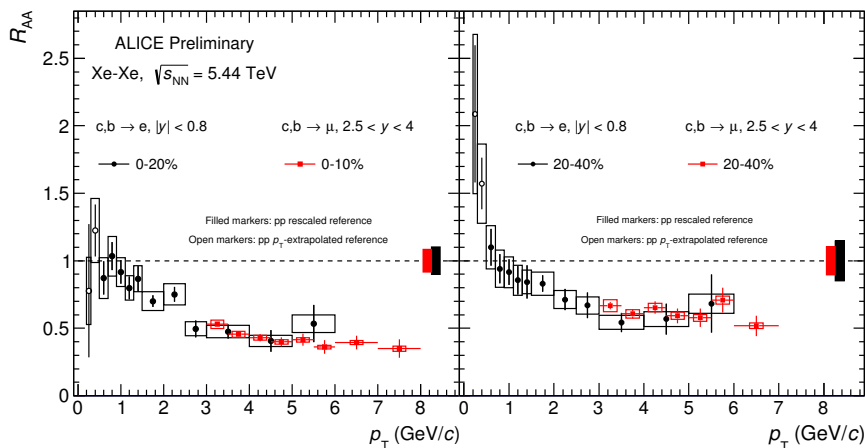
ALI-PREL-148699

Figure 5.4: Nuclear modification factor R_{AA} in Xe-Xe collisions as function of p_T obtained from the analysis of electrons and muons from semi-leptonic decays of heavy flavour hadrons.

On the other hand, Fig.5.5 shows the R_{AA} for the most central (0-10%) and semi-central (30-50%) collisions in Pb-Pb collisions at $\sqrt{s}$ = 5.02 TeV together with different theoretical predictions. The cross section measured in this analysis is used as pp reference up to a momentum of p_T = 10 GeV/c. Above p_T = 10 GeV/c, the reference was obtained by scaling the measurment at $\sqrt{s}$ = 7 TeV by the ATLAS collaboration [56] with the ratio of the cross section at the two collisions energies computed by FONLL [57].

First of all, a strong suppression is observed from what is expected from a binary scaling at large p_T, which was discussed in section 2.3. This behaviour is a signature for the medium induced energy loss on heavy quarks traversing the QGP produced in heavy-ion collisions. In addition, a centrality dependence of the nuclear modification factor is observed, which is compatible with the hypotheses of the partonic energy loss dependence on the medium density being larger in a hotter and denser QGP, which is produced in central collisions. Both observations are also seen in Xe-Xe collisions.

The theoretical models shown in Fig. 5.5 differ in their implementation of the medium properties and dynamics of the medium evolution, e.g., how heavy quarks lose their energy in the medium. They also differ in the implementation of the hadronisation process, the nuclear modification of the parton distribution functions and the input of the heavy-flavour cross-section. Most of the models show good agreement with the data in both centrality classes. The predictions of
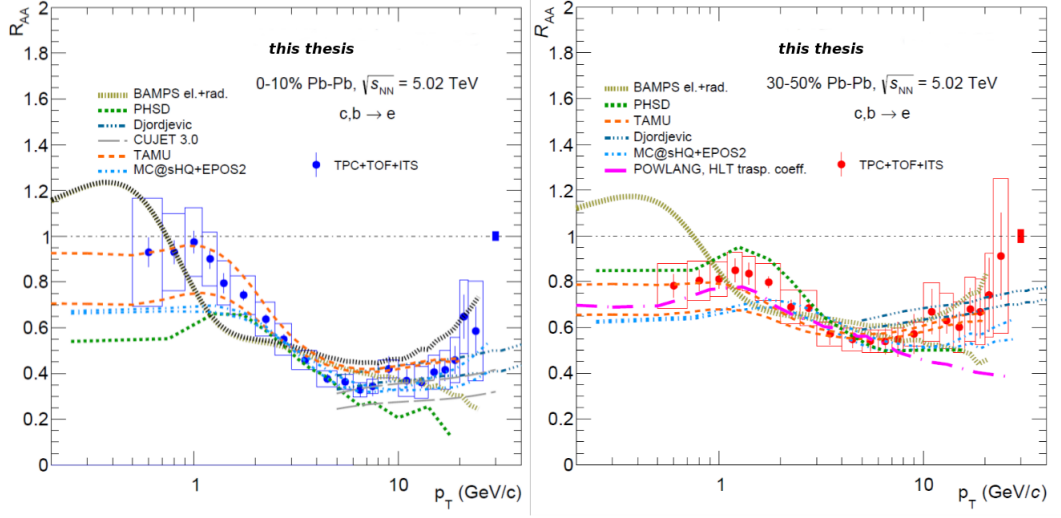
(a)

Figure 5.5: Nuclear modification factor of electrons from semi-leptonic decays of heavy-flavour hadrons for Pb-Pb collisions as function of the transverse momentum together with several theoretical models [54]-[55]. In the left panel most central collisions are shown, whereas the right panel shows semi-central collisions.

MC@sHQ+EPOS2 [54], PHSD [58] and TAMU [59] models also include the modification of the parton distribution functions, which is needed to describe the suppression of the R_{AA} at low p_T.

The nuclear modification factor in central Pb-Pb collisions is well described by TAMU [59] at $p_T < 3$ GeV/c within the uncertainties. At larger p_T the model tends to overestimate the R_{AA}, which can be explained by the missing implementation of the radiative energy loss in the model, which becomes dominant at large p_T.

The CUJET3.0 [60] and Djordjevic [61, 62] models show a good description of the R_{AA} in both centralities, indicating that the dependencies of the radiative energy loss on the path length in the QGP are well understood.

6   Conclusion

The production cross-section of electrons form semi-leptonic decays of heavy-flavour hadrons was measured in the transverse momentum interval between 0.5 GeV/c and 10 GeV/c at mid-rapidity in proton-proton collisions at the center of mass energy of $\sqrt{s} = 5.02$ TeV via the photonic tagging method, to estimate the dominate background sources.

The production cross-section was compared to perturbative QCD calculation FONLL and shows good agreement within uncertainties. The measurement shows a better precision than the pQCD calculation itself, and also lies at the upper edge of the theoretical prediction. Therefore a more precise pQCD calculation is needed to improve our understanding of the underlying phenomena. This could be achieved in adding NNLO and NNNLO resummation terms to the pQCD calculation, since FONLL includes only terms up to NLO. On the other hand, data can be used to restrict some of the input parameters of FONLL, which could be achieved by comparing the ratio of the production cross-section from semi-leptonic decays of heavy-flavour hadrons at different collision energies in proton-proton collisions. Since the statistical and systematic uncertainties of these ratios are to large to draw any conclusions they need to be improved. The statistical uncertainties can be reduced with high statistical data in the future Run 3 and 4 of the ALICE experiment, whereas the systematic uncertainties can be reduced by e.g. a new analysis strategy.

On the other hand, the production cross-section of electron from semi-leptonic decays of heavy-flavour hadrons was used as a reference for the same measurement in heavy-ion collisions to investigate the medium induced energy loss for heavy-flavour particles. The nuclear modification factor shows a strong suppression both in Pb-Pb and Xe-Xe collisions, which is expected from the violation of binary scaling, due to nuclear matter effects. In addition, the nuclear modification factor was compared to model calculations with different implementation of the medium properties and the dynamics of the medium, showing the importance of both radiative and collisional energy loss mechanism, to explain the observed behaviour of the nuclear modification factor.

A   Appendix

A.1   Electrons from background sources
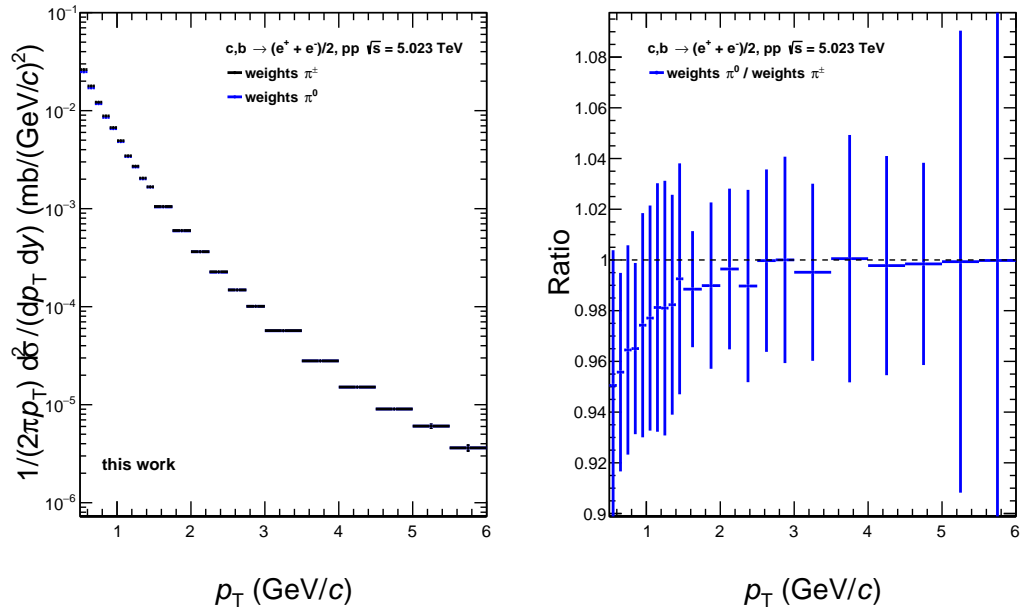
Figure A.1: Final production cross section of electrons from semi-leptonic decays of heavy flavour hadrons using for the weight calculation charged and neutral pion spectrum together with the ratio for the TPC-TOF analysis.

A.2   Systematic uncertainties due to the selection of electron candidates

A.2.1   TPC-TOF analysis
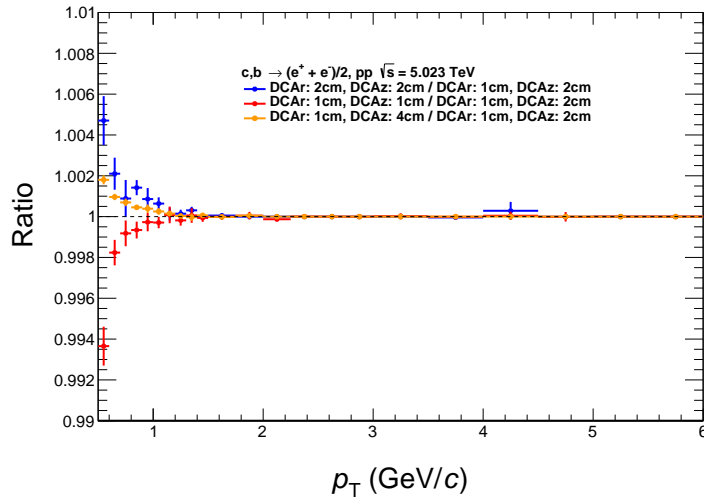
Figure A.2: Ratio of the cross section obtained with the default selection criterion and with the varied selection criteria, varying the DCA_{xy} and DCA_z for the selection of electron candidates.
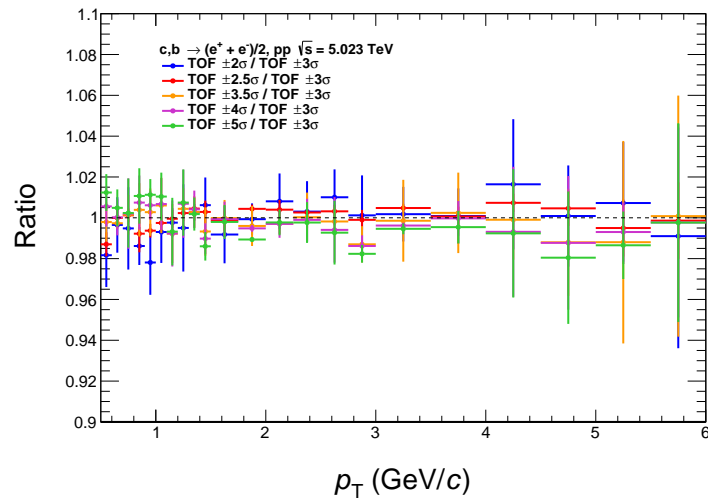
Figure A.3: Ratio of the cross section obtained with the default selection criterion and with the varied selection criteria, varying the TOF PID selection for electron candidates.
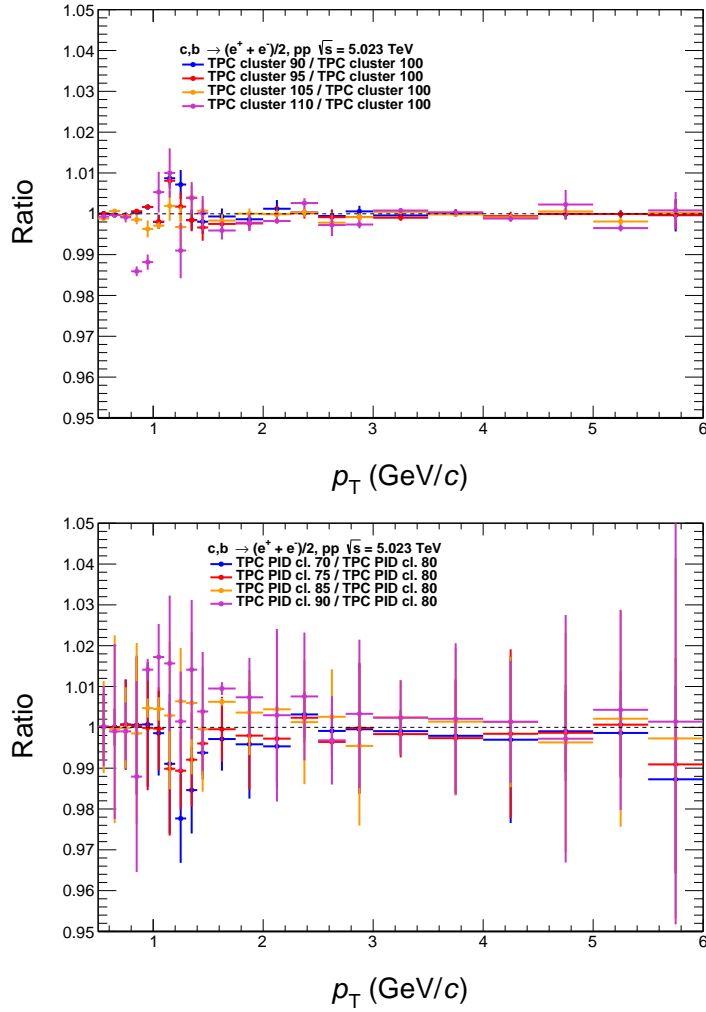
Figure A.4: Ratio of the cross section obtained with the default selection criterion and with the varied selection criteria, varying the number of TPC cluster and TPC cluster used for PID for the selection of electron candidates.
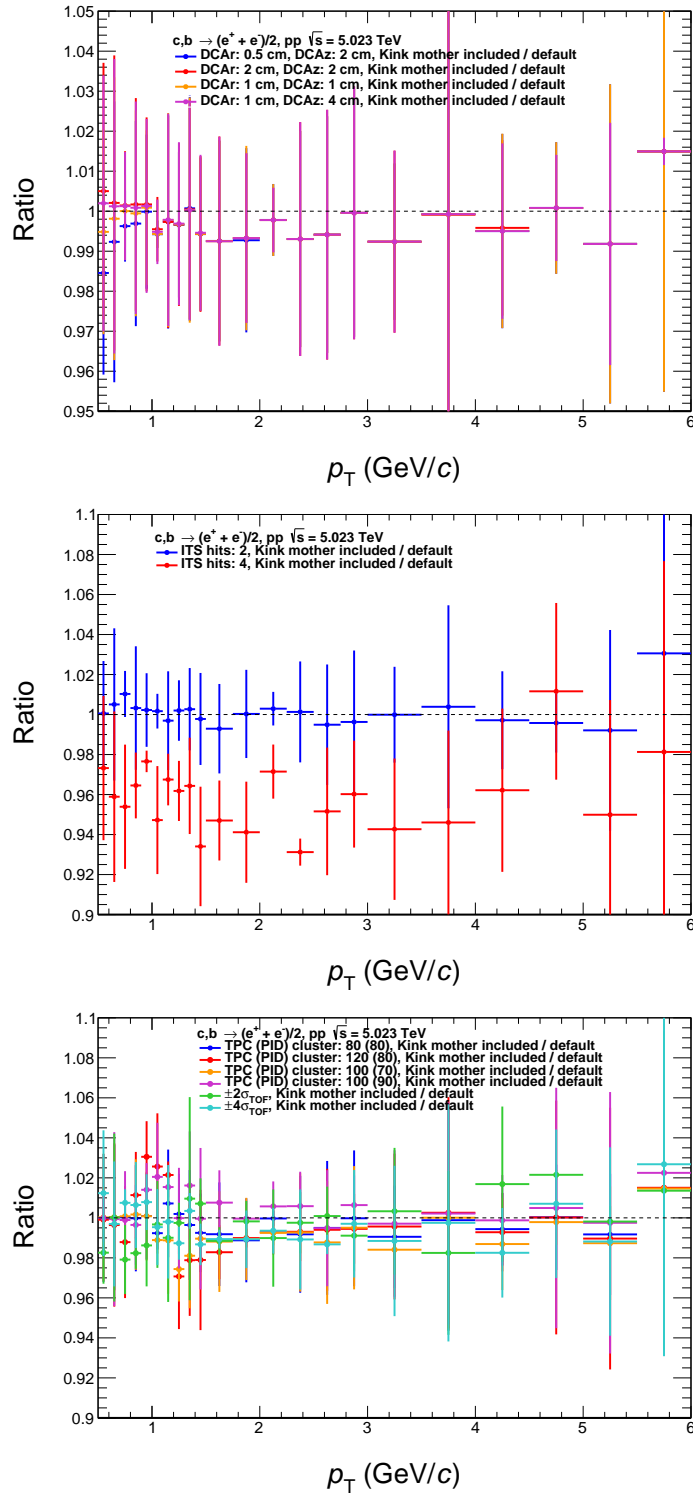
Figure A.5: Ratio of the cross section obtained with the default selection criterion and the varied selection criteria, varying different combination of criteria for the selection of electron candidates.
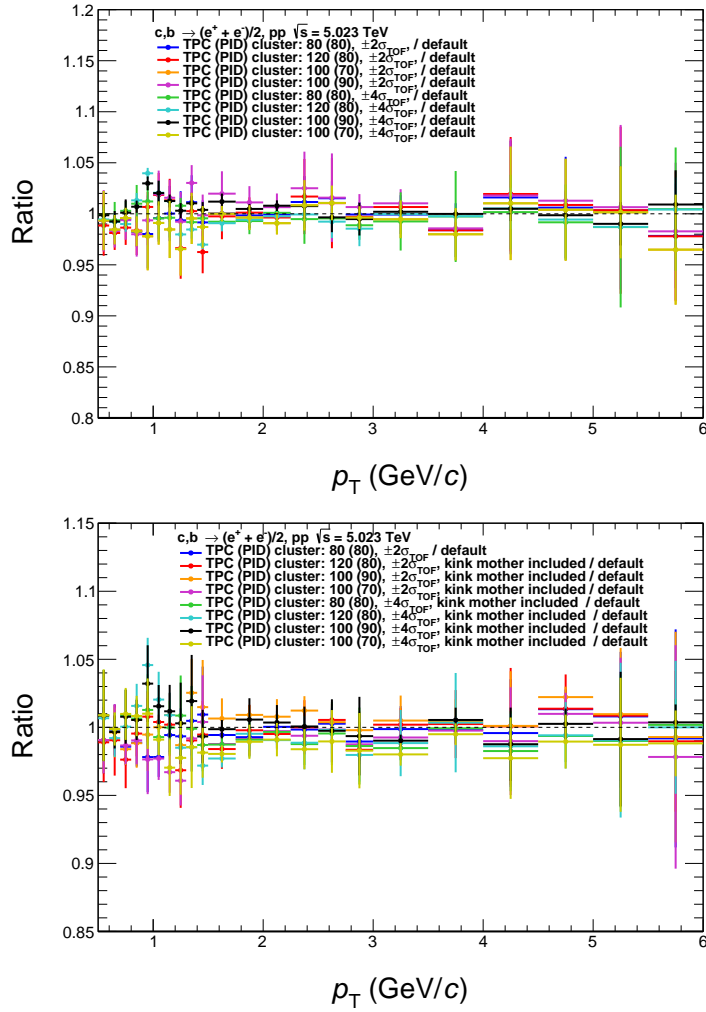
Figure A.6: Ratio of the cross section obtained with the default selection criterion and the varied selection criteria, varying different combination of criteria for the selection of electron candidates.
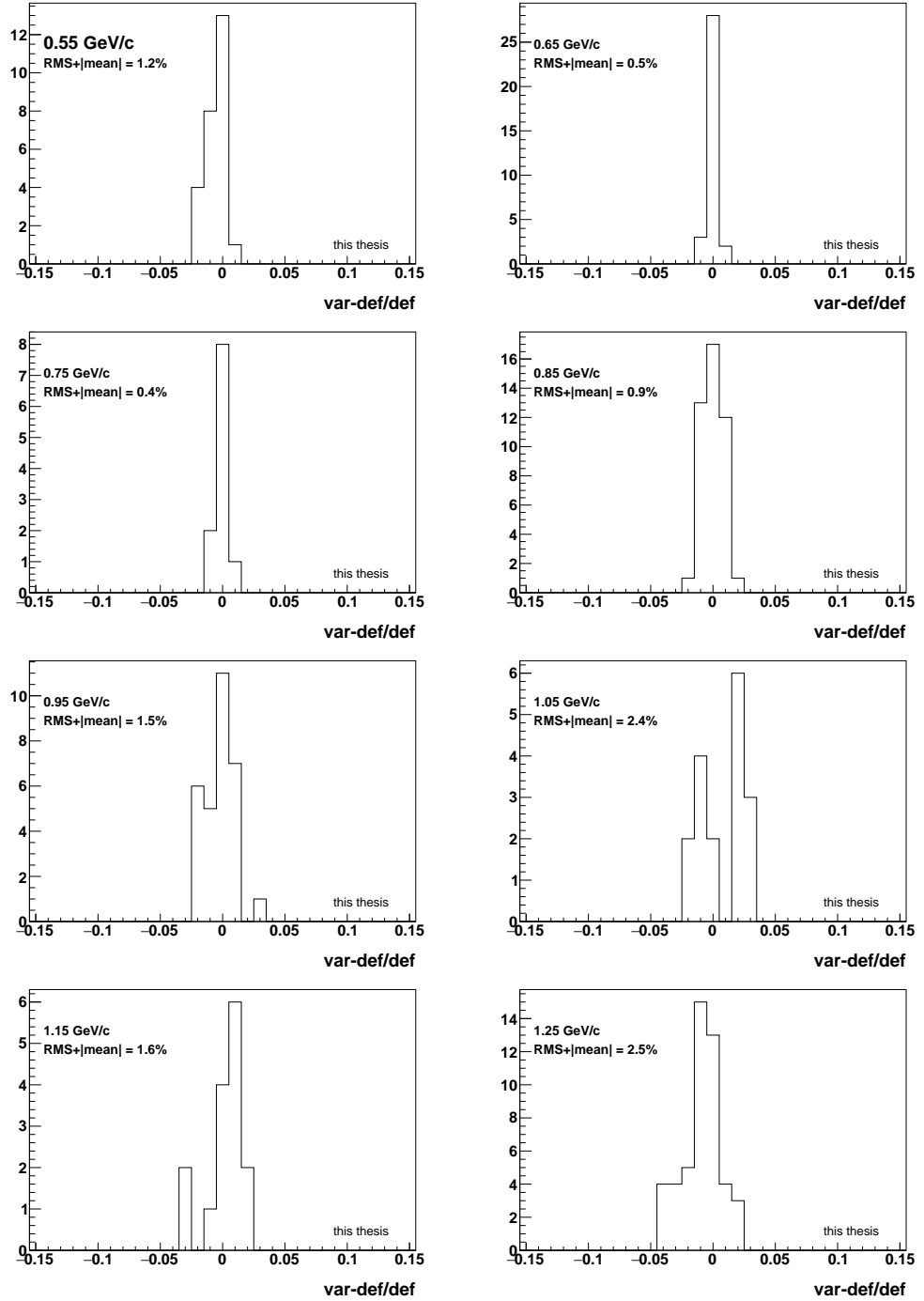
Figure A.7: Distributions of the difference between the cross section obtained with the default selection criteria and the varied selection criteria due to electron candidates for all p_T - intervals considered in this analysis.
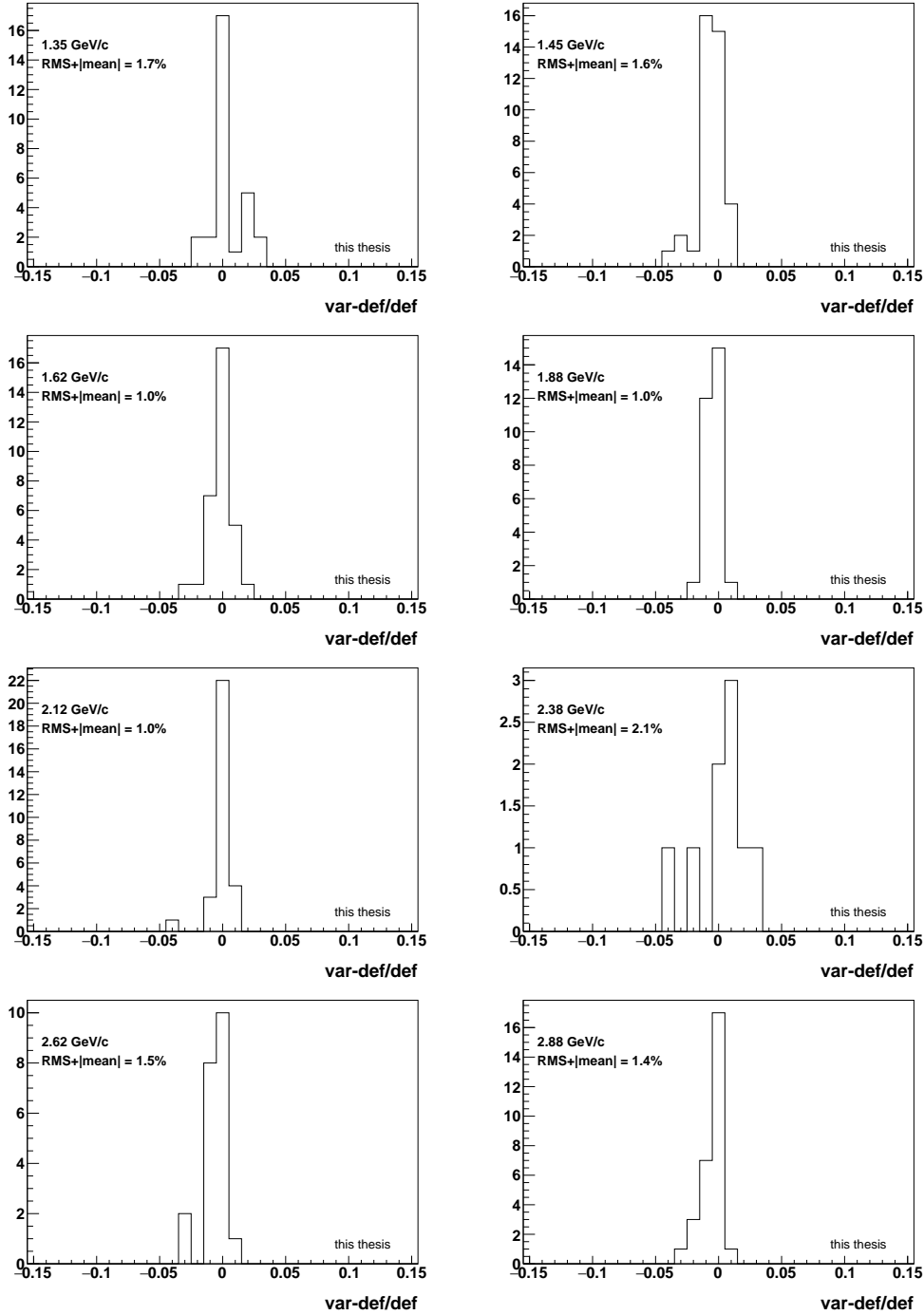
Figure A.8: Distributions of the difference between the cross section obtained with the default selection criteria and the varied selection criteria due to electron candidates for all p_T - intervals considered in this analysis.
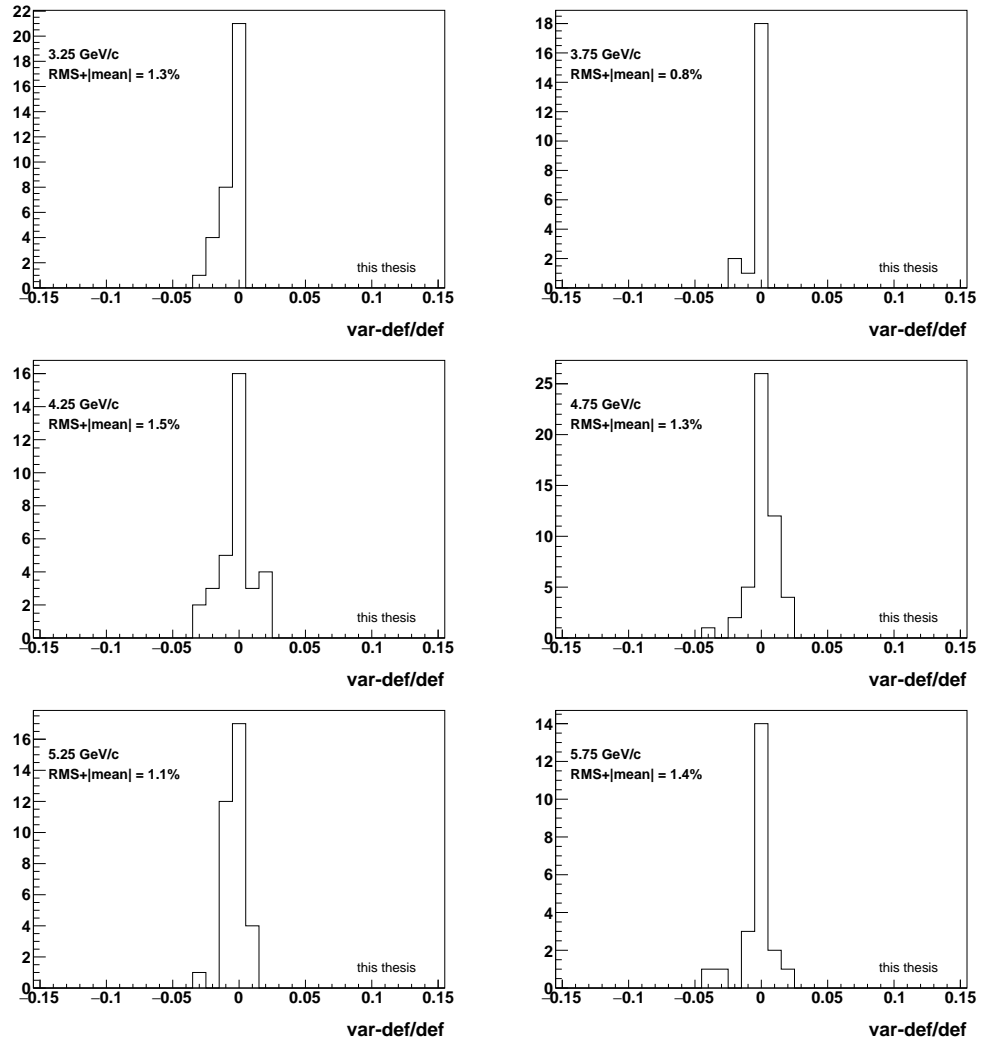
Figure A.9: Distributions of the difference between the cross section obtained with the default selection criteria and the varied selection criteria due to electron candidates for all p_T - intervals considered in this analysis.

A.2.2   TPC only analysis
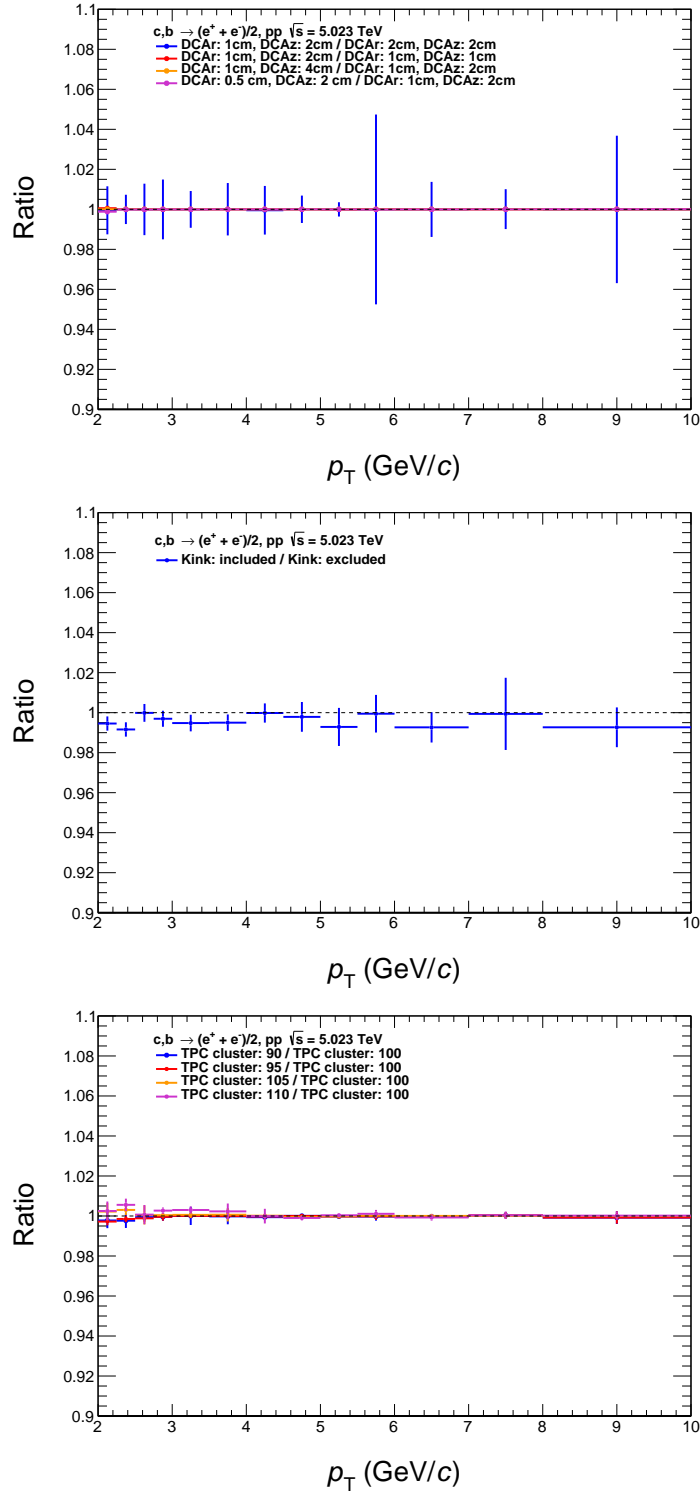
Figure A.10: Ratio of the cross section obtained with the default selection criteria and with the varied selection criteria, varying simultaneously different combination of selection criteria for the selection of electron candidates for the TPC only analysis.
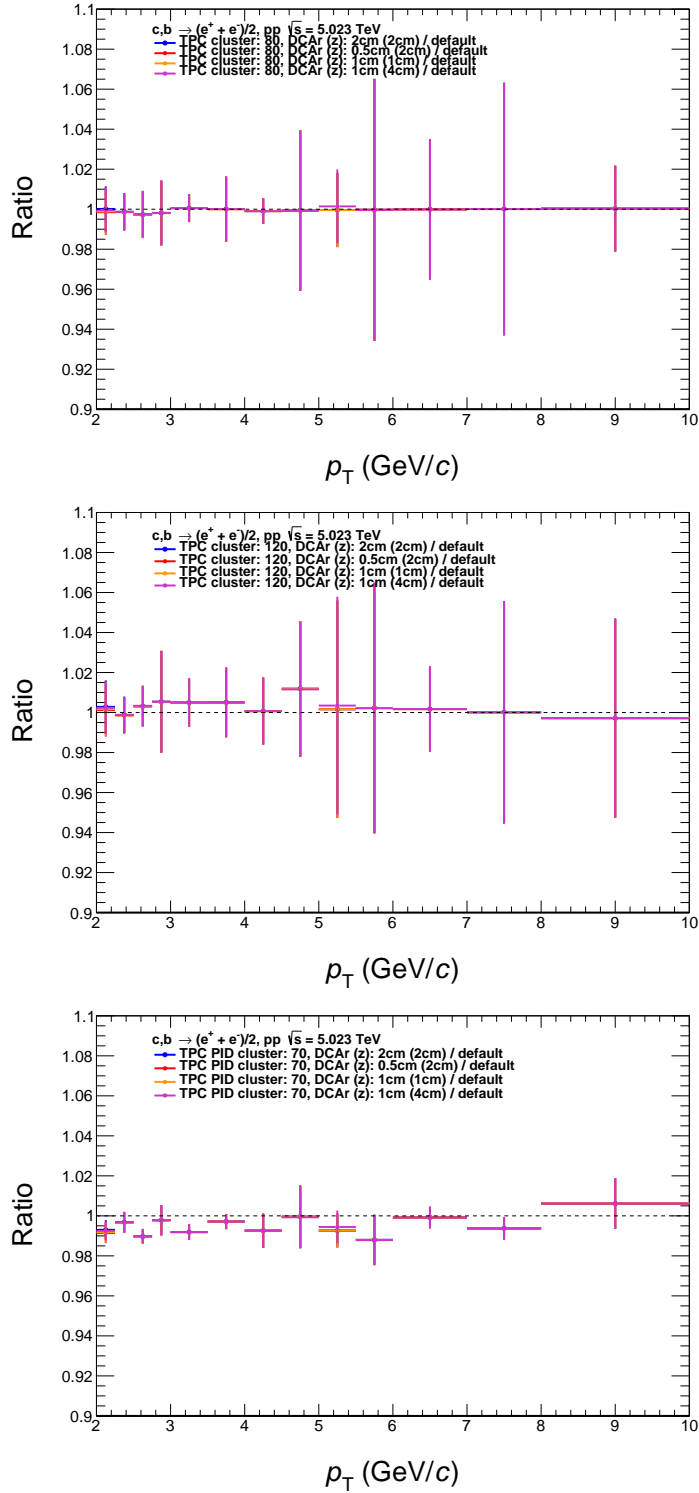
Figure A.11: Ratio of the cross section obtained with the default selection criteria and with the varied selection criteria, varying simultaneously different combination of selection criteria for the selection of electron candidates for the TPC only analysis.

A.3   Systematic uncertainties due to the subtraction of electron from photonic sources

A.3.1   TPC-TOF analysis
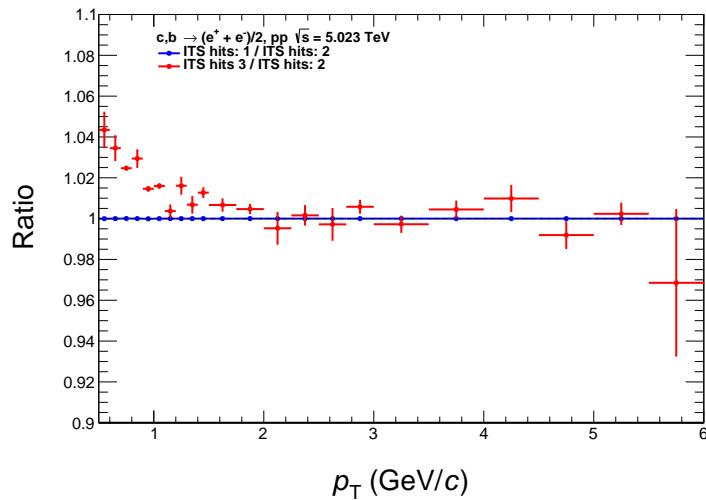
Figure A.12: Ratio of the cross section obtained with the default selection criteria and with the varied selection criteria, varying the number of required ITS hits for the associated tracks.
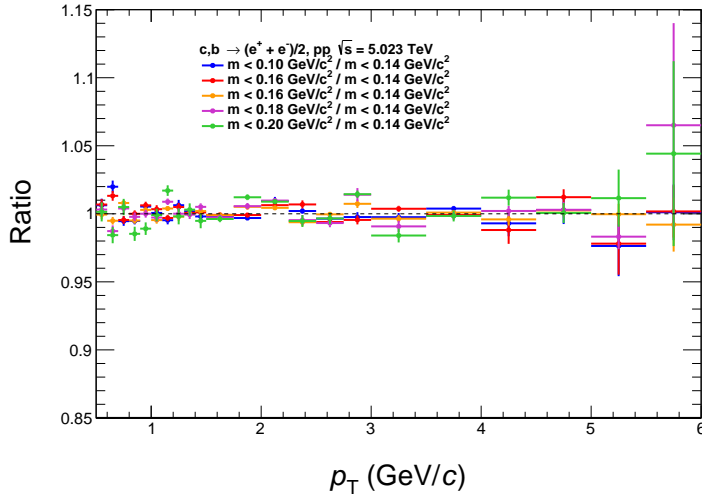
Figure A.13: Ratio of the cross section obtained with the default selection criteria and with the varied selection criteria, varying the cut on the invariant mass of the electron pairs.
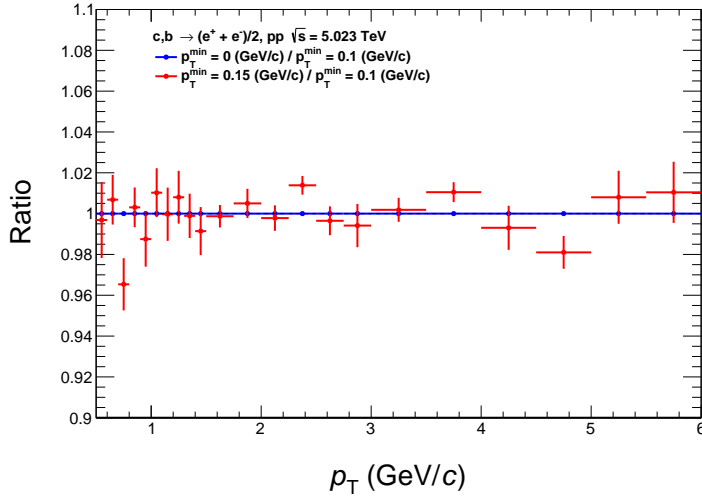
Figure A.14: Ratio of the cross section obtained with the default selection criteria and with the varied selection criteria, varying the minimum p_T of the associated tracks.
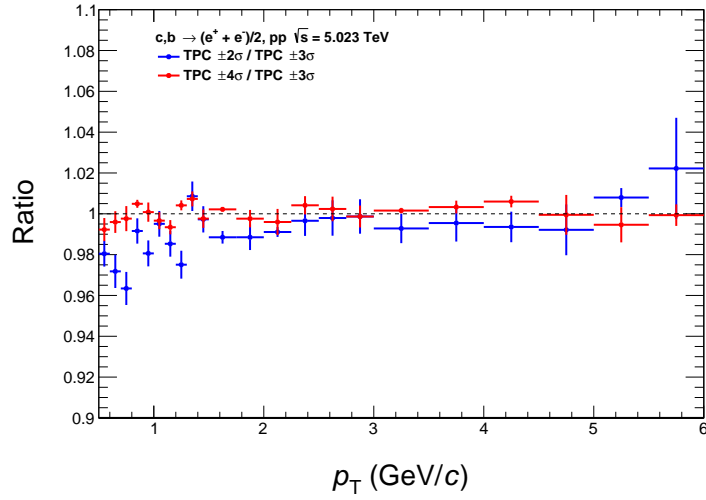
Figure A.15: Ratio of the cross section obtained with the default selection criteria and with the varied selection criteria, varying the selection in $n\sigma_{TPC}^{e}$ of the associated tracks.
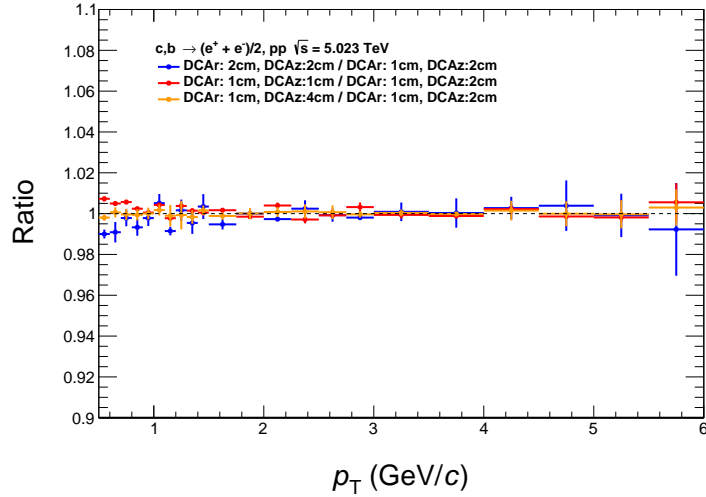
Figure A.16: Ratio of the cross section obtained with the default selection criteria and with the varied selection criteria, varying the DCA_{xy} and DCA_{z} of the associated tracks.
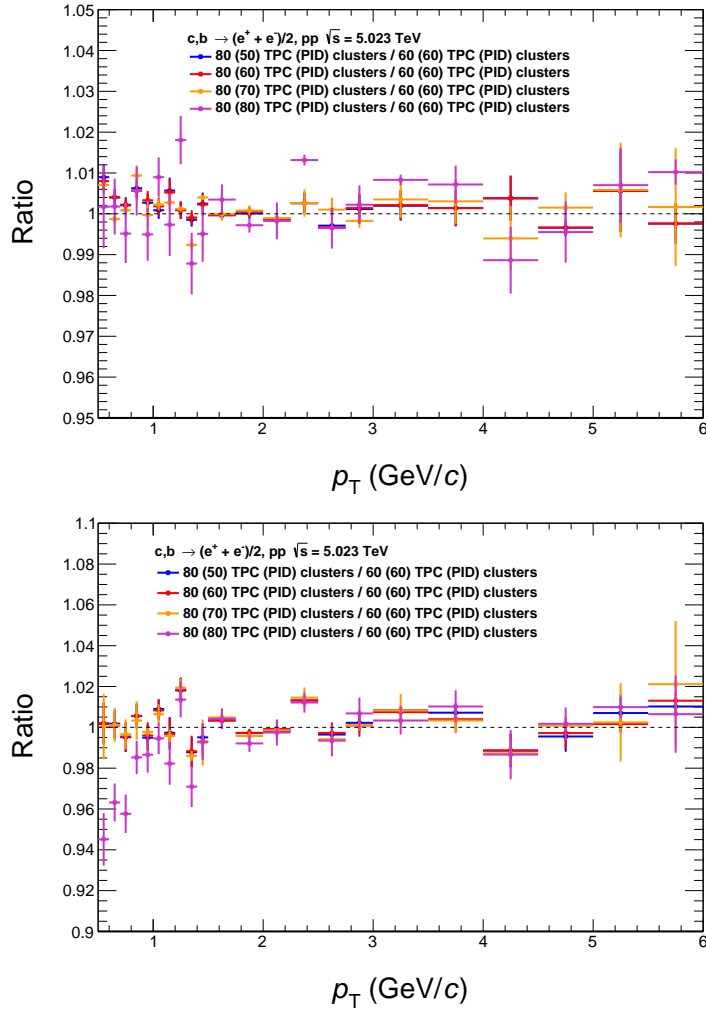
Figure A.17: Ratio of the cross section obtained with the default selection criteria and with the varied selection criteria, varying the number of TPC cluster and TPC cluster for PID of the associated tracks.
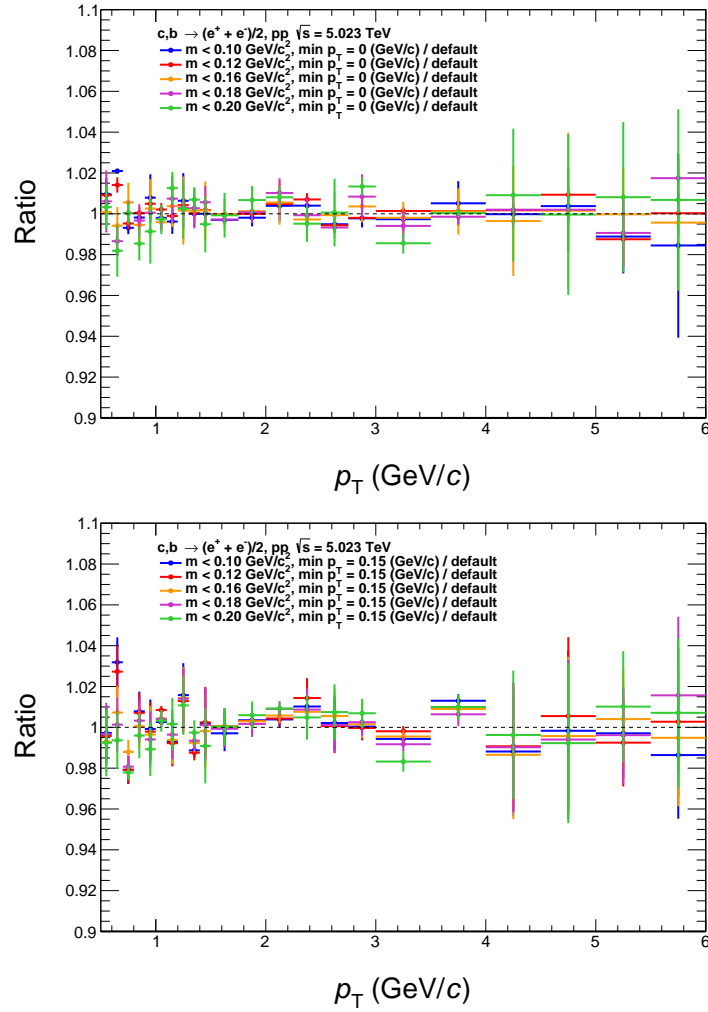
Figure A.18: Ratio of the cross section obtained with the default selection criteria and with the varied selection criteria, varying simultaneously pair mass and minimum p_T.
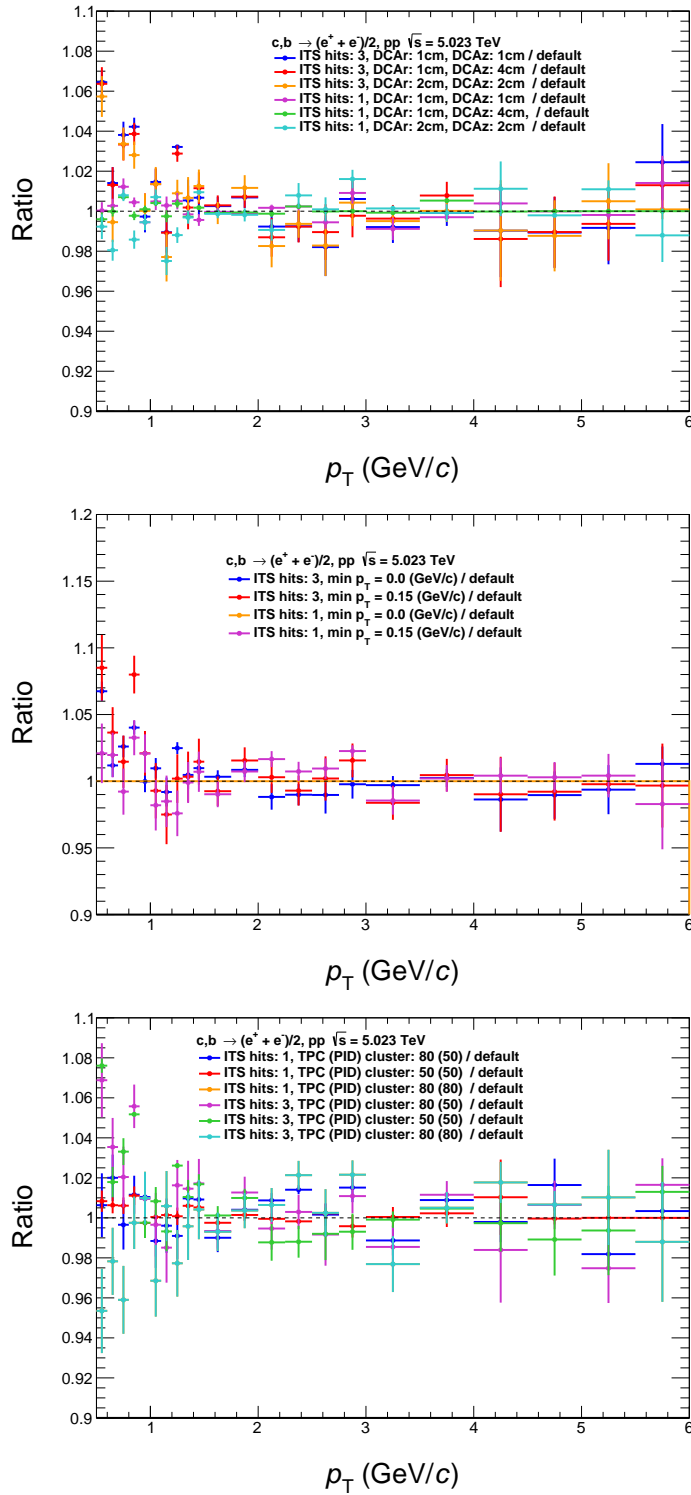
Figure A.19: Ratio of the cross section obtained with the default selection criteria and with the varied selection criteria, varying simultaneously different combination of selection criteria of the associated track candidates.
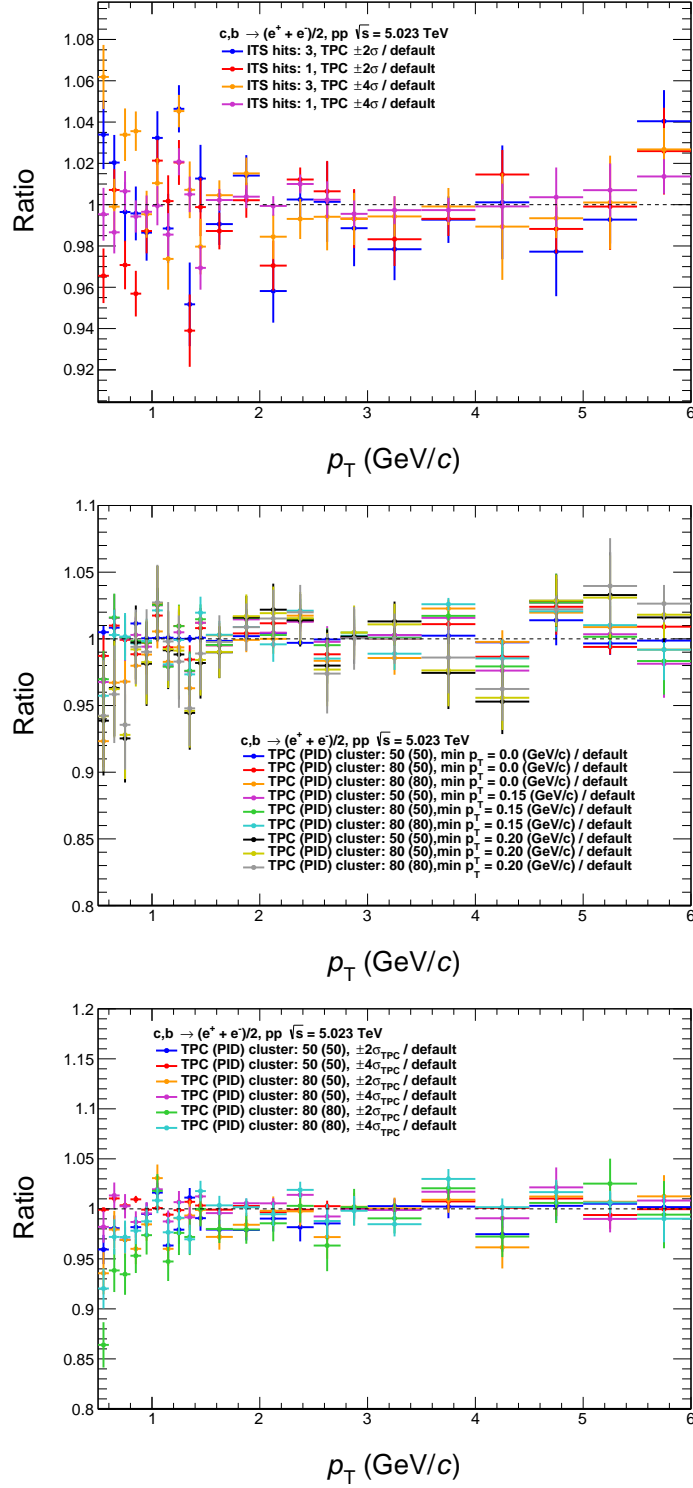
Figure A.20: Ratio of the cross section obtained with the default selection criteria and with the varied selection criteria, varying simultaneously different combination of selection criteria of the associated track candidates.
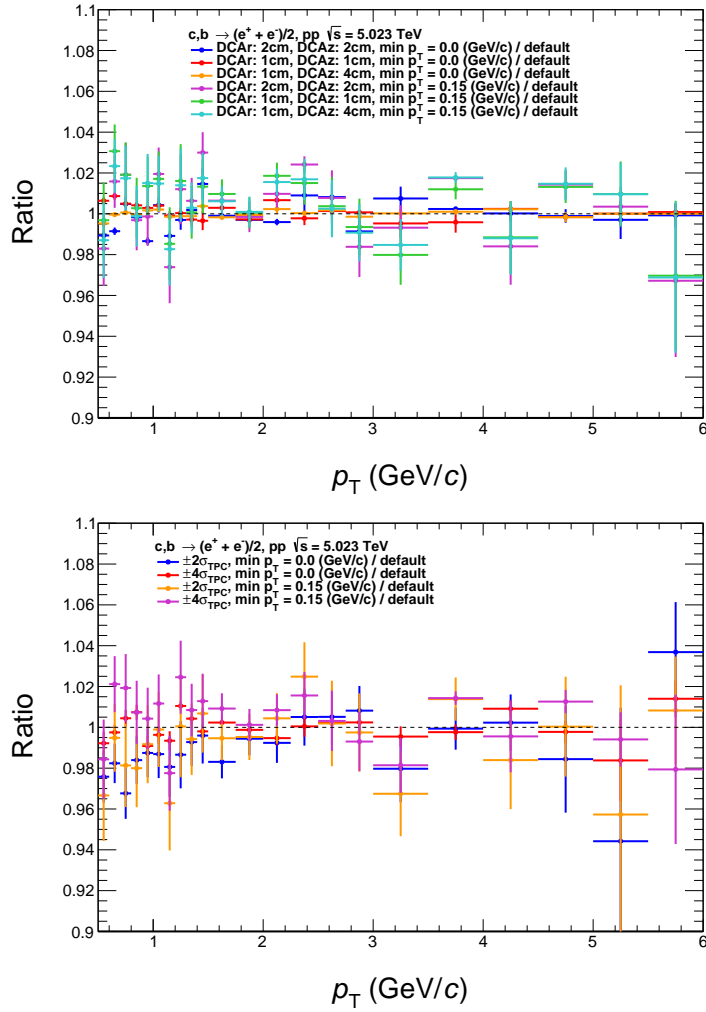
Figure A.21: Ratio of the cross section obtained with the default selection criteria and with the varied selection criteria, varying simultaneously different combination of selection criteria of the associated track candidates.
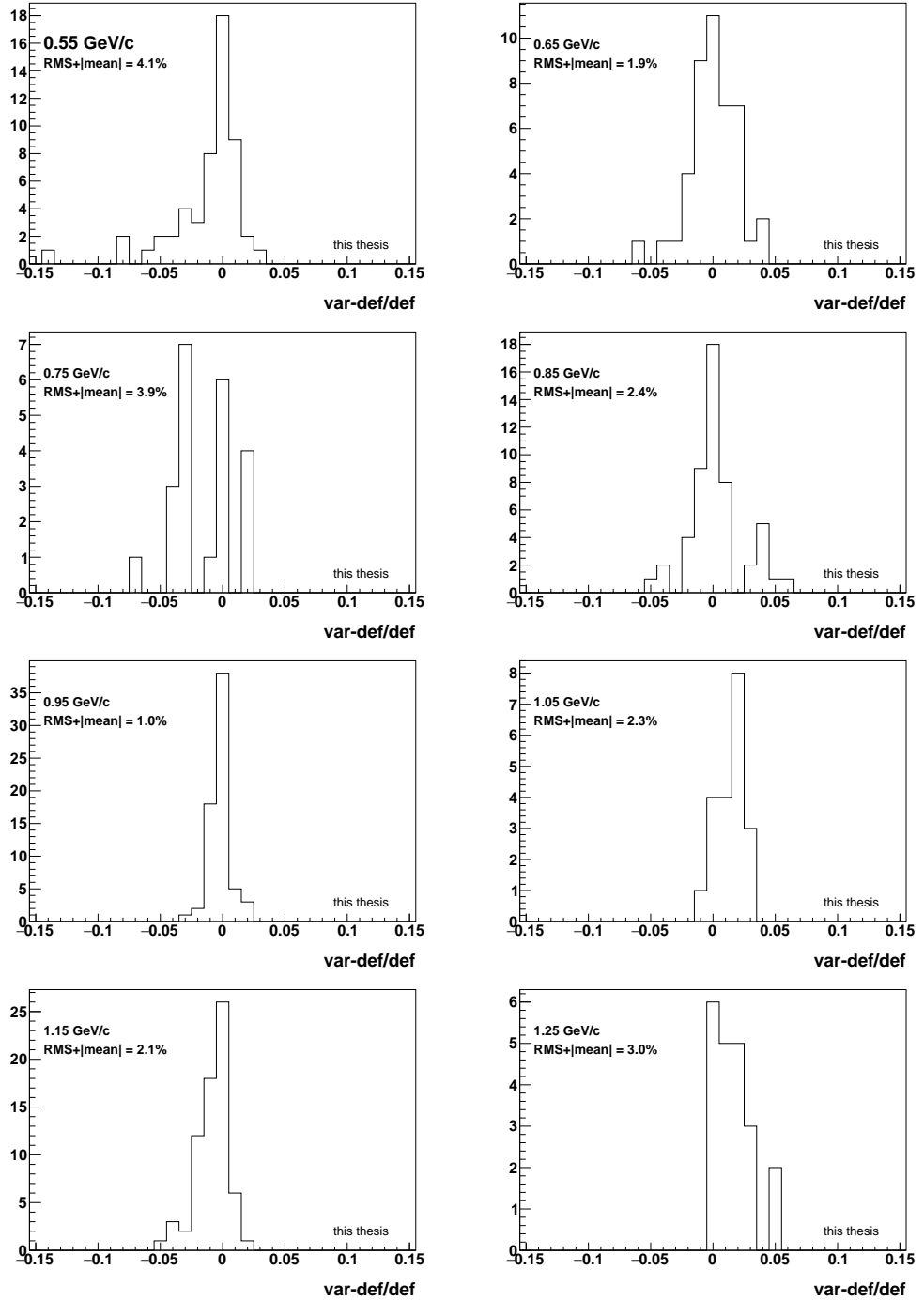
Figure A.22: Distributions of the difference between the cross section obtained with the default selection criteria and the varied selection criteria due to associated tracks for all p_T - intervals considered in this analysis.
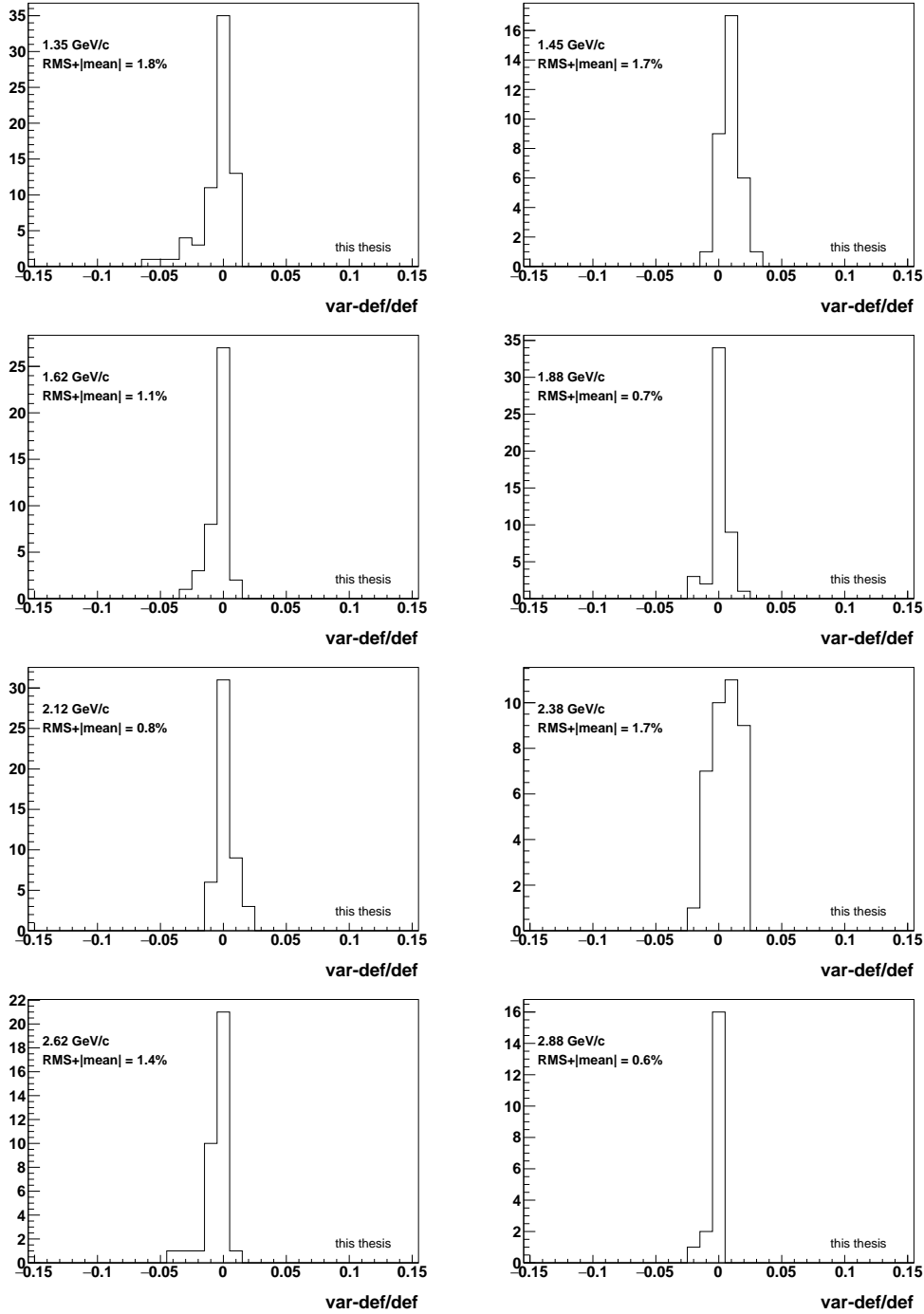
Figure A.23: Distributions of the difference between the cross section obtained with the default selection criteria and the varied selection criteria due to associated tracks for all p_{T} - intervals considered in this analysis.
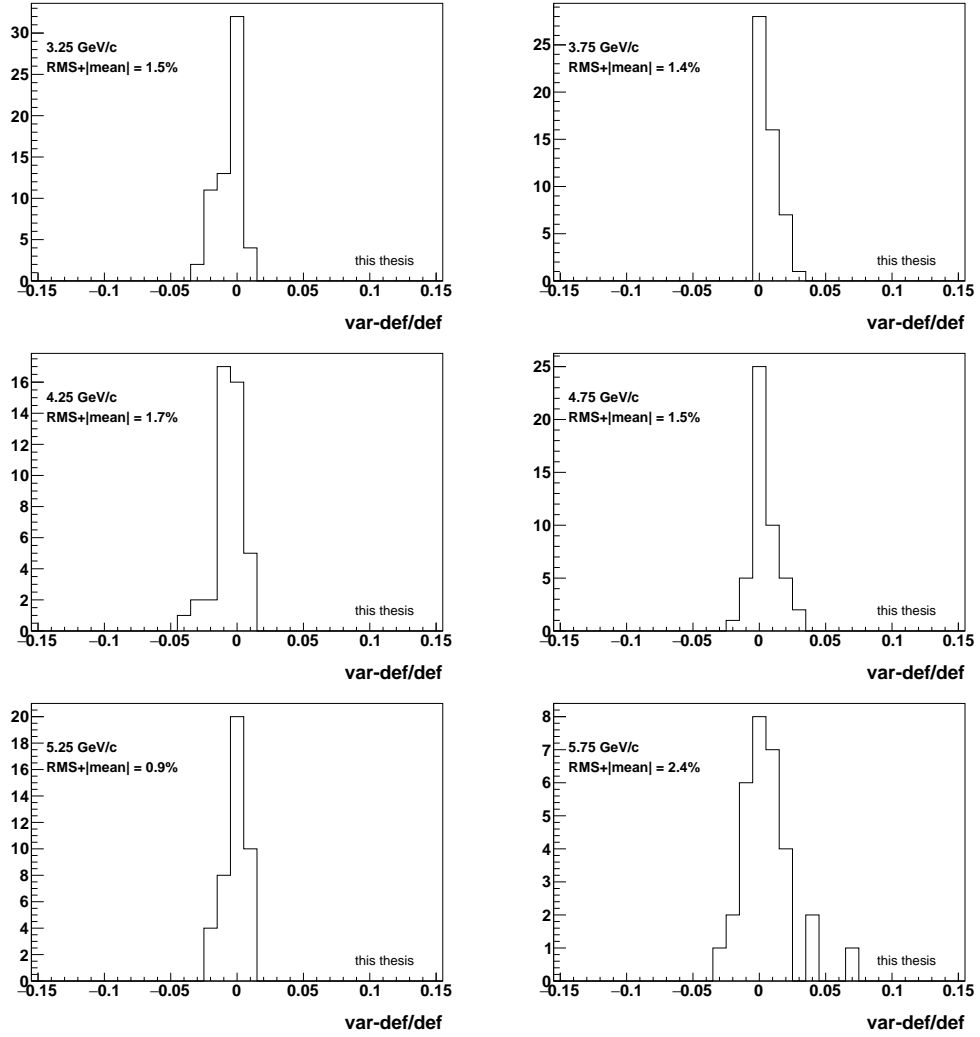
Figure A.24: Distributions of the difference between the cross section obtained with the default selection criteria and the varied selection criteria due to associated tracks for all p_{T} - intervals considered in this analysis.

A.3.2 TPC only analysis
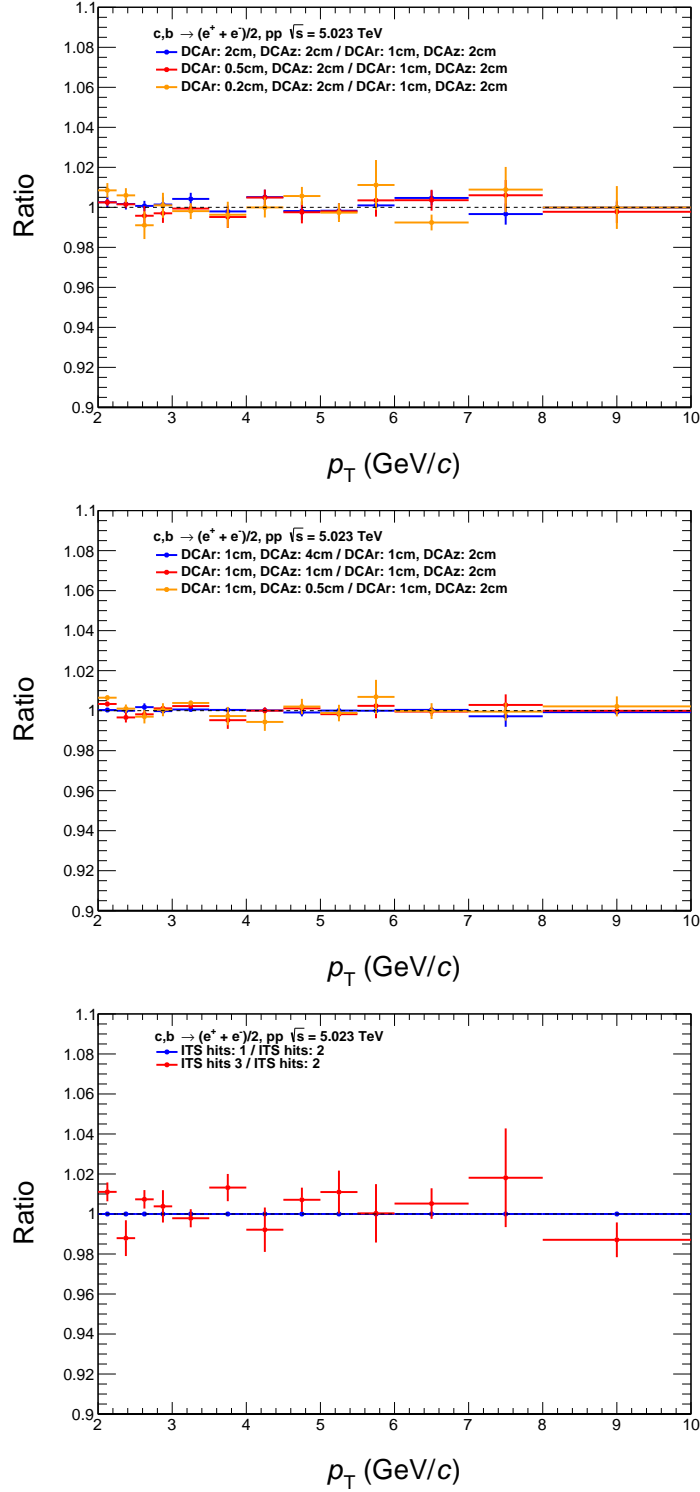
Figure A.25: Ratio of the cross section obtained with the default selection criteria and with the varied selection criteria, varying different combination of selection criteria of the associated track candidates for the TPC only analysis strategy.
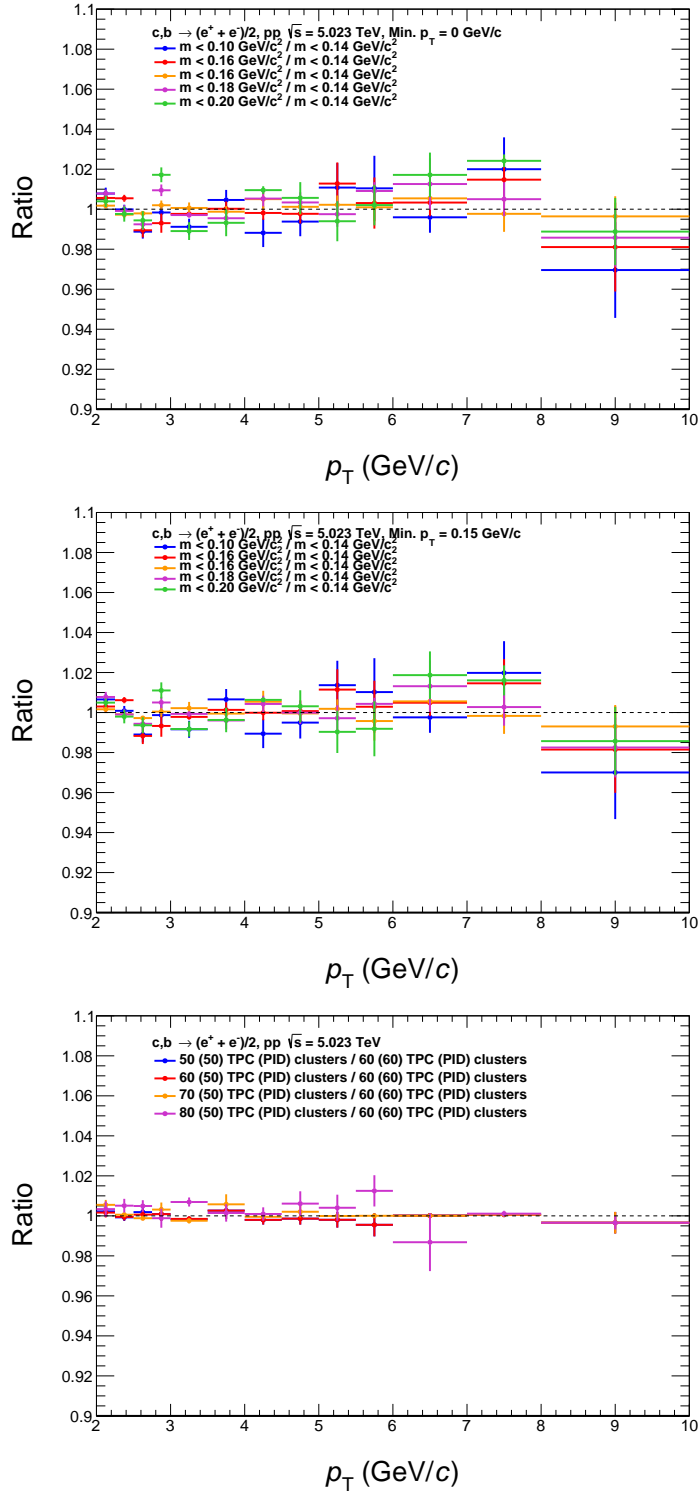
Figure A.26: Ratio of the cross section obtained with the default selection criteria and with the varied selection criteria, varying different combination of selection criteria of the associated track candidates for the TPC only analysis strategy.   91
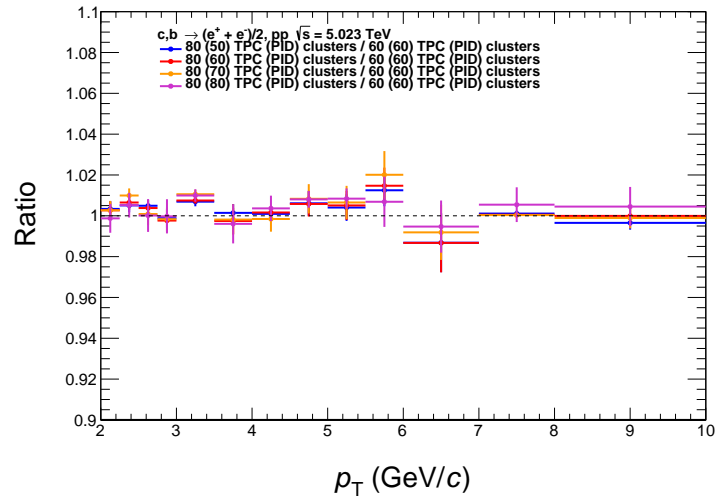
Figure A.27: Ratio of the cross section obtained with the default selection criteria and with the varied selection criteria, varying different combination of selection criteria of the associated track candidates for the TPC only analysis strategy.

List of Figures

List of Tables

References

[1] E. D. Bloom et al. High-energy inelastic $e - p$ scattering at $6°$ and $10°$. *Phys. Rev. Lett.*, 23:930–934, Oct 1969. doi: 10.1103/PhysRevLett.23.930. URL https://link.aps.org/doi/10.1103/PhysRevLett.23.930.

[2] M. Breidenbach et al. Observed behavior of highly inelastic electron-proton scattering. *Phys. Rev. Lett.*, 23:935–939, Oct 1969. doi: 10.1103/PhysRevLett.23.935. URL https://link.aps.org/doi/10.1103/PhysRevLett.23.935.

[3] Martin L. Perl, Eric R. Lee, and Dinesh Loomba. Searches for fractionally charged particles. *Annual Review of Nuclear and Particle Science*, 59(1): 47–65, 2009. doi: 10.1146/annurev-nucl-121908-122035. URL https://doi.org/10.1146/annurev-nucl-121908-122035.

[4] David J Griffiths. *Introduction to elementary particles; 2nd rev. version*. Physics textbook. Wiley, New York, NY, 2008. URL http://cds.cern.ch/record/111880.

[5] H. David Politzer. Reliable perturbative results for strong interactions? *Phys. Rev. Lett.*, 30:1346–1349, Jun 1973. doi: 10.1103/PhysRevLett.30.1346. URL https://link.aps.org/doi/10.1103/PhysRevLett.30.1346.

[6] David J. Gross and Frank Wilczek. Ultraviolet behavior of non-abelian gauge theories. *Phys. Rev. Lett.*, 30:1343–1346, Jun 1973. doi: 10.1103/PhysRevLett.30.1343. URL https://link.aps.org/doi/10.1103/PhysRevLett.30.1343.

[7] M. Tanabashi et al. Review of particle physics. *Phys. Rev. D*, 98:030001, Aug 2018. doi: 10.1103/PhysRevD.98.030001. URL https://link.aps.org/doi/10.1103/PhysRevD.98.030001.

[8] Helmut Satz. The Quark-Gluon Plasma: A Short Introduction. *Nucl. Phys.*, A862-863:4–12, 2011. doi: 10.1016/j.nuclphysa.2011.05.014.

[9] Edward V. Shuryak. Quantum Chromodynamics and the Theory of Superdense Matter. *Phys. Rept.*, 61:71–158, 1980. doi: 10.1016/0370-1573(80)90105-2.

[10] Gines Martinez. Advances in Quark Gluon Plasma. 2013.

[11] Sourendu Gupta. Phases and properties of quark matter. *J. Phys.*, G35: 104018, 2008. doi: 10.1088/0954-3899/35/10/104018.

[12] Patrick Steinbrecher. The QCD crossover at zero and non-zero baryon densities from Lattice QCD. *Nucl. Phys.*, A982:847–850, 2019. doi: 10.1016/j.nuclphysa.2018.08.025.

[13] Alexander Schmah et al. The beam energy scan at RHIC: Recent results from STAR. *Journal of Physics: Conference Series*, 426:012007, mar 2013. doi: 10.1088/1742-6596/426/1/012007. URL `https://doi.org/10.1088%2F1742-6596%2F426%2F1%2F012007`.

[14] David Tlusty. The RHIC Beam Energy Scan Phase II: Physics and Upgrades. In *13th Conference on the Intersections of Particle and Nuclear Physics (CIPANP 2018) Palm Springs, California, USA, May 29-June 3, 2018*, 2018.

[15] R. Averbeck. Heavy-flavor production in heavy-ion collisions and implications for the properties of hot QCD matter. *Prog. Part. Nucl. Phys.*, 70: 159–209, 2013. doi: 10.1016/j.ppnp.2013.01.001.

[16] John C. Collins, Davison E. Soper, and George F. Sterman. Heavy Particle Production in High-Energy Hadron Collisions. *Nucl. Phys.*, B263:37, 1986. doi: 10.1016/0550-3213(86)90026-X.

[17] Ringaile Placakyte. Parton Distribution Functions. In *Proceedings, 31st International Conference on Physics in collisions (PIC 2011): Vancouver, Canada, August 28-September 1, 2011*, 2011.

[18] Richard D. Ball, Valerio Bertone, Stefano Carrazza, Luigi Del Debbio, Stefano Forte, Patrick Groth-Merrild, Alberto Guffanti, Nathan P. Hartland, Zahari Kassabov, José I. Latorre, Emanuele R. Nocera, Juan Rojo, Luca Rottoli, Emma Slade, and Maria Ubiali. Parton distributions from high-precision collider data. *The European Physical Journal C*, 77(10):663, Oct 2017. ISSN 1434-6052. doi: 10.1140/epjc/s10052-017-5199-5. URL `https://doi.org/10.1140/epjc/s10052-017-5199-5`.

[19] Matteo Cacciari et al. The p_T spectrum in heavy flavor hadroproduction. *JHEP*, 05:007, 1998. doi: 10.1088/1126-6708/1998/05/007.

[20] Michael L. Miller et al. Glauber modeling in high energy nuclear collisions. *Ann. Rev. Nucl. Part. Sci.*, 57:205–243, 2007. doi: 10.1146/annurev.nucl.57.090506.123020.

[21] Yuri V Kovchegov. Cronin effect and high-pTsuppression in p(d)a collisions. *Journal of Physics G: Nuclear and Particle Physics*, 30(8):S979–S982, jul 2004. doi: 10.1088/0954-3899/30/8/042. URL `https://doi.org/10.1088%2F0954-3899%2F30%2F8%2F042`.

[22] K. J. Eskola, H. Paukkunen, and C. A. Salgado. EPS09: A New Generation of NLO and LO Nuclear Parton Distribution Functions. *JHEP*, 04:065, 2009. doi: 10.1088/1126-6708/2009/04/065.

[23] Yuri L. Dokshitzer and D. E. Kharzeev. Heavy quark colorimetry of QCD matter. *Phys. Lett.*, B519:199–206, 2001. doi: 10.1016/S0370-2693(01) 01130-3.

[24] Magdalena Djordjevic. Collisional energy loss in a finite size QCD matter. *Phys. Rev.*, C74:064907, 2006. doi: 10.1103/PhysRevC.74.064907.

[25] Elena Botta. Particle identification performance at ALICE. In *5th Large Hadron Collider Physics Conference (LHCP 2017) Shanghai, China, May 15-20, 2017*, 2017.

[26] K. Aamodt et al. The ALICE experiment at the CERN LHC. *JINST*, 3: S08002, 2008. doi: 10.1088/1748-0221/3/08/S08002.

[27] Betty Bezverkhny Abelev et al. Performance of the ALICE Experiment at the CERN LHC. *Int. J. Mod. Phys.*, A29:1430044, 2014. doi: 10.1142/ S0217751X14300440.

[28] L. Betev et al. Definition of the ALICE coordinate system and basic rules for sub-detector components numbering. URL `https://edms.cern.ch/ui/#!master/navigator/document?D: 1020137949:1020137949:subDocs`.

[29] ALICE Collaboration, F Carminati, et al. ALICE: Physics Performance Report, Volume I. *Journal of Physics G: Nuclear and Particle Physics*, 30 (11):1517, 2004. URL `http://stacks.iop.org/0954-3899/30/i=11/ a=001`.

[30] K Aamodt et al. Alignment of the ALICE Inner Tracking System with cosmic-ray tracks. *JINST*, 5:P03003, 2010. doi: 10.1088/1748-0221/5/03/ P03003.

[31] J. Schukraft. Heavy Ion physics with the ALICE experiment at the CERN LHC. *Phil. Trans. Roy. Soc. Lond.*, A370:917–932, 2012. doi: 10.1098/rsta. 2011.0469.

[32] J. Alme et al. The ALICE TPC, a large 3-dimensional tracking device with fast readout for ultra-high multiplicity events. *Nuclear Instruments and Methods in Physics Research Section A: Accelerators, Spectrometers,*

Detectors and Associated Equipment, 622(1):316 – 367, 2010. ISSN 0168-9002. doi: https://doi.org/10.1016/j.nima.2010.04.042. URL `http://www.sciencedirect.com/science/article/pii/S0168900210008910`.

[33] Andrea Dubla, Raimond Snellings, and Alessandro Grelli. Elliptic flow at different collision stages, Apr 2016. URL `http://cds.cern.ch/record/2161742`. Presented 06 Apr 2016.

[34] URL `http://aliceinfo.cern.ch/Public/en/Chapter2/Chap2_TOF.html`.

[35] Christian Lippmann. Particle identification. *Nucl. Instrum. Meth.*, A666: 148–172, 2012. doi: 10.1016/j.nima.2011.03.009.

[36] Torbjorn Sjostrand, Stephen Mrenna, and Peter Z. Skands. PYTHIA 6.4 Physics and Manual. *JHEP*, 05:026, 2006. doi: 10.1088/1126-6708/2006/05/026.

[37] Torbjorn Sjostrand, Stephen Mrenna, and Peter Z. Skands. A Brief Introduction to PYTHIA 8.1. *Comput. Phys. Commun.*, 178:852–867, 2008. doi: 10.1016/j.cpc.2008.01.036.

[38] René Brun et al. GEANT Detector Description and Simulation Tool. 1994. doi: 10.17181/CERN.MUHF.DMJ1.

[39] Völkl Martin. Study of the transverse momentum spectra of semielectronic heavy flavor decays in pp collisions at $\sqrt{s}$ = 7 TeV and Pb-Pb collisions at $\sqrt{s_{NN}}$ 2= 2.76 TeV with ALICE. Master's thesis, Universität Heidelberg, 2012. URL `https://www.physi.uni-heidelberg.de//Publications/ThesisVoelkl.pdf`.

[40] Betty Abelev et al. Measurement of electrons from semileptonic heavy-flavour hadron decays in pp collisions at $\sqrt{s}$ = 7 TeV. *Phys. Rev.*, D86: 112007, 2012. doi: 10.1103/PhysRevD.86.112007.

[41] Jan Wagner. *Electrons from decays of open charm and beauty hadrons in p-Pb collisions at sqrt(sNN) = 5.02 TeV*. PhD thesis, Technische Universität Darmstadt, Darmstadt, July 2016. URL `http://tuprints.ulb.tu-darmstadt.de/5710/`.

[42] Yasser Corrales Morales et al. Production of pions, kaons and protons in pp and Pb-Pb collisions at $\sqrt{s}$= 5.02 TeV. *Analysis Note*, 2017. URL `https://alice-notes.web.cern.ch/node/589`.

[43] F. Bossu et al. Phenomenological interpolation of the inclusive J/psi cross section to proton-proton collisions at 2.76 TeV and 5.5 TeV. 2011.

[44] ALICE luminosity determination for pp collisions at $\sqrt{s} = 5$ TeV. Jul 2016. URL `https://cds.cern.ch/record/2202638`.

[45] Roger Barlow. Systematic errors: Facts and fictions. In *Advanced Statistical Techniques in Particle Physics. Proceedings, Conference, Durham, UK, March 18-22, 2002*, pages 134–144, 2002. URL `http://www.ippp.dur.ac.uk/Workshops/02/statistics/proceedings//barlow.pdf`.

[46] URL `https://twiki.cern.ch/twiki/bin/viewauth/ALICE/AliDPGtoolsTrackSystematicUncertaintyBookkeping`.

[47] 2016. URL `http://www.lpthe.jussieu.fr/~cacciari/fonll/fonllform.html`.

[48] Shreyasi Acharya et al. Measurements of low-p_T electrons from semileptonic heavy-flavour hadron decays at mid-rapidity in pp and Pb-Pb collisions at $\sqrt{s_{NN}} = 2.76$ TeV. *JHEP*, 10:061, 2018. doi: 10.1007/JHEP10(2018)061.

[49] Preliminary Physics Summary: Measurements of low-p_T electrons from semileptonic heavy-flavour hadron decays at mid-rapidity in pp collisions at $\sqrt{s} = 7$ TeV. May 2018. URL `https://cds.cern.ch/record/2317185`.

[50] Camila De Conti and Andrea Dubla. Electrons from heavy-flavour hadron decays at mid-rapidity and low transverse momenta in pp collisions at $\sqrt{s} = 13$ TeV. 2017. URL `https://alice-notes.web.cern.ch/node/651`.

[51] Matteo Cacciari, Michelangelo L. Mangano, and Paolo Nason. Gluon PDF constraints from the ratio of forward heavy-quark production at the LHC at $\sqrt{S} = 7$ and 13 TeV. *Eur. Phys. J.*, C75(12):610, 2015. doi: 10.1140/epjc/s10052-015-3814-x.

[52] Andrea Dubla. Nuclear modification factor of electrons from of heavy-flavour hadron decays in Xe-Xe collisions at $\sqrt{s_{NN}} = 5.44$ TeV. 2018. URL `https://alice-notes.web.cern.ch/node/730`.

[53] Mattia Faggin, Andrea Dubla, and Silvia Masciocchi. Measurments of low p_T electrons from heavy-flavour hadrons decays in Pb-Pb collisions at $\sqrt{s_{NN}}$ TeV with ALICE. 2018. URL `https://alice-notes.web.cern.ch/node/733`.

[54] M. Gyulassy, P. Levai, and I. Vitev. Reaction operator approach to non-Abelian energy loss. *Nucl. Phys.*, B594:371–419, 2001. doi: 10.1016/S0550-3213(00)00652-0.

[55] Jan Uphoff et al. Elastic and radiative heavy quark interactions in ultra-relativistic heavy-ion collisions. *J. Phys.*, G42(11):115106, 2015. doi: 10.1088/0954-3899/42/11/115106.

[56] Georges Aad et al. Measurements of the electron and muon inclusive cross-sections in proton-proton collisions at $\sqrt{s} = 7$ TeV with the ATLAS detector. *Phys. Lett.*, B707:438–458, 2012. doi: 10.1016/j.physletb.2011.12.054.

[57] R. Averbeck et al. Reference Heavy Flavour Cross Sections in pp Collisions at $\sqrt{s} = 2.76$ TeV, using a pQCD-Driven $\sqrt{s}$-Scaling of ALICE Measurements at $\sqrt{s} = 7$ TeV. 2011.

[58] Taesoo Song et al. Charm production in Pb + Pb collisions at energies available at the CERN Large Hadron Collider. *Phys. Rev.*, C93(3):034906, 2016. doi: 10.1103/PhysRevC.93.034906.

[59] Min He, Rainer J. Fries, and Ralf Rapp. Heavy Flavor at the Large Hadron Collider in a Strong Coupling Approach. *Phys. Lett.*, B735:445–450, 2014. doi: 10.1016/j.physletb.2014.05.050.

[60] Jiechen Xu, Jinfeng Liao, and Miklos Gyulassy. Bridging Soft-Hard Transport Properties of Quark-Gluon Plasmas with CUJET3.0. *JHEP*, 02:169, 2016. doi: 10.1007/JHEP02(2016)169.

[61] Magdalena Djordjevic and Marko Djordjevic. Predictions of heavy-flavor suppression at 5.1 TeV Pb + Pb collisions at the CERN Large Hadron Collider. *Phys. Rev.*, C92(2):024918, 2015. doi: 10.1103/PhysRevC.92.024918.

[62] Magdalena Djordjevic and Marko Djordjevic. Lhc jet suppression of light and heavy flavor observables. *Physics Letters B*, 734:286 – 289, 2014. ISSN 0370-2693. doi: https://doi.org/10.1016/j.physletb.2014.05.053. URL http://www.sciencedirect.com/science/article/pii/S0370269314003633.

Erklärung:

Ich versichere, dass ich diese Arbeit selbstständig verfasst habe und keine anderen als die angegebenen Quellen und Hilfsmittel benutzt habe.

Heidelberg, den (Datum)   . . . .